In-plane anisotropic nanocolumnar films for advanced functional applications

Julián Parra Barranco

Instituto de Ciencia de Materiales de Sevilla (US-CSIC)
Universidad de Sevilla

PhD thesis, 2015

In-plane anisotropic nanocolumnar films for advanced functional applications

A dissertation submitted for the degree of
Philosophiæ Doctor (PhD)

Memoria presentada para optar al grado
de Doctor por la Universidad de Sevilla

Seville, April 2015

Julián Parra Barranco

Directed by:

Dr. Ángel Barranco Quero
Científico Titular CSIC
Instituto de Ciencia de Materiales de Sevilla
(CSIC-Universidad de Sevilla)

Pr. Agustín Rodríguez González-Elipe
Profesor de Investigación CSIC
Instituto de Ciencia de Materiales de Sevilla
(CSIC-Universidad de Sevilla)

Tutor:

Pr. José Antonio Odriozola Gordón
Catedrático Universidad de Sevilla
Dpt. Química Inorgánica
(Universidad de Sevilla)

Index

Chapter 1

Introduction

Nowadays, the development of new materials entails the preparation of systems with properties that can be predicted and controlled as a function of final technology applications. This perspective is also a requirement by the development of nanostructured materials intended for different final functional applications (optics, magnetism, chemistry, electronics, etc).

The work included in this thesis deals with nanostructured thin films and the analysis of a series of related applications. A customary definition of thin film is that of a layer of material ranging from fractions of a nanometer (monolayer) to several micrometers in thickness, that provides a new characteristic or property to the substrate material where it has been deposited. Thin films of functional materials are directly or indirectly involved in a large series of applications and are essential for the advance technological areas such as optoelectronics, photonics, magnetism and many others[1–5].

Currently, thin film materials are used in semiconductor devices[6], telecommunications, integrated circuits[7], transistors[8,9], solar cells[10], light-emitting diodes[11,12], photoconductors[13], light crystal displays[14], magneto-optic memories[15,16], smart windows[17] and multifunctional emerging coatings, as well as in cutting tools or sensors[18,19].

Figure 1.1 shows some examples of thin films incorporated in flexible microelectronic device (left) and optical filters (right).

Figure 1.1- Some examples of thin film applications in microelectronics and integrated optics: (left) flexible electronic integrated circuit (right) optical filters.

This wide range of applications is possible thanks to the large variety of materials that can be processed in form of thin films, encompassing inorganic and organic compounds, metals, polymers etc. The present work focuses on oxides, namely ITO, SiO_2, and TiO_2 and addresses applications related with their electrical, optical and surface wetting applications.

In this thesis the method of choice to prepare nanostructured thin films of the aforementioned materials is physical vapour deposition (PVD) in the so-called glancing angle deposition (GLAD) configuration and a full account of it will be given in the next sections.

In this introductory chapter we describe the basic concepts about the growth mechanism and the main microstructural features of the films prepared by this technique. In addition, some basic notions are commented about electrical, optical and wetting properties of these nanostructures as resulting from a brief literature survey of the last ten years.

1.1 Thin Films Deposition Techniques

The choice of the proper deposition technique is crucial for the final application of the thin films. Factors like the nature of the substrate and coating or requirements of temperature, crystallinity, etc… will determine the most suitable deposition technique. Furthermore, the scalability of the technique at industrial level is an extremely important requisite for the manufacture of real commercial devices.

Dry methods of deposition used to fabricate thin films can be divided in Physical and Chemical methods[20]

In the physical methods the required material is sublimed or ejected from a source, i.e. evaporation or sputtering, whereas in the chemical methods an "in situ" chemical reaction constitutes the origin of the material to be deposited.

The thin films developed within this thesis have been fabricated by Physical Vapour Deposition (PVD), using an electron beam to sublimate the material and a Glancing angle deposition (GLAD) geometry to control the microstructure. Moreover, in this work we have developed a novel modification of that method to assist the deposition with plasma. We have called this approach Plasma Assisted electron Beam Deposition (PA-GLAD). Basics aspects of these two techniques are described in the next sections.

1.1.1 Physical Vapour Deposition (PVD)

The term Physical Vapour Deposition (PVD) was originally coined in the 1966 book "Vapour Deposition" by C. F. Powell, J. H. Oxley and J. M. Blocher Jr., although Michael Faraday already used PVD to deposit coatings as early as 1838.

PVD is a process based on the evaporation of the required material from a solid target and the subsequent condensation on a specific substrate under vacuum conditions. To achieve this goal, the material in solid state is heated until its evaporation (thermal evaporation) or is "sputtered" by an intense bombardment with ions (sputtering). These methods are widely used to deposit different types of materials, mainly metal, metal oxides or nitrides.

1.2 Glancing Angle Deposition (GLAD)

Compact thin films are obtained when the substrate is placed at normal geometry with respect to the evaporated flux[21,22].Meanwhile, when the deposition flux forms a glancing angle with the substrate, an additional variable is introduced in the growth process with significant consequences in the film microstructure and compactness.

1.2.1. Geometry of the deposition process and shadowing effects.

It is commonly accepted that at low temperatures and GLAD conditions, the main mechanistic factor controlling the nanostructure evolution is the existence of "shadowing" effects that prevent the deposition of particles in the regions situated behind the initially formed nuclei (the so-called shadowed regions)[23,24]

Figures 1.2 represent an ideal GLAD geometrical scheme accounting for the deposition from a small source. This situation is typical of e-beam assisted evaporation processes, the most common experimental arrangement for GLAD of thin films. The scheme in this figure highlights the geometrical parameters which are relevant for the GLAD of thin films, namely the zenithal angle or deposition angle aligning the source and the film, α, the azhimutal angle, φ, and the polar angles, δ and θ. The zenithal (deposition angle) and azhimutal angles are well defined in e-beam assisted evaporation experiments where the target source can be considered nearly punctual.

According to Figure 1.2, drawn to illustrate the most basic notions of thin film growth by GLAD[23–25], the first nuclei formed during the earliest stages of deposition project a shadow behind them that prevents the arrival of the evaporated material at these zones of the substrate. As the deposition progresses, these nuclei promote the development of tilted and separated nanocolumns. Outstanding properties of GLAD thin films like porosity, birefringence, magnetic anisotropy and others are directly dependent on this microstructure consisting of tilted and separated nanocolumns, such as it will be described in next sections.
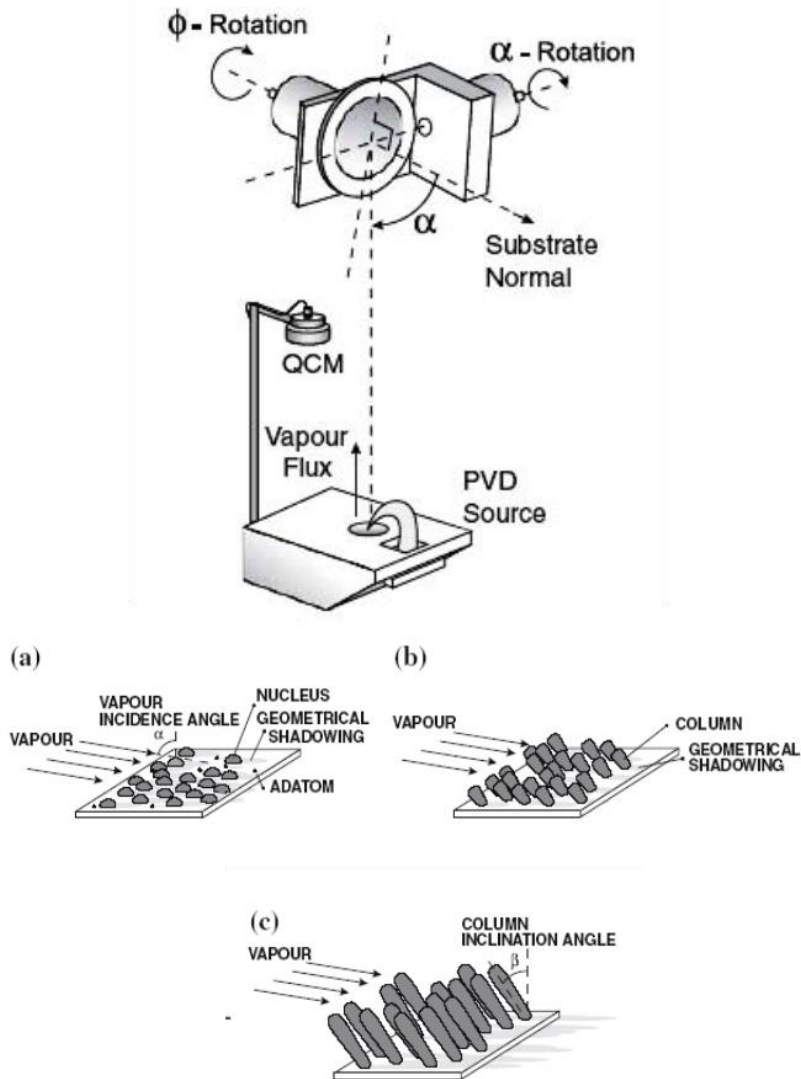
Figure 1.2. (Top) Scheme of an electron beam physical vapour deposition in glancing angle configuration. The design of the nanostructure of the thin film is achieved by adjusting the angles (α) and (φ) during deposition. (down).- Scheme of columnar growth mechanism in a GLAD configuration. In the first stages of growth (a) atoms condense and form nuclei that produce a shadowing effect in different regions (b). The final film is composed by columns which grow from nuclei and are inclined in the direction of the vapour source (c). The main geometrical parameters have been indicated: the zenithal angle of the vapour incidence (α) and the angle of the tilted columns (φ).

7

In general, the low kinetic energy of the vapour species when landing onto the surface (the energy of evaporated atoms is around 0.2 eV) ensures that no kinetic energy-induced processes are likely to take place and that the competitive growth of tilted nanostructures is directly dependent on the arrival angle of vapour species[26].

The relation between the tilt angle of the nanocolumns and the zenithal angle of deposition α , is of the outmost importance for the control of the film properties[27–29] and was roughly described by means of the heuristic tangent rule deduced from experimental data by Nieuwenhuizen and Haanstra [23]. This rule describes the relation between both angles (α, β)[28] by a direct tangent relation. More recently, Tait et al.[30] proposed the so-called cosine rule, which attempts to describe the relation between both angles using cosine relationships. None of the two relations succeed in accounting the experimental tilting angles and, in general, fail for most deposition conditions. Based on recently published results, Álvarez et al.[31,32], have succeeded in accounting for the dependence between α and β by means of new concept that takes into account the interaction between the deposition particles and the surface of the deposited material.(next section and Chapter 3)

Figure 1.3 shows some examples of thin films prepared by GLAD. Different microstructures can be obtained by changing the deposition angle (α). Moreover, ziz-zag or helicoidally structures (i.e., sculptured thin films) can be developed by changing during deposition the orientation of the substrate with respect to the direction of arrival of the vapour flux (sculptured layers)[33].
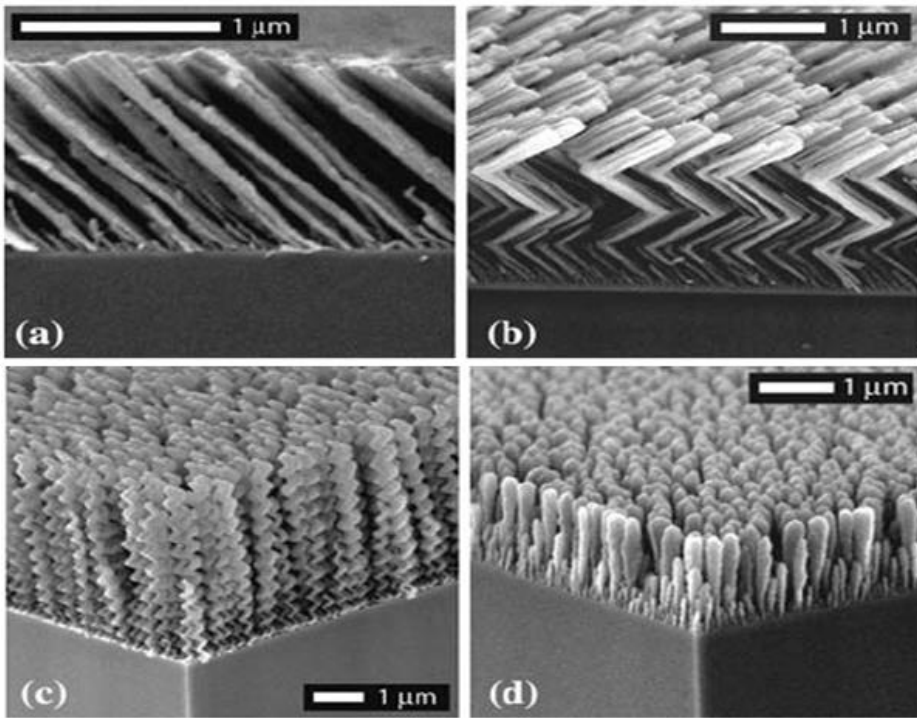
Figure 1.3 *Examples of nanostructured thin films prepared by GLAD-PVD. The thin film a) shows a columnar structure grown at different oblique angles, and b) the same kind of deposition, but rotating the sample 180º at regular time intervals. Samples c) and d) are grown by rotating the sample at a constant speed, c) spirals obtained at low speed while isolated columns are formed at high rotation speed* [33].

In the present work we will develop microstructures obtained by changing the zenithal angle (α) during the evaporation of single inorganic oxides such as SiO_2, TiO_2 and ITO. Other experimental parameters, e.g., the use of a plasma during deposition, are also incorporated during the deposition process as discussed in the next chapters.

1.3 Microstructure of GLAD thin films.

Nowadays, the development of new material systems is intended to manufacture devices with predicted and controlled properties as required for specific technological applications. Unlike isotropic materials that have identical properties in all directions, the properties of anisotropic materials change with the direction along the object. Anisotropic properties can be a result of differences in the structure or composition along given directions.

In nature, there are many examples of anisotropic structures, e.g., the cellular structure of the skin, leafs of trees or wood which present anisotropy due to their asymmetric structure along given directions, etc. A typical example of anisotropic material is the calcite mineral that presents optical anisotropy because of the difference chemical composition along given directions. Such a type of anisotropy is quite common in the natural world where birefringence and double refractive properties are quite widespread.
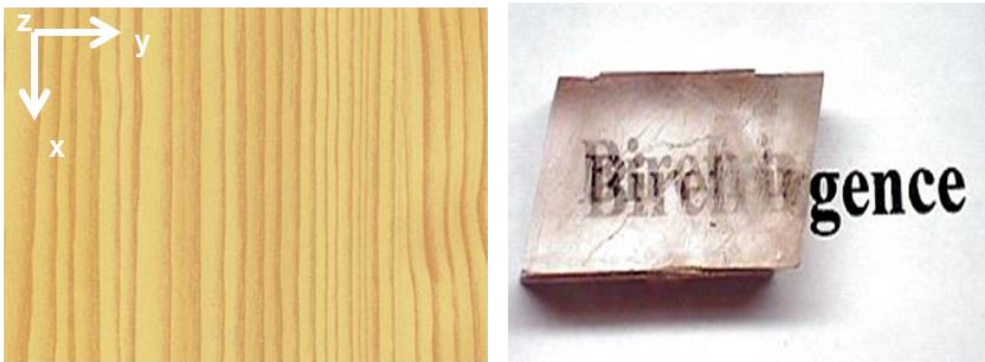
Figure 1.4 *Piece of wood showing structural anisotropy in the x and y axis. (left). Piece of calcite showing an optic effect (Birefringence) due to composition anisotropy in two perpendicular directions(right).*

Processed anisotropic items have found many applications in fields such as Computer Graphics, Geology and Geophysics, Medicine, Microfabrication, Chemistry, Physics and Material Science and engineering. In this latter case, there

are a large number of materials that have been developed to cope with specific functions for optical, magnetic, microfluidics, electro-optical, construction, aeronautics and many other applications[34–38]. For instance, honeycomb structures are employed to fabricate the inner pieces of planes or trains with high compressive and tensile strengths in a preferential direction. This structural anisotropy complies with the conditions of a light material and a high consistency under high pressure which are required in aeronautic applications[37,39].

Our group have employed glancing angle deposition (GLAD) thin films as template to control the growth of anisotropic gold nanoparticles with outstanding properties that are used for encoding of information and advanced anticounterfeiting applications[40]. The motivation of the present work is the systematic development of anisotropic oxide materials by GLAD where the anisotropy of their optical and electrical properties provide new functions as invisible labelling, data encoding, plasmonics or wetting.

1.3.1 Surface roughness and porosity.

The previous sections have implicitly assumed that the development of tilted and/or sculptured nanostructures is the most typical morphological characteristic of GLAD thin films. Herein, it is discussed about other relevant microstructural features such as roughness, preferential association of the nanocolumns (i.e., phenomenon usually denoted as *bundling*) or porosity, features that confer to the GLAD films some of the unique properties required for a large variety of applications. Owing to the importance of bundling within the context of the present work, we will dedicate a specific section to present some basic issues associated with its development.

The termination of the nanocolumnar features at the film surface generates a peculiar topography characterized by a high surface roughness. Surface analysis by atomic force microscopy (AFM) of GLAD evaporated thin films reveals that the RMS surface roughness increases with the deposition angle α and with the thickness of the films [41–43]. This situation is schematically described in Figure 1.5.
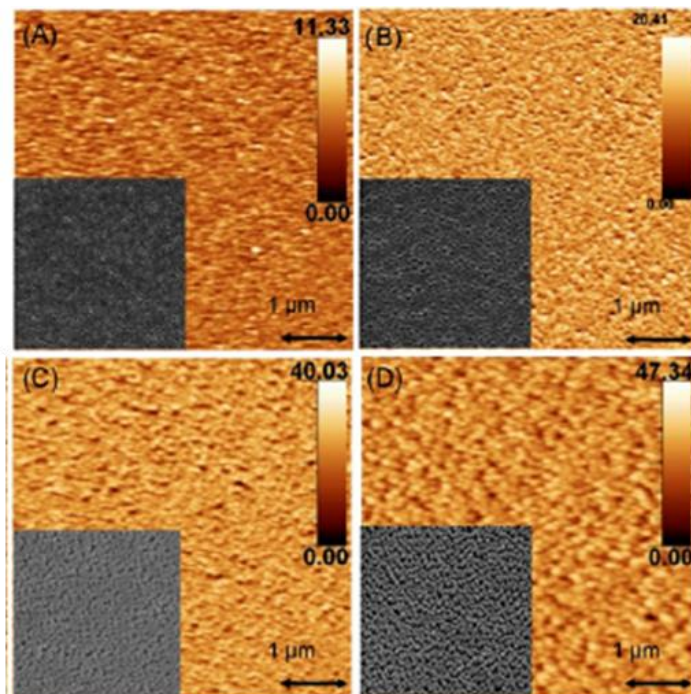
Figure 1.5. *AFM images of TiO₂ GLAD thin films with a similar thickness of 300 nm prepared at deposition angles of 60º 70º, 80º and 85º. For comparison normal SEM images of the surface of these films taken with the same scale (small squares) are included as inset.*[43].

.

For many applications (e.g., sensors, electrochemistry, catalysis, electrochromism, antireflective layers, etc.) the porous character of the GLAD thin films is a key feature for the fabrication of final devices.

An important consequence of the high porosity of GLAD thin films of oxides or other transparent dielectric materials is that, according to the effective medium approximation[44], their optical constants vary by condensation of air or water in their pores. Surprisingly, this effect has been generally overlooked in numerous works using GLAD thin films as antireflective coatings and multilayers for solar cells or other related environmental applications[45,46].

García-García L. et al.[43] have showed that percentage pore volume of TiO₂ GLAD thin films increases with the deposition angle (α), at the same time the meso

and micro porous increases with the deposition angle but in different aspect ratio. This aspect result essential for the properties of thin films and consequently the applications such as have been studied in several works.[40,47]

1.3.2 Separation and association of nanocolumns: bundling effects.

A first assessment of the nanocolumnar arrangement in GLAD thin films might suggest a random distribution of nanocolumns within the film. However, some experimental evidences by AFM and SEM analysis of surface and film morphologies contradict this simple view (Figure 1.5)[43,48,49] For example, in evaporated GLAD thin films, well defined correlation lengths and intercolumnar distances have been determined by SEM and AFM. These correlations are dependent on the deposition conditions and can be formally described with a power law scaling approach[49]. For example, by analyzing the surface SEM micrographs of a series of GLAD thin films Krause et al.[48] identified some repetitive correlation distances between the surface voids separating the nanocolumns that were dependent on deposition parameters. Similarly, by using AFM, Mukherjee et al.[50] were able to determine the period of the surface roughness features in different GLAD thin materials and correlate the obtained values with specific growth exponents.

To confirm the existence of possible correlations between nanocolumns in the interior of the films and not merely at their surface, previous works of our groups have proposed the use of a bulk technique such as GISAXS[10].

By this method it is possible to determine both the tilting orientation of the nanocolumns and the correlation distances existing among them. Figure 1.6 shows a series of GISAXS patterns corresponding to TiO_2 thin films that were prepared by e-beam GLAD at different zenithal angles. While the asymmetric shape of the patterns clearly sustains a tilted orientation of the nanocolumns, the position of the maxima in each pattern provides rather accurate values of correlation distances in the system[10,43]. It is also interesting that these patterns depict a well-defined

maximum suggesting the existence of correlation distances varying between 30 and 200 nm, progressively increasing with film thickness and the deposition angle.
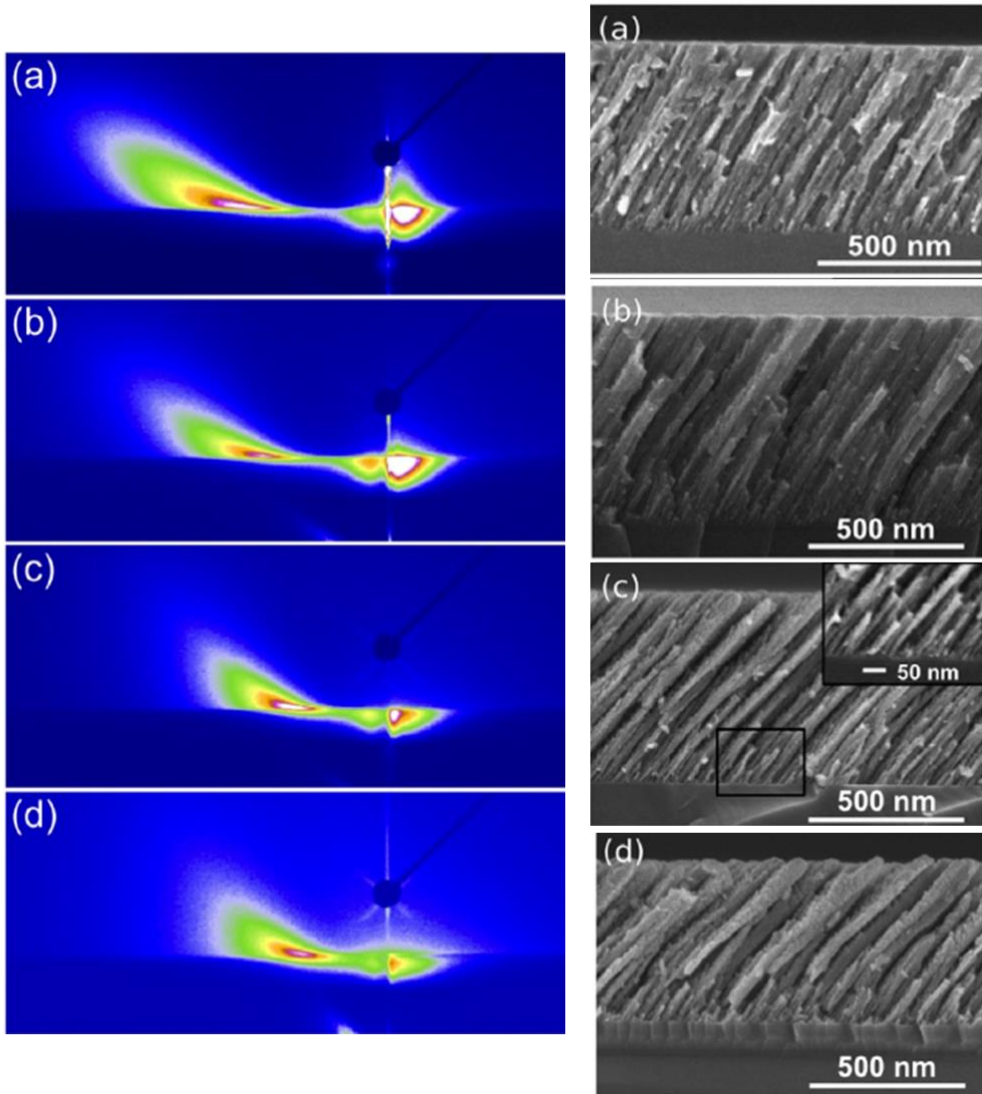
Figure 1.6 *GISAXS and SEM analysis of tilted nanostructures prepared by GLAD.-TiO$_2$ thin films prepared by evaporation at the zenithal angles of 60º, 70º ,80º, 85º (a,b,c,d) respectively (ref. [48]). The GISAXS spectra are asymmetric and depict well defined maxima that can be associated with the correlation distances existing in the system.*

In early studies of evaporated GLAD thin film materials[23,24,51], it was soon recognized that nanocolumns may associate in the form of bundles, i.e., laterally connected associations of nanocolumns arranged in a direction perpendicular to the vapour flux. Later on, bundling association has been reported for GLAD thin films prepared by either evaporation or MS (Magnetron Sputtering)[52,53]. Although the development of this microstructural arrangement has been mainly reported for the case of metal thin films[23,24,51,53], it can be also found for oxides where it has been used as a template structure to develop new composite thin films[40,47]

Surprisingly, except for some detailed discussions in early reviews[24], the bundling phenomenon has not conceited much attention in recent investigations on GLAD thin films. The growth association of nanocolumns in the form of bundles cannot be explained by traditional ballistic processes neither described by the heuristic tangent rule exposed in the previous section. However, some hints about its understanding can be deduced within the context of the so called *surface trapping mechanism* developed in our group[31]. According to it vapour species passing a few angstroms away from the surface may bend its trajectory and be deposited at nearby locations (see figure 1.7(a)).
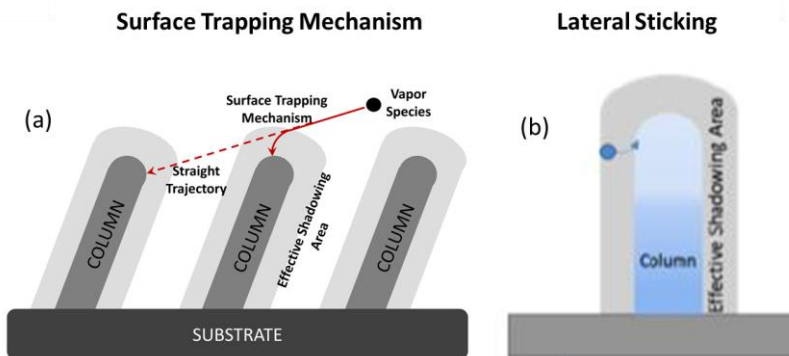
Figure 1.7 a) Illustration of the surface trapping mechanism: unlike typical ballistic models, where vapour species follow straight trajectories, the surface trapping mechanism introduces the possibility that trajectories may bend within an effective shadowing region. b) Illustration of the lateral sticking process, implicit in the trapping mechanism.

This trapping mechanism not only accounts for the tilting angle of the nanoclumns, but also for the formation of bundles. Figure 1.7(b) illustrates that trapping processes may also occur for vapour species passing laterally near a growing nanocolumn. A consequence of such preferential side trapping would be a faster lateral growth of the nanostructures in the direction perpendicular to the vapour flux, ultimately provoking their collapse along this direction

In the present work we will show that the bundling phenomenon is a versatile and powerful tool to get anisotropic optical and electrical properties that can find extremely interesting applications in plasmonic, data encoding invisible labelling and anisotropic wetting.

1.4. Plasma Assisted GLAD

Tuning the nanostructure of GLAD thin films may give rise to new nanostructures with singular surface roughness, organization of nanocolumnar structure or porosity and a large number of experimental strategies are used for this purpose. A first approach is to grow the films on nanostructured substrates where the key issue is to control the shadow casted by a series of patterned hillocks, protrusions or other well-defined features of the surface [54,55]. Another classical way to induce changes in the morphology is to modify the deposition speed, working pressure or substrate temperature[56,57].

A less common approach is to use plasma to modify the microstructure of the deposited GLAD thin films. An example of this possibility is reported in Figure 1.8 showing the development of nanopillar structures by plasma etching[58].
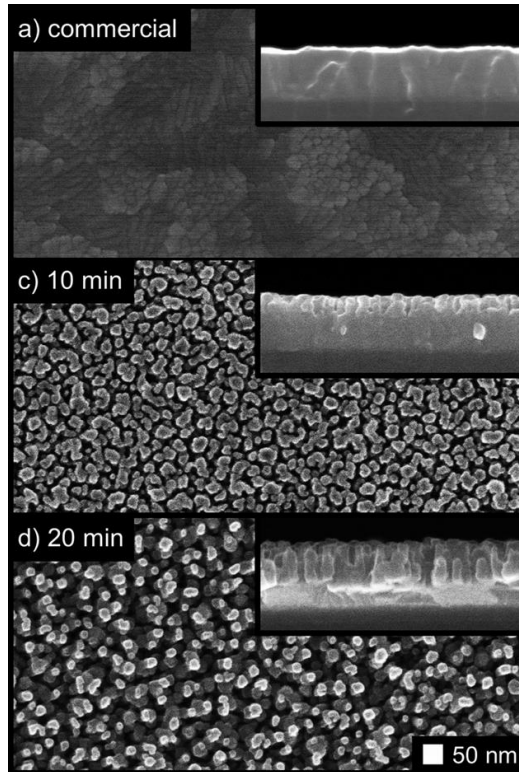
Figure 1.8. SEM images of (a) the original commercial ITO film and (b–d) the nanopillar ITO films with different etch times (indicated in the image)[58].

However, to our knowledge, there are no previous essays where plasma is used to assist the growth of GLAD thin films. Chapters 3 and 4 illustrate the use of plasmas to modify the microstructure of the GLAD thin films during their growth.

1.5 GLAD thin films on flexibles substrates.

Functionalization of polymers to create heterogeneous composites with metallic and magnetic nanoparticles, organic fluorescence molecules or polymers or inorganic thin films constitute emerging routes to develop flexible devices for new electronic, photonic, or controlled wetting applications [59–63]. The main advantage of this type of nanocomposites is its straightforward implementation at industry scale.

In this context, the use of PDMS (polydimethylsiloxane) based composite systems formed by an inorganic thin film deposited on its surface has experienced a rapid expansion during the last years due to the singular nano and microstructures that can be obtained by subjecting them to stretch deformation[64–66]. Figure 1.9 shows some polymer nanocomposites incorporated in plasmonic flexible devices or in stretchable fluorescence composites. In this later case luminescent organic-thin-films transparent in the visible region and that can be used as UV photodetectors have been synthesized on polycarbonate [67].
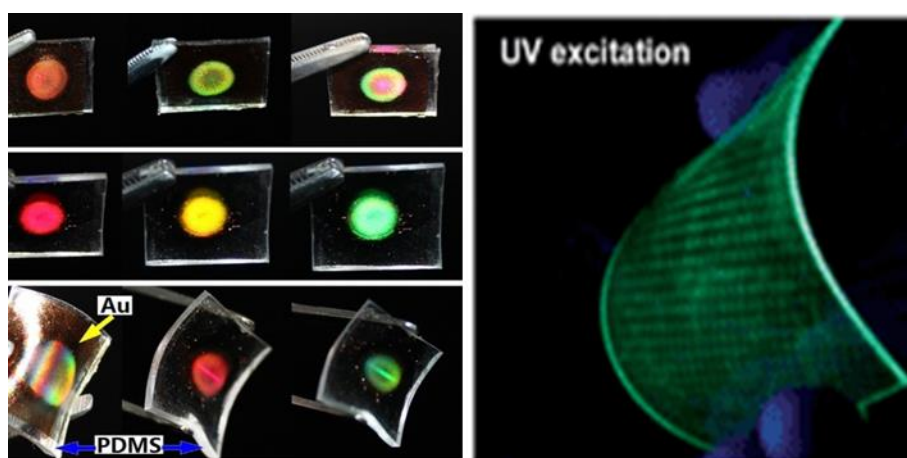
Figure 1.9 *(a) Gold nanoparticles soaked in PDMS. (b) Luminescent 3-hydroxiflavone nanocomposites.*

In the present work we describe a process to fabricate anisotropic surface systems by depositing GLAD thin films on a PDMS substrate which is latter-on subjected to a stretching deformation. The obtained system presents outstanding anisotropic optical and wetting properties (Chapter 5 y 6).

1.6 GLAD thin film properties and applications.

This section discusses some basic notions regarding the optical, electrical and wetting properties and applications that can be found when working with GLAD thin films.

1.6.1 Electrical Properties and applications

Electrical properties of GLAD thin films have been studied by several groups[68–71], showing a series of basic trends in their behaviour.

First, increasing deposition angle (α) leads to an increase of in-plane resistivity because the film density decreases and the number of electrical pathways available for charge conduction decreases[69,71]. The nanostructured character of GLAD thin films leads to different conductivities in the directions parallel and perpendicular to the GLAD nanocolumns[68,71].

Transparent conductor thin films (TCO) are key materials for the development of optoelectronic devices such as displays, sensors or solar cells[9,72,73]. Tin-doped indium oxide (ITO) is likely the most important TCO[6]. Due to its low resistivity (~10^{-4} Ω cm), high transmittance in the visible range (80–90%) and low-deposition temperature, tin-doped indium oxide (ITO) is the most popular TCO in industry[3,74]. Only the need to replace the increasingly costly indium has prompted the search for other alternative TCO[75].

Fabrication of highly porous and/or sculptured ITO thin films has been attempted by e-beam GLAD from ITO pellets both under high vacuum conditions and in a carrier gas flux, generally nitrogen[76–79].

Due to the good electrical performance, high porosity and nanocolumnar structure of ITO-GLAD films, they have been implemented as active component in liquid crystal displays (LCDs) for the alignment of calamitic liquid crystals[73] in the inner or surface of the nanostructure. This alignment produces a high birefringence behaviour (see next section) when is exposed between crossed polarizers such as showed the Figure 1.10 a. Nevertheless, no optical response is obtained when the system is shown between parallel polarizers.(Figure 1.10)
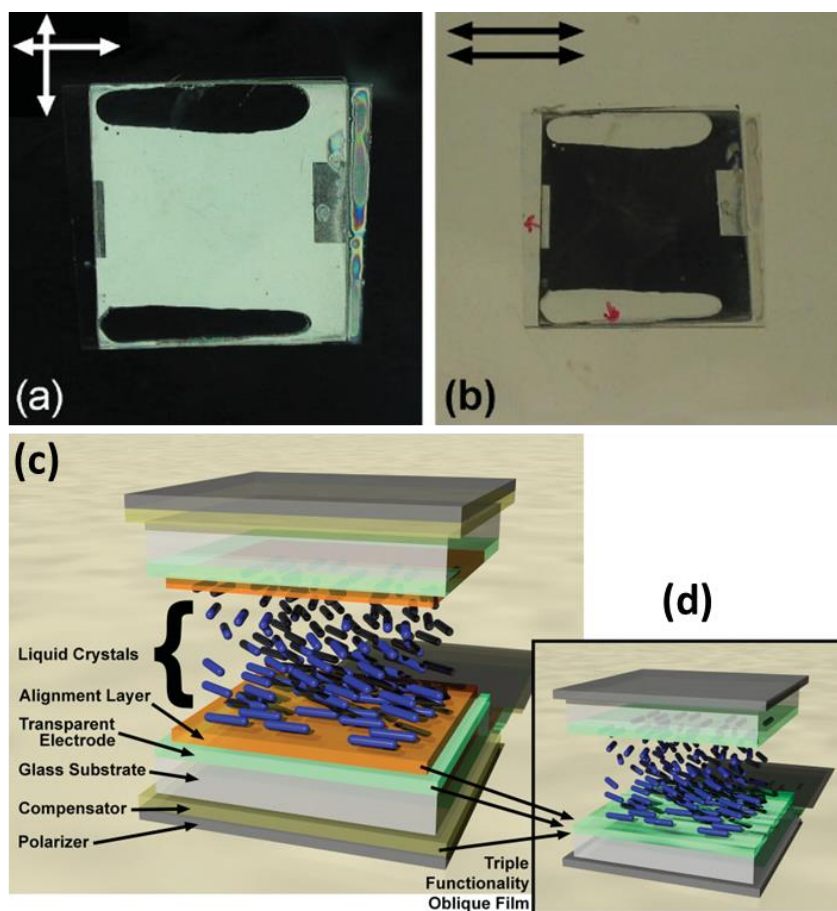
Figure 1.10. *Scheme and performance of devices using GLAD ITO films for liquid crystals alignment (a-b) The liquid crystal E7 is aligned in a twisted nematic configuration by two ITO films deposited at α= 65°. The cell is shown between crossed polarizers in A), and between parallel polarizers in B). The polarizer absorption axes are indicated as arrows. c) Scheme of a common LCD incorporating separate layers acting as transparent electrodes, LC alignment layers and birefringent compensators. d) Unification of the functions of these three components within the ITO nanopillar layer.*

In the present work will be study the singular electrical properties of ITO thin films grown at glancing angle deposition and some plasmonic applications developed with these materials.(Chapter 3)

1.6.2 Optical Properties and applications.

The optical response of GLAD thin films is intimately connected with its structure and composition.

Firstly, using GLAD methods it is possible to wide tune the refractive index of the deposited layer because the film optical constants are determined by its relative density ρ_n which, in turn, is controlled by the deposition angle (α) (Section 1.2).

Secondly, through the geometrical control of the columnar microstructure, ordinary isotropic materials can be endowed with complex optical anisotropies (e.g. birefringence, dichroism).

1.6.2.1 Optical anisotropy in columnar glancing angle deposition.

Ever since the earliest studies of oblique deposition[80,81], it has been realized that the tilted columnar microstructure of obliquely deposited films generates an optical anisotropy. Thus, even if the constituent material in is isotropic, lateral connectivity and bundling formation induce he development of an asymmetric columnar structure and hence the generation of an anisotropic optical response.

Figure 1.11 shows a series of GLAD nanostructures with, respectively biaxial and uniaxial optical characteristics. In general, the different nanostructures can be characterized by three structural axes: "B", the axis corresponding with the bulk nanocolumnar growth, "g" the axis corresponding with material flux direction (growing), "b" the axis corresponding with the preferential aggregation direction of nanocolumns (bundling). Figure 1.11 a) and b) lead to biaxial anisotropy, where the film optical properties are specified by a refractive index tensor with three distinct principal indices n_b, n_g and n_B respectively oriented along the x, y and z axes. (c) The low-symmetry scheme. Figure d and e shows a more symmetric microstructure where the refractive index tensor contains only two unique principal indices $n_b = n_g$, and n_B. This microstructure presents uniaxial anisotropy (f),
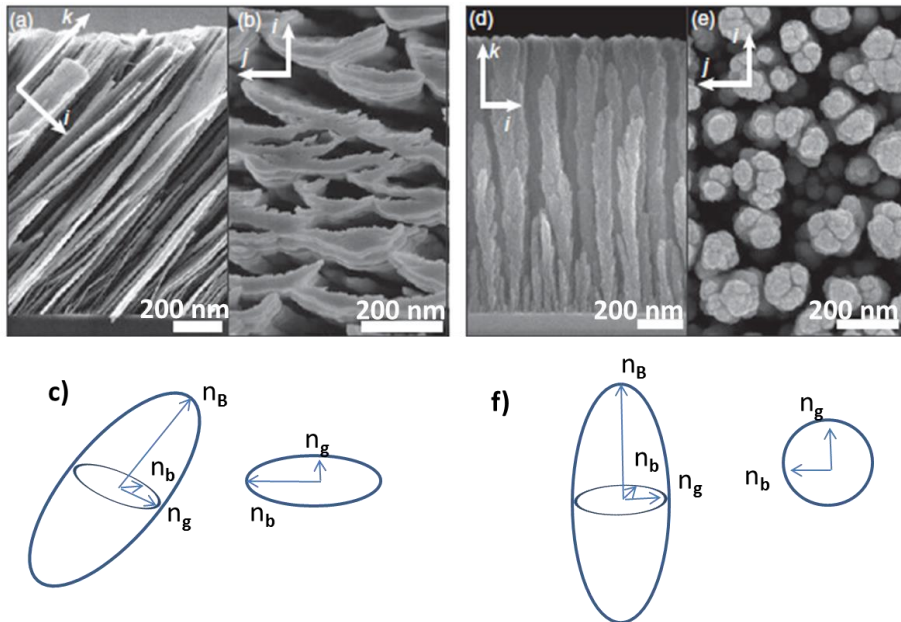
***Figure 1.11 (left*)** *Cross and top view SEM micrographs of (a,b) biaxial anisotropy TiO$_2$ GLAD thin films and (d,e) uniaxial anisotropy TiO$_2$ thin films(.c, f) Biaxial and uniaxial anisotropy scheme*[2].

When developing GLAD materials for polarization devices, a key issue is the planar birefringence, defined as the difference between the refractive indexes along the slow axis (*bundling*-axis) and the fast axis (*growing*-axis) for light at normal incidence. The fast axis is perpendicular to the slow axis and lies in the substrate plane. Usually the fast axis corresponds to the smaller refractive index, while the slow axis corresponds to the higher refractive index. This difference between refractive indexes produces change in the polarization state of the light.

In general, the planar birefringence can be written:

$$\Delta n = n_s - n_y. \qquad\qquad (1)$$

Figure 1.12 shows values of the planar birefringence (Δn) for several GLAD inorganic oxides as a function of the deposition angle (α).
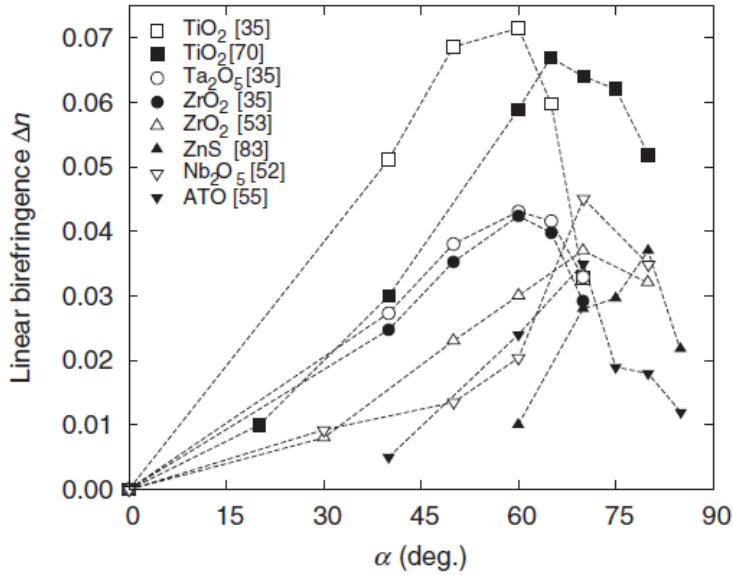
Figure 1.12. *Planar birefringence values measured for several materials, showing the complex α-dependence of the birefringence*[2,29].

1.6.2.2 Plasmonics. Applications

At certain incident conditions, when the incident light frequency matches the intrinsic frequency of the free electrons, a resonant absorption occurs for metals with a high concentration of free electrons. This phenomenon is called surface plasmon resonance (SPR) or, in the case of nanometric metallic structures, localized surface plasmon resonance (LSPR).
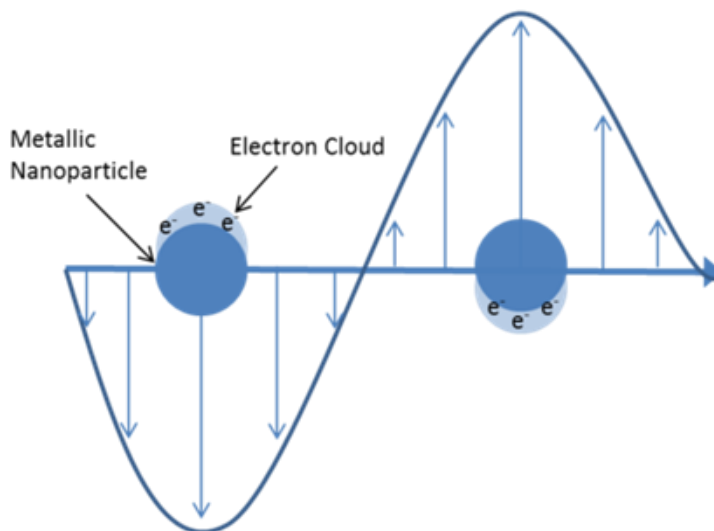
Figure 1.13. *Schematic showing surface plasmon resonance (SPR) for a metallic sphere.*

The peculiar morphologies and microstructures generated by GLAD have been widely used to grow metallic nanoparticles and nanostructures, either self-sustained or embedded in a host matrix formed by a transparent thin film prepared by this method. Specially, SiO_2 GLAD thin films have been used for this latter purpose due their high transmittance in the visible region. For example, anisotropic SiO_2 nanocolumnar films have been used as templates for the fabrication of dichroic Ag films by direct DC sputtering deposition of silver on their surface[47] Laser post-treatment silver melting has been used for optical encryption of information at micron level.

Recently, we have developed in our group a host-guest strategy based on the formation of anisotropic Au nanodiscs inside the intercolumnar space of a bundled SiO_2 GLAD thin film[40] .

These composite materials have been applied for optical encryption of information after laser treatment (Figure 1.14a), so that the distinct colours of the untreated zones are due to the different anisotropies of the gold nanoparticles depending on the characteristics of the SiO2 host layer. This laser treatment

removes the dichroic character of the gold nanoparticles in selected zones with control at the micron scale ((Figure 1.14b)).
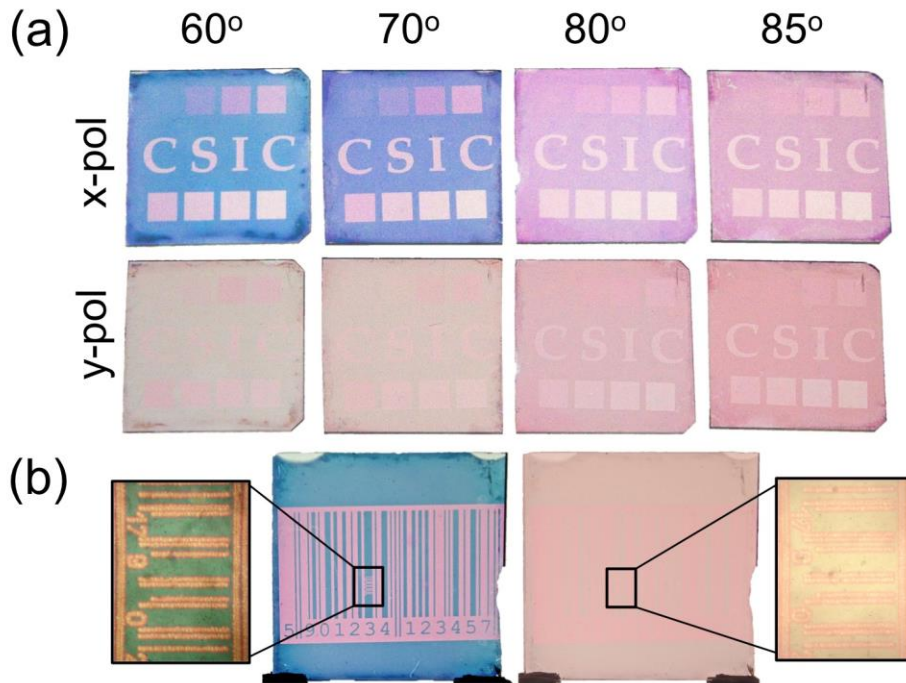
Figure 1.14. *a) Pictures taken with x- and y-polarized lights for a series of dichroic Au/SiO2 samples deposited at α= 60, 70, 80 and 85º. Selected zones of these samples were treated with laser at different powers: b) Standard bar code written with the laser onto a Au/SiO2-60º sample and monitored with x- and y-polarized lights*[40]

1.6.3 Wetting Properties and applications

Mimicking the nature to obtain superhydrophobic/superhydrophilic, adhesive/anti-adhesive and, lately, omniphobic and wetting-anisotropic surfaces has been a topic of constant interest in Nanotechnology during the last two decades, with converging efforts from academy and industry towards the search of new surface functionalities[82,83].

The wetting angle of a drop on a flat surface is determined by the Young Law and is the result of the balance among the cohesive forces acting at the contact line between the drop, the solid surface and the air or gas environment[84].

GLAD techniques have been extensively utilized to control the wetting properties of materials because they provide a fine control over both surface chemistry and roughness. Important achievements have been the fabrication of surfaces with singular adhesives properties[85], hydrophobicity[86–88] superhydrophobicity[89–91], superhydrophilicity[92] or superolephobicity[93,94].

Figure 1.15a,b showe an example of a droplet wetting anisotropy on a patterned surface[59,95]. The droplet presents a spherical shape when is deposited on smooth surface. However, when a patterned surface is created, the droplet adopts an elongated, parallel-sided shape. In most occasions, the formation and control of droplet wetting anisotropy is the first step to develop anisotropic wetting devices for wetting and microfluidics applications such as the one shown in Figure 1.15c. This example illustrates the use of GLAD to fabricate anisotropic films with unidirectional adhesive and wetting properties[38]. It shows the use of glancing angle technique for the fabrication of Parylene (PPX) nanorods depicting a pin-release droplet ratchet mechanism derived from their singular nanoscale microstructure. These nanofilms exhibited a difference of 80 μN in the droplet retention forces between the pin and release directions, this latter characterized by a microscale smooth surface on which microliter droplets are preferentially transported.
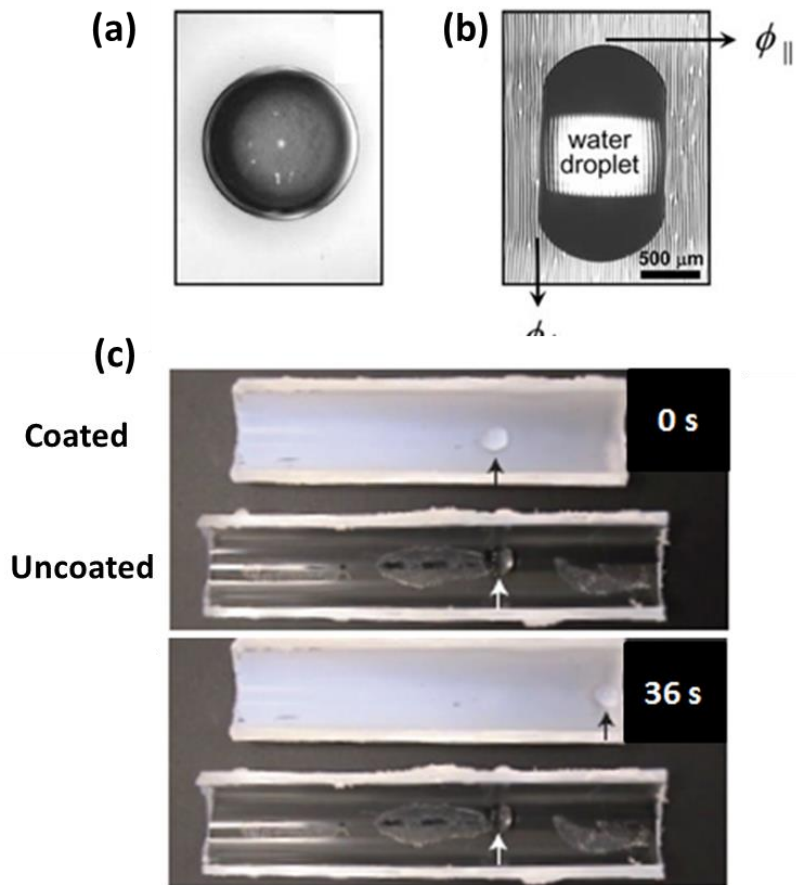
Figure 1.15. *Top view optical micrograph of 2 mL water droplet on the smooth surface (a) and patterned surface (b), revealing an elongated, parallel-sided shape; C) Time-lapse of droplet motion in the coated and uncoated half pipes. Water drops moved axially on the half-pipe coated with the PPX nanofilm, whereas those on the uncoated half-pipe merely vibrated randomly[59,95].*

In the present work dealing with anisotropic properties of GLAD thin films, we have focussed on the development of anisotropic-wetting applications. The interest on this topic stems from the industrial need of materials capable of inducing a preferentially oriented liquid spreading or rendering asymmetrical adhesive surfaces

1.7 Objetives

The main objective of this thesis is the control, enhance and manipulation of anisotropic microstructural properties of thin films prepared at glancing angle deposition to develop advanced functional applications. From this general objective, more concrete goals are also within the intention of this thesis, namely:

- To optimize the plasma assisted at glancing angle deposition process.

- To develop and synthesis porous ITO thin films by plasma assisted at glancing angle deposition with optimal optical transparency and electrical conductivity. To study the microstructural influence of plasma assisted during the growth.

- To characterize and study of the electrical and optical properties of ITO thin films at glancing angle deposition derivated of their structural anisotropy.

- To fabricate electronic and optical devices for plasmonic and encoding date applications using the anisotropic microstructure of ITO GLAD thin films.

- To study and optimize thin films at glancing angle deposition on flexible polymers. To study the microstructural changes and how it affect, the properties under mechanic deformations.

- To study the thin film-polymer interactions and reversibility after mechanic deformations.

- To optimize the optical and wetting properties generated in the nanocomposite before, during and after mechanic stress.

- To fabricate optical and wetting devices for inviable labeling and wetting control with the nanocomposites generated.

1.16 Thesis scheme.

In-plane anisotropic nanocolumnar films for advanced functional materials

Objective		Why
Control, enhance and manipulation of anisotropy		Modification of electrical, optical and wetting properties

How

Plasma assisted	Mechanical deformations
Nanoscale	Microscale
ITO thin films	SiO$_2$ and TiO$_2$/PDMS
Applications: ➢ Dihcroic systems ➢ Waveplates ➢ Encryption devices	➢ Invisible labeling ➢ Wetting devices
Chapter 3 and 4	Chapter 5 y 6

Figure 1.16. *Thesis scheme.*

REFERENCES

(1)   Venables, J. A. *Introduction to Surface and Thin Film Processes*; Cambridge University Press: Cambridge, 2000.

(2)   Hawkeye, M. M.; Taschuk, M. T.; Brett, M. J. *Glancing angle deposition of thin films: engineering the nanoscale*; 2014.

(3)   Granqvist, C. G. *Sol. Energy Mater. Sol. Cells* **2007**, *91* (17), 1529–1598.

(4)   Ohring, M. In *Materials Science of Thin Films (Second Edition)*; Ohring, M., Ed.; Academic Press: San Diego, 2002; pp 1–56.

(5)   Kern, W. *Thin Film Processes II*; Academic Press, 2012.

(6)   Granqvist, C. G.; Hultåker, A. *Thin Solid Films* **2002**, *411* (1), 1–5.

(7)   Cao, Q.; Kim, H.; Pimparkar, N.; Kulkarni, J. P.; Wang, C.; Shim, M.; Roy, K.; Alam, M. A.; Rogers, J. A. *Nature* **2008**, *454* (7203), 495–500.

(8)   Malenfant, P. R. L.; Dimitrakopoulos, C. D.; Gelorme, J. D.; Kosbar, L. L.; Graham, T. O.; Curioni, A.; Andreoni, W. *Appl. Phys. Lett.* **2002**, *80* (14), 2517–2519.

(9)   Nomura, K.; Ohta, H.; Ueda, K.; Kamiya, T.; Hirano, M.; Hosono, H. *Science* **2003**, *300* (5623), 1269–1272.

(10)   González-García, L.; Barranco, A.; Páez, A. M.; González-Elipe, A. R.; García-Gutiérrez, M.-C.; Hernández, J. J.; Rueda, D. R.; Ezquerra, T. A.; Babonneau, D. *ChemPhysChem* **2010**, *11* (10), 2205–2208.

(11)   Kim, J. K.; Chhajed, S.; Schubert, M. F.; Schubert, E. F.; Fischer, A. J.; Crawford, M. H.; Cho, J.; Kim, H.; Sone, C. *Adv. Mater.* **2008**, *20* (4), 801–804.

(12)   Tsukazaki, A.; Ohtomo, A.; Onuma, T.; Ohtani, M.; Makino, T.; Sumiya, M.; Ohtani, K.; Chichibu, S. F.; Fuke, S.; Segawa, Y.; Ohno, H.; Koinuma, H.; Kawasaki, M. *Nat. Mater.* **2005**, *4* (1), 42–46.

(13)   Mamat, M. H.; Sahdan, M. Z.; Khusaimi, Z.; Ahmed, A. Z.; Abdullah, S.; Rusop, M. *Opt. Mater.* **2010**, *32* (6), 696–699.

(14)   Jiang, B.; Ren, C.; Zheng, Z.; Liu, X.; Fan, H.; Yao, L.; Li, Y.; Su, X. *Nucl. Instrum. Methods Phys. Res. Sect. B Beam Interact. Mater. At.* **2004**, *215* (3-4), 413–418.

(15)   Schmidt, D.; Kjerstad, A. C.; Hofmann, T.; Skomski, R.; Schubert, E.; Schubert, M. *J. Appl. Phys.* **2009**, *105* (11).

(16)   Albrecht, O.; Zierold, R.; Patzig, C.; Bachmann, J.; Sturm, C.; Rheinländer, B.; Grundmann, M.; Görlitz, D.; Rauschenbach, B.; Nielsch, K. *Phys. Status Solidi B* **2010**, *247* (6), 1365–1371.

(17)   Deepa, M.; Srivastava, A. K.; Sood, K. N.; Agnihotry, S. A. *Nanotechnology* **2006**, *17* (10), 2625–2630.

(18)   Kasik, I.; Mrazek, J.; Podrazky, O.; Seidl, M.; Aubrecht, J.; Tobiska, P.; Pospisilova, M.; Matejec, V.; Kovacs, B.; Markovics, A.; Szili, M. *Sens. Actuators B Chem.* **2009**, *139* (1), 139–142.

(19)   Marcu, A.; Viespe, C. *Sens. Actuators B Chem.* **2015**, *208*, 1–6.

(20)   Glover, R. E. *Science* **1970**, *169* (3948), 850–850.

(21) Strafford, K. N. *Surface Engineering: Processes and Applications*; CRC Press, 1994.

(22) Tang, F.; Parker, T.; Wang, G.-C.; Lu, T.-M. *J. Phys. Appl. Phys.* **2007**, *40* (23), R427.

(23) Abelmann, L.; Lodder, C. *Thin Solid Films* **1997**, *305* (1–2), 1–21.

(24) Van Kranenburg, H.; Lodder, C. *Mater. Sci. Eng. R Rep.* **1994**, *11* (7), 295–354.

(25) Robbie, K.; Brett, M. J. *J. Vac. Sci. Technol. Vac. Surf. Films* **1997**, *15* (3), 1460–1465.

(26) Poxson, D. J.; Mont, F. W.; Schubert, M. F.; Kim, J. K.; Schubert, E. F. *Appl. Phys. Lett.* **2008**, *93* (10).

(27) Main, E. *J. Appl. Phys.* **2004**, *95* (8).

(28) Zhou, Q.; Li, Z.; Ni, J.; Zhang, Z. *Mater. Trans.* **2011**, *52* (3), 469–473.

(29) Hodgkinson, I.; Wu, Q. hong; Hazel, J. *Appl. Opt.* **1998**, *37* (13), 2653–2659.

(30) Tait, R. N.; Smy, T.; Brett, M. J. *Thin Solid Films* **1993**, *226* (2), 196–201.

(31) Alvarez, R.; Lopez-Santos, C.; Parra-Barranco, J.; Rico, V.; Barranco, A.; Cotrino, J.; Gonzalez-Elipe, A. R.; Palmero, A. *J. Vac. Sci. Technol. B* **2014**, *32* (4).

(32) Álvarez, R.; González-García, L.; Romero-Gómez, P.; Rico, V.; Cotrino, J.; González-Elipe, A. R.; Palmero, A. *J. Phys. Appl. Phys.* **2011**, *44* (38), 385302.

(33) Lintymer, J.; Martin, N.; Chappé, J.-M.; Delobelle, P.; Takadoum, J. *Surf. Coat. Technol.* **2005**, *200* (1-4), 269–272.

(34) Sánchez-Valencia, J. R.; Toudert, J.; Borras, A.; López-Santos, C.; Barranco, A.; Feliu, I. O.; González-Elipe, A. R. *Plasmonics* **2010**, *5* (3), 241–250.

(35) Gambardella, P.; Rusponi, S.; Veronese, M.; Dhesi, S. S.; Grazioli, C.; Dallmeyer, A.; Cabria, I.; Zeller, R.; Dederichs, P. H.; Kern, K.; Carbone, C.; Brune, H. *Science* **2003**, *300* (5622), 1130–1133.

(36) Aieta, F.; Genevet, P.; Yu, N.; Kats, M. A.; Gaburro, Z.; Capasso, F. *Nano Lett.* **2012**, *12* (3), 1702–1706.

(37) Belouettar, S.; Abbadi, A.; Azari, Z.; Belouettar, R.; Freres, P. *Compos. Struct.* **2009**, *87* (3), 265–273.

(38) Malvadkar, N. A.; Hancock, M. J.; Sekeroglu, K.; Dressick, W. J.; Demirel, M. C. *Nat. Mater.* **2010**, *9* (12), 1023–1028.

(39) Chen, D. H. *Compos. Struct.* **2011**, *93* (2), 736–746.

(40) Gonzalez-García, L.; Parra-Barranco, J.; Sanchez-Valencia, J. R.; Ferrer, J.; Garcia-Gutierrez, M.-C.; Barranco, A.; Gonzalez-Elipe, A. R. *Adv. Funct. Mater.* **2013**, *23* (13), 1655–1663.

(41) Lintymer, J.; Martin, N.; Chappe, J.-M.; Takadoum, J. *Wear* **2008**, *264* (5-6), 444–449.

(42) Rico, V.; Borrás, A.; Yubero, F.; Espinós, J. P.; Frutos, F.; González-Elipe, A. R. *J. Phys. Chem. C* **2009**, *113* (9), 3775–3784.

(43) González-García, L.; Parra-Barranco, J.; Sánchez-Valencia, J. R.; Barranco, A.; Borrás, A.; González-Elipe, A. R.; García-Gutiérrez, M.-C.; Hernández, J. J.; Rueda, D. R.; Ezquerra, T. A. *Nanotechnology* **2012**, *23* (20).

(44) Aspnes, D. E. *Thin Solid Films* **1982**, *89* (3), 249–262.

(45) Xi, J.-Q.; Schubert, M. F.; Kim, J. K.; Schubert, E. F.; Chen, M.; Lin, S.-Y.; Liu, W.; Smart, J. A. *Nat. Photonics* **2007**, *1* (3), 176–179.

(46) Chattopadhyay, S.; Huang, Y. F.; Jen, Y. J.; Ganguly, A.; Chen, K. H.; Chen, L. C. *Mater. Sci. Eng. R Rep.* **2010**, *69* (1–3), 1–35.

(47) Sanchez-Valencia, J. R.; Toudert, J.; Borras, A.; Barranco, A.; Lahoz, R.; de la Fuente, G. F.; Frutos, F.; Gonzalez-Elipe, A. R. *Adv. Mater.* **2011**, *23* (7), 848–853.

(48) Krause, K. M.; Thommes, M.; Brett, M. J. *Microporous Mesoporous Mater.* **2011**, *143* (1), 166–173.

(49) Buzea, C.; Beydaghyan, G.; Elliott, C.; Robbie, K. *Nanotechnology* **2005**, *16* (10), 1986–1992.

(50) Mukherjee, S.; Gall, D. *J. Appl. Phys.* **2010**, *107* (8).

(51) Hara, K.; Kamiya, M.; Hashimoto, T.; Okamoto, K.; Fujiwara, H. *Thin Solid Films* **1988**, *158* (2), 239–244.

(52) Ehsani, M. H.; Rezagholipour Dizaji, H.; Azizi, S.; Ghavami Mirmahalle, S. F.; Hosseini Siyanaki, F. *Phys. Scr.* **2013**, *88* (2).

(53) Itoh, K.; Ichikawa, F.; Takahashi, Y.; Tsutsumi, K.; Noguchi, Y.; Okamoto, K.; Uchiyama, T.; Iguchi, I. *Jpn. J. Appl. Phys.* **2006**, *45* (4R).

(54) Zhou, C. M.; Li, H. F.; Gall, D. *Thin Solid Films* **2008**, *517* (3), 1214–1218.

(55) Zhou, C. M.; Gall, D. *Thin Solid Films* **2007**, *516* (2-4), 433–437.

(56) Xue, C.-H.; Jia, S.-T.; Zhang, J.; Ma, J.-Z. *Sci. Technol. Adv. Mater.* **2010**, *11* (3).

(57) Flickyngerová, S.; Netrvalová, M.; Šutta, P.; Novotný, I.; Tvarožek, V.; Gašpierik, P.; Bruncko, J. *Thin Solid Films* **2011**, *520* (4), 1233–1237.

(58) Jaron G. Van Dijken, M. J. B. *J. Vac. Sci. Amp Technol. Vac. Surf. Films* **2012**, *30* (4).

(59) Chung, J. Y.; Youngblood, J. P.; Stafford, C. M. *Soft Matter* **2007**, *3* (9).

(60) Cortecchia, E.; Pacilli, A.; Pasquinelli, G.; Scandola, M. *Biomacromolecules* **2010**, *11* (9), 2446–2453.

(61) Drzaic, P. S. *J. Appl. Phys.* **1986**, *60* (6), 2142–2148.

(62) Ibn-Elhaj, M.; Schadt, M. *Nature* **2001**, *410* (6830), 796–799.

(63) Calvo, M. E.; González-García, L.; Parra-Barranco, J.; Barranco, A.; Jiménez-Solano, A.; González-Elipe, A. R.; Míguez, H. *Adv. Opt. Mater.* **2015**, *3* (2), 272–272.

(64) Efimenko, K.; Rackaitis, M.; Manias, E.; Vaziri, A.; Mahadevan, L.; Genzer, J. *Nat. Mater.* **2005**, *4* (4), 293–297.

(65) Chung, J. Y.; Nolte, A. J.; Stafford, C. M. *Adv. Mater.* **2011**, *23* (3), 349–368.

(66) Kim, P.; Hu, Y.; Alvarenga, J.; Kolle, M.; Suo, Z.; Aizenberg, J. *Adv. Opt. Mater.* **2013**, *1* (5), 381–388.

(67) Aparicio, F. J.; Alcaire, M.; Borras, A.; Gonzalez, J. C.; López-Arbeloa, F.; Blaszczyk-Lezak, I.; González-Elipe, A. R.; Barranco, A. *J. Mater. Chem. C* **2014**, *2* (32), 6561.

(68) Okamoto, K.; Itoh, K. *Jpn. J. Appl. Phys. Part 1 Regul. Pap. Short Notes Rev. Pap.* **2005**, *44* (3), 1382–1388.

(69) Lintymer, J.; Gavoille, J.; Martin, N.; Takadoum, J. *Surf. Coat. Technol.* **2003**, *174*, 316–323.

(70) Kuwahara, K.; Shinzato, S. *Thin Solid Films* **1988**, *164* (C), 165–168.

(71) Vick, D.; Brett, M. J. *J. Vac. Sci. Technol. Vac. Surf. Films* **2006**, *24* (1), 156–164.

(72) Beaudry, A. L.; LaForge, J. M.; Tucker, R. T.; Li, P.; Taschuk, M. T.; Brett, M. J. *Cryst. Growth Des.* **2013**, *13* (1), 212–219.

(73) Harris, K. D; van Popta, A. C.; Sit, J. C.; Broer, D. J.; Brett, M. J. *Adv. Funct. Mater.* **2008**, *18* (15), 2147–2153.

(74) Yamada, A.; Takakura, W.; Ikeda, S.; Ueda, Y. *Phys. Status Solidi Appl. Res.* **2002**, *189* (3), 753–757.

(75) Kumar, A.; Zhou, C. *ACS Nano* **2010**, *4* (1), 11–14.

(76) Kim, S. I.; Jung, T. D.; Song, P. K. *Thin Solid Films* **2010**, *518* (11), 3085–3088.

(77) Jung, Y. S.; Lee, S. S. *J. Cryst. Growth* **2003**, *259* (4), 343–351.

(78) Ikenoue, T.; Sakamoto, S.; Inui, Y. *Phys. Status Solidi C* **2014**, *11* (7-8), 1237–1239.

(79) Mahieu, S.; Ghekiere, P.; De Winter, G.; Depla, D.; De Gryse, R.; Lebedev, O. I.; Van Tendeloo, G. *Thin Solid Films* **2005**, *484* (1-2), 18–25.

(80) Lewis, B. *J. Vac. Sci. Technol.* **1967**, *4* (5).

(81) Nakhodkin, N. G.; Shaldervan, A. I. *Thin Solid Films* **1972**, *10* (1), 109–122.

(82) Tuteja, A.; Choi, W.; Ma, M.; Mabry, J. M.; Mazzella, S. A.; Rutledge, G. C.; McKinley, G. H.; Cohen, R. E. *Science* **2007**, *318* (5856), 1618–1622.

(83) Feng, X. J.; Jiang, L. *Adv. Mater.* **2006**, *18* (23), 3063–3078.

(84) Mittal, K. L. *Contact Angle, Wettability and Adhesion*; CRC Press, 2006.

(85) Rahmawan, Y.; Xu, L.; Yang, S. *J. Mater. Chem. A* **2013**, *1* (9).

(86) Kannarpady, G. K.; Khedir, K. R.; Ishihara, H.; Woo, J.; Oshin, O. D.; Trigwell, S.; Ryerson, C.; Biris, A. S. *ACS Appl. Mater. Interfaces* **2011**, *3* (7), 2332–2340.

(87) Khedir, K. R.; Kannarpady, G. K.; Ishihara, H.; Woo, J.; Ryerson, C.; Biris, A. S. *Langmuir* **2011**, *27* (8), 4661–4668.

(88) A. Bayat, M. E. *Vacuum* **2014**, *101*, 279–282.

(89) Tsoi, S.; Fok, E.; Sit, J. C.; Veinot, J. G. C. *Langmuir ACS J. Surf. Colloids* **2004**, *20* (24), 10771–10774.

(90) Dawood, M. K.; Zheng, H.; Kurniawan, N. A.; Leong, K. C.; Foo, Y. L.; Rajagopalan, R.; Khan, S. A.; Choi, W. K. *Soft Matter* **2012**, *8* (13), 3549–3557.

(91) Dawood, M. K.; Zheng, H.; Liew, T. H.; Leong, K. C.; Foo, Y. L.; Rajagopalan, R.; Khan, S. A.; Choi, W. K. *Langmuir* **2011**, *27* (7), 4126–4133.

(92) Macias-Montero, M.; Filippin, A. N.; Saghi, Z.; Aparicio, F. J.; Barranco, A.; Espinos, J. P.; Frutos, F.; Gonzalez-Elipe, A. R.; Borras, A. *Adv. Funct. Mater.* **2013**, *23* (48), 5981–5989.

(93) Fujii, T.; Sato, H.; Tsuji, E.; Aoki, Y.; Habazaki, H. *J. Phys. Chem. C* **2012**, *116* (44), 23308–23314.

(94) Fujii, T.; Aoki, Y.; Habazaki, H. *Langmuir* **2011**, *27* (19), 11752–11756.

(95)   Lee, S. G.; Lim, H. S.; Lee, D. Y.; Kwak, D.; Cho, K. *Adv. Funct. Mater.* **2013**, *23* (5), 547–553.

Chapter 2

Resumen en español

Durante los últimos años, el desarrollo de películas delgadas de óxidos depositadas a ángulo rasante (GLAD) es un tema de gran interés tanto científico y tecnológico[1–3]. Esto es debido a que la técnica permite la fabricación de láminas nanoestructuradas que pueden ser usadas para la creación de distintos dispositivos y aplicaciones[4–8]. Una característica esencial de este tipo de materiales es que presentan estructuras anisotrópicas en forma de nanocolumnas porosas e inclinadas de formas complejas y diversas[9–11].

Esta investigación se ha centrado en la fabricación de láminas delgadas para modificar y controlar su microestructura con el objeto de mejorar o innovar en sus propiedades y propiciar nuevas aplicaciones de los dispositivos en los que se integran. En esta tesis se han abordado diferentes campos de aplicación en electro-óptica, óptica y microfluídica, usando para ello tres óxidos inorgánicos de diferente naturaleza química: Óxido de Indio dopado con Estaño (ITO), óxido de titanio (TiO_2) y óxido de silicio (SiO_2).

En esta investigación se ha perseguido la generación de aplicaciones y dispositivos que modulen las propiedades básicas de estos materiales mediante el control y modificación de su microestructura y porosidad para abrir nuevas áreas de aplicación. En concreto el desarrollo de capas nanoestructuradas de ITO por crecimiento a ángulo rasante es una primera área de trabajo de gran crecimiento durante los últimos años, particularmente cuando este óxido conductor y transparente se prepara en forma de material poroso.

Otro elemento novedoso abordado en esta tesis se refiere a la integración de estos materiales nanoestructurados sobre sustratos flexibles con el objetivo de estudiar la evolución de sus propiedades y propiciar su posible transferencia a nivel industrial.

2.1 Microestructura mediante deposición en ángulo rasante. Anisotropía estructural.

La deposición de capas delgadas a ángulo rasantes (GLAD), también conocida como deposición a ángulos oblicuos (OAD) consiste en la deposición física desde fase vapor en esta configuración geométrica lo que permite fabricar películas delgadas con una morfología porosa y topología columnar.

El crecimiento columnar direccional es el resultado de un mecanismo de sombra (shadowing)[12,13] que ocurre en la superficie del sustrato durante la deposición de material evaporado, tal y como se muestra en la Fig.2.1.
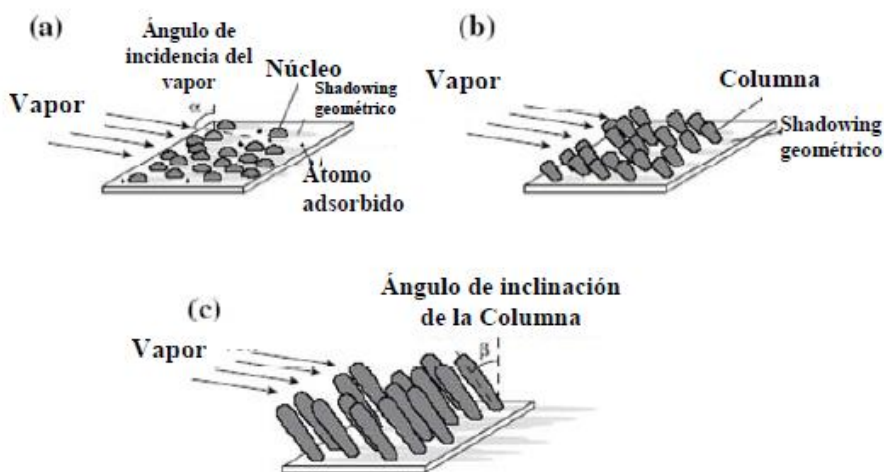
Fig 2.1: *Mecanismo de crecimiento columnar. En las primeras etapas de crecimiento a), se condensan átomos y forman núcleos que producen un efecto de sombra tras ellas, impidiendo la deposición de material (b). La película resultante se compone de columnas crecidas a partir de los núcleos que aparecen inclinadas en la dirección del flujo de vapor(c).*

Durante el intervalo inicial del crecimiento de una película, se condensan átomos procedentes de la sublimación en el sustrato y forman islas separadas individualmente o "núcleos". (Véase en Capítulo 1, los modelos de crecimiento. Trapping). Cuando el sustrato está inclinado con respecto a la dirección del vapor, este incide a ángulos oblicuos de forma que los núcleos proyectan un cono de sombra sobre el sustrato, impidiendo la deposición en esa zona, evitando la coalescencia de los núcleos y la formación de una capa continua. Los núcleos iniciales crecen mediante captura de nuevos átomos evaporados, lo que origina la formación de columnas inclinadas que crecen en la dirección de aporte del vapor[12–14]

Mediante esta técnica se han llegado a producir nanoestructuras columnares de gran complejidad, como nanoestructuras periódicas, perforadas o de porosidad gradual para el uso en multitud de aplicaciones que van desde sensores hasta filtros ópticos, dispositivos microfluídicos, magnéticas y catalíticos[5,7,8,15–19]. Ejemplos de microestructuras de capas GLAD con carácter "escultural" se presentan en la Fig.2.2
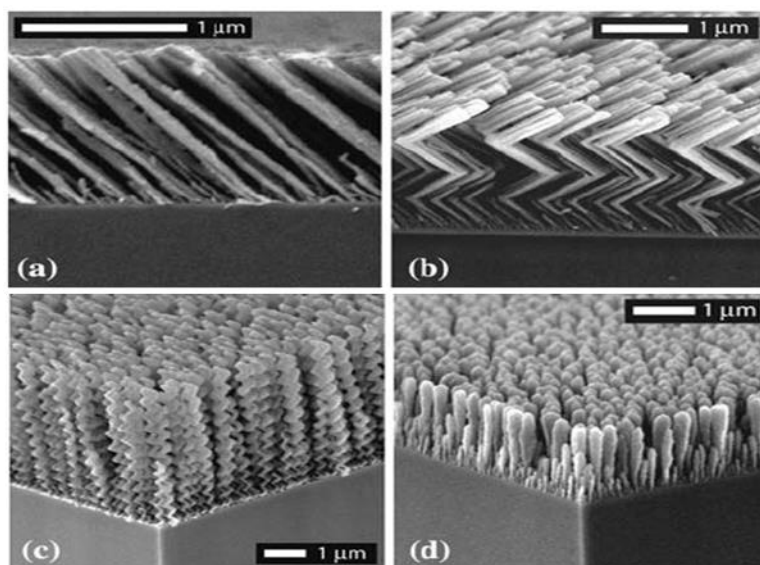
Fig.2.2*: Ejemplos de películas delgadas nanoestructuradas de carácter escultural preparadas mediante GLAD. La película delgada a) muestra una estructura columnar crecida a un ángulo oblicuo y la b) ese mismo tipo de deposición girando la muestra 180° según su eje azimutal a intervalos de tiempo regulares. Las muestras c) y d) se crecieron girando a una velocidad constante. Para una velocidad lenta (c) se obtienen espirales mientras que a velocidades altas (d) se forman columnas perpendiculares.*

Los efectos de sombra que dan lugar al crecimiento de materiales nanoestructurados formados por columnas inclinadas(Ver figura2.1a) respecto al sustrato son una de las causas de que las capas GLAD presenten anisotropía en sus propiedades físico-químicas.

En materiales anisotrópicos sus propiedades son dependientes de la dirección de análisis. En concreto, mientras que los materiales isotrópicos presentan propiedades equivalentes en todas direcciones, las propiedades de los materiales anisotrópicos dependen de la dirección en la que se realiza el análisis de dicha propiedad.

La anisotropía en los materiales puede ser impuesta por una estructura direccionada según sus ejes de crecimiento o por una composición química distinta dentro de una estructura determinada, la cual puede ser direccionada o no. Por

ejemplo, minerales, como la calcita presentan propiedades ópticamente anisotrópicas debido a que su composición química cambia con la dirección de crecimiento. Otros ejemplos de anisotropía estructural que aparecen en la naturaleza pueden ser la estructura celular de la piel, o la estructura de las hojas o la propia madera.[20,21]
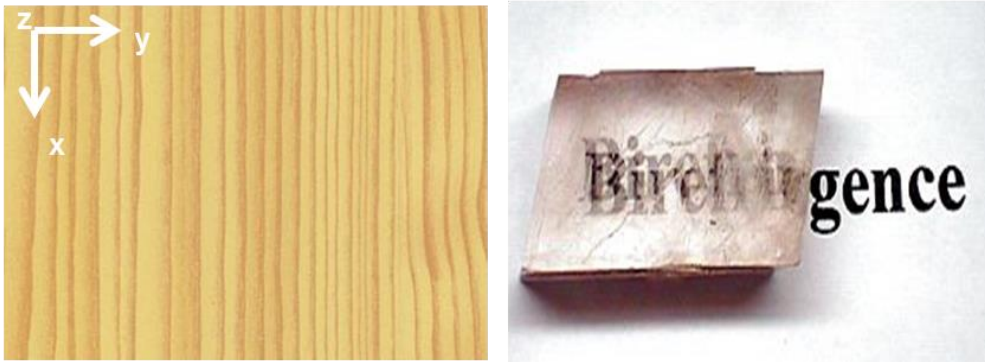
Figura 2.3. Lámina de madera donde se muestra la anisotropía estructural entre los ejes x e y.(izqda.) Pieza de calcita relevando un efecto óptico (Birrefringencia) atribuido a la distinta organización química en ejes perpendiculares a su crecimiento(drcha.).

Como se ha comentado anteriormente, las láminas delgadas mediante GLAD presentan una microestructura singular en forma de nanocolumnas inclinadas. Su porosidad, rugosidad, espesor, conectividad entre columnas etc. son clave para entender las propiedades y propiciar aplicaciones dependientes del tipo de crecimiento.(Véase Capitulo 1). Por ello uno de los objetivos que persigue este trabajo es profundizar en el conocimiento de la anisotropía estructural generada por la agrupación de nanocolumnas GLAD para obtener nuevas propiedades y aplicaciones de estas nanoestructuras.

Diversos trabajos sobre la preparación de láminas delgadas mediante GLAD[12,13,20], han mostrado que las nanocolumnas pueden asociarse lateralmente en forma de agregados en la dirección perpendicular a la llegada de material al sustrato. Este fenómeno es conocido como "bundling", habiéndose estudiado sobre todo en el caso de películas metálicas[12,13,20–22]. Su aplicación a óxidos inorgánicos ha

sido mucho más restringida hasta el momento, desconociéndose sus posibles modificaciones y cómo estas afectan a las propiedades finales de las capas[5,19]

Una de las motivaciones de este trabajo es desarrollar nanoestructuras orientadas de óxidos inorgánicos mediante la técnica GLAD para desarrollar propiedades ópticas y eléctricas anisotrópicas específicas que permitan su aprovechamiento en diversos campos de aplicación como la codificación de información, plasmónica, mojado superficial controlado y microfluídica.

2.2 Modificación de la microestructura GLAD

En las últimas décadas, el uso de plasmas a baja temperatura ha tenido una alta repercusión en ciencia de materiales. La deposición química desde fase vapor asistida por plasma (PECVD) y los procesos de tratamiento superficial empleando plasmas son técnicas bien establecidas en campos como la microelectrónica, optoelectrónica, recubrimientos protectores, tecnología de polímeros, etc. Así mismo, en los últimos años, el plasma está siendo usado como técnica para la modificación de las propiedades de una superficie para ampliar sus rangos de aplicación[23–25]

En esta memoria se muestra por primera vez el efecto de un plasma sobre los crecimientos a ángulo rasante de películas evaporadas (plasma-GLAD) con el objeto de controlar y modificar la microestructura y porosidad de las mismas. Como efecto de esta interacción, se han puesto de manifiesto cambios importantes a nivel nanométrico de la microestructura de las capas y, en consecuencia, de sus propiedades y posibilidades de aplicación.

Para lograr la modificación controlada de nonaestructuras y su modo de agrupación, otra aproximación abordada en el presente trabajo ha sido cuando las capas se depositan sobre sustratos flexibles y son sometidas a esfuerzos mecánicos controlados. Se ha puesto de manifiesto que los cambios que se inducen con las tensiones externas sobre la microestructura de las capas generan otro nuevo campo de propiedades y aplicaciones donde la anisotropía estructural juega un papel

esencial. En concreto, las aplicaciones investigadas en este caso caen dentro de los campos de la óptica y la microfluídica.

2.3 Propiedades y aplicaciones de nanoestructuras orientadas obtenidas mediante GLAD

Las propiedades de los recubrimientos preparados mediante GLAD van a depender en gran medida de la naturaleza química del material y del desarrollo de propiedades anisotrópicas asociadas a su microestructura. Un ejemplo de la bibliografía sobre propiedades eléctricas se refiere a recubrimientos metálicos de cobre o níquel, cuya resistividad varía en función de la dirección de la medida[26,27] Otro ejemplo clásico, es la variación de las propiedades ópticas de capas transparentes en función de la microestructura columnar, tal y como se presenta en la Figura 2.4. En ella se muestra la diferencia entre los valores de índice de refracción para las polarizaciones perpendicular y paralela al eje de anisotropía (Birrefringencia) que poseen una serie de recubrimientos GLAD de distinta naturaleza química.(Ver con más detalle sección 1.3 del Capítulo 1)
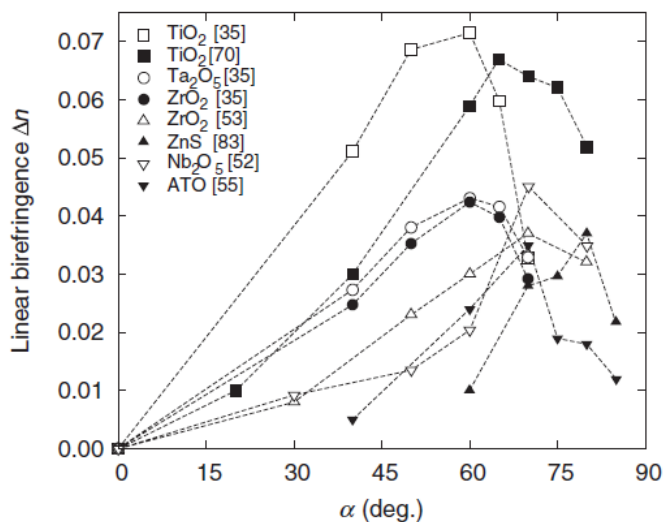
Figura2.4. *Variación de birrefringencia medidas para distintos óxidos inorgánicos mostrando el grado de dependencia de esta propiedad con el ángulo de deposición (α)*[2]

43

En el resumen bibliográfico que acompaña a la introducción de esta tesis se comentan los resultados más relevantes sobre la influencia de la anisotropía estructural sobre las propiedades de estos materiales, principalmente eléctricas, ópticas y de mojado.

2.4 Metodología experimental. Reactor de deposición (GLAD-PVD)

Para la fabricación de capas finas nanoestructuradas la cámara de deposición empleada contiene un evaporador por bombardeo electrónico *"Multihearth electron beam source"*, EV M-5, suministrada por la empresa *Advanced Products &Technologies GmbH* (AP&T). La fuente de electrones es un filamento espiral de wolframio que opera a un determinado potencial fijo y se calienta mediante el efecto Joule por el paso de una corriente eléctrica. El sistema experimental empleado consta de 4 crisoles y un sistema que permite el cambio de uno al otro mediante un motor.

La fuente proporciona una potencia máxima de 4 kW, suministrando una corriente variable al filamento y generando un potencial de aceleración para los electrones. La Figura 2.5 muestra un esquema general del sistema de deposición por evaporación electrónica. La cámara tiene forma cilíndrica, 55 cm de diámetro y 70 cm de altura y está unida a un sistema de vacío.(Ver más Capítulo 1)
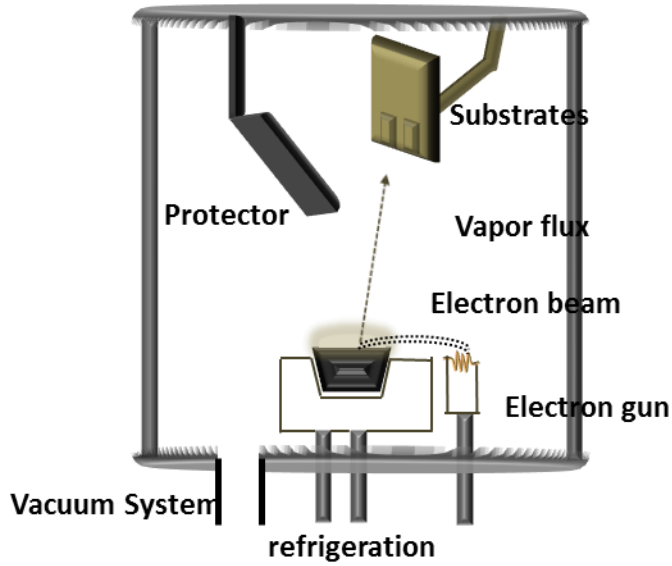
Fig.2.5 . *Esquema general del sistema de deposición por evaporación electrónica.*

El portamuestras se coloca en la parte superior de la cámara, pudiéndose cubrir numerosos sustratos a la vez. El portamuestras está diseñado para poder depositar a varios ángulos de evaporación simultáneamente: 65°, 70°, 80°, 85° y 90°. Una foto y un esquema del portasustratos se muestran en la Figura 2.6
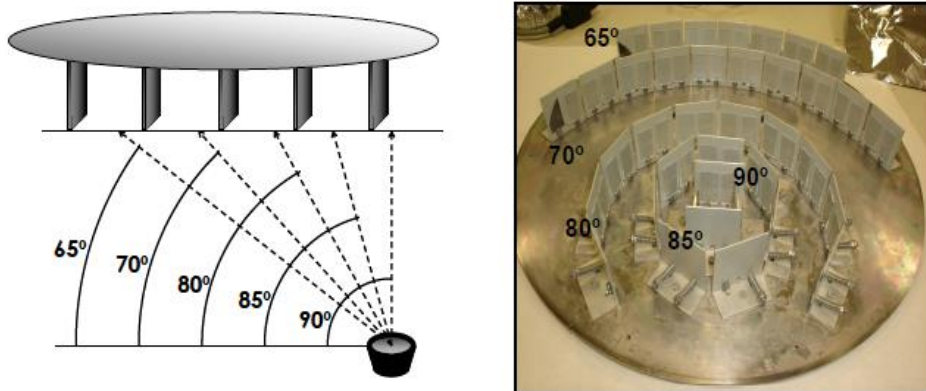
Fig.2.6. *Esquema geométrico (izquierda) y Fotografía (derecha) del portasustratos.*

2.4.1 Plasma GLAD. (PA-GLAD)

Para esta investigación se ha puesto a punto un nuevo sistema experimental que permite asistir la deposición GLAD mediante un plasma. Para ello se ha acoplado un reactor de plasma comercial (Micro-Slam 32) a una cámara de evaporación electrónica. Se trata de una fuente de plasma de microondas a 2.45 GHz con un potencia máxima de 800 W. La fuente puede trabajar en condiciones de "Resonancia Ciclotrónica Electrónica" (ECR), lo que permite obtener plasmas a presiones relativamente bajas (rango 10^{-4} Torr), y densidades electrónicas altas en una región bien confinada[28]. El principal reto de esta modificación a la técnica GLAD es conseguir acoplar un plasma a las condiciones de deposición en ángulo rasante, sin que estas cambien. Para la fabricación de las películas se ha trabajado a una potencia de 460 W. Se ha adaptado un sistema de varios controladores de flujo másico a la cámara de GLAD para poder realizar experimentos con mezclas controladas de gases ($Ar + O_2$).

Para poder emplear este nuevo sistema experimental es necesario sustituir el portamuestras original de la cámara por otro que permita un contacto directo del plasma con los distintos substratos. Por esta razón las distintos experimentos realizados bajo condiciones de plasma se han llevado a cabo a un ángulo de deposición constante de 80º.
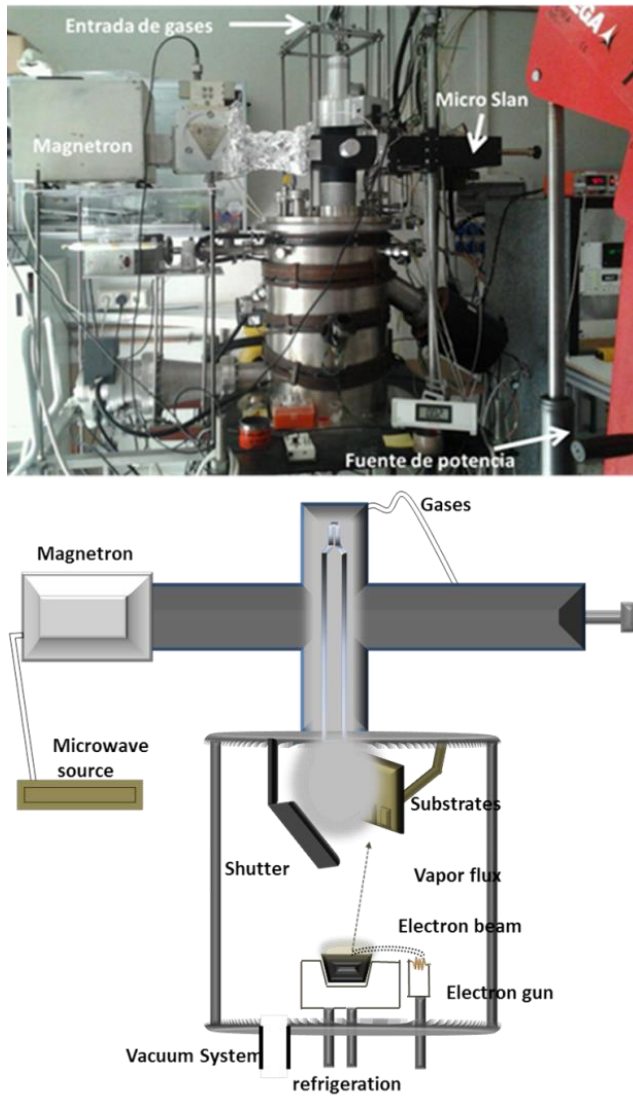
Fig.2.7.(arriba) *Fotografía del sistema experimental Plasma asistido PVD. (abajo) Esquema del sistema experimental.*

2.5 Objetivos

En esta memoria se incluyen los resultados más relevantes de la fabricación de películas delgadas mediante la técnica de evaporación electrónica en ángulo rasante (GLAD), así como en procesos asistidos por plasma y la fabricación de este tipo de láminas sobre sustrato flexible. De forma general, la fabricación de este tipo de películas ha perseguido en este trabajo la consecución de los siguientes objetivos:

1. Controlar y mejorar la anisotropía de la microestructura de las capas GLAD durante su crecimiento.

2. Obtención de películas delgadas crecidas a ángulo rasante sobre sustrato flexible. Análisis de los cambios estructurales en las láminas inducidos tras deformaciones mecánicas

3. Obtención y desarrollo de dispositivos para aplicaciones electro ópticas, ópticas y microfluídicas donde los cambios en la anisotropía estructural es el elemento controlante de las mismas.

2.6   Películas delgadas de ITO con conductividad anisotrópica en el plano fabricadas por deposición a ángulo rasante asistida por plasma.

En este primer trabajo se han preparado películas de Indio dopado con Estaño (ITO) mediante evaporación electrónica a ángulo rasante asistida con plasma.(Sección anterior). El interés de estas capas de ITO reside en la posibilidad de combinar y controlar las propiedades singulares que presenta este material con microestructura porosa, alto porcentaje de transparencia (80-90%) y gran conductividad eléctrica.[27,29,30] Como se verá a continuación, el uso de plasma permite modificar las características finales de las capas y optimizar sus propiedades.

En el desarrollo de este trabajo las capas PA-GLAD (películas crecidas a ángulo rasante asistidas por plasma) se han comparado microestructuralmente y eléctricamente con sus análogas preparadas en ausencia de plasma (GLAD). La microestructura de las películas se ha caracterizado por microscopia electrónica de barrido, microscopia de fuerza atómica y mediante dispersión de Rayos X a ángulo rasante (GISAXS), así como su composición química. Los resultados correspondientes se muestran en el capítulo 3 de esta memoria.

La microestructura que ofrecen los crecimientos en presencia y ausencia de plasma se muestran en la Figura 2.8 donde se observa un claro cambio microestructural al aplicarse plasma durante el crecimiento. La película crecida en ausencia de plasma presenta una distribución homogénea de las nanocolumnas a lo largo de su superficie. Sin embargo, las películas crecidas en presencia de plasma presentan una distribución anisotrópica de las nanoestructuras, siendo aparente un apilamiento o aglomeración de nanocolumnas (*bundling*) en una dirección preferente.
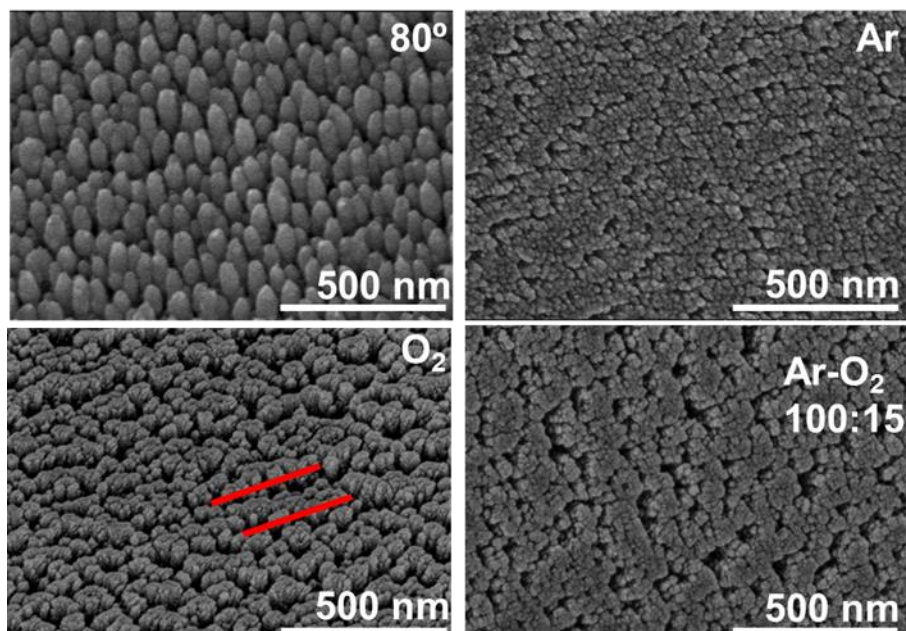
Figura 2.8. *: Micrografías SEM de cuatro películas de ITO depositadas por GLAD crecidas a un ángulo de 80°, tres de ellas crecidas bajo distintas condiciones de plasma, O_2, Ar, y mezclas O_2:Ar a este mismo ángulo de deposición. Todas ellas con un espesor de 500 nm.*

Este cambio en la microestructura no solo se observó en la superficie de las láminas delgadas, sino en el interior de las mismas. Tal y como muestra la Figura 2.9, un examen por SEM de la sección de las capas muestra que el ángulo de inclinación respecto a la normal (Ver capítulo 3) disminuye en presencia de plasma hasta en 15° si se compara con una película crecida en su ausencia. Este cambio microestructural posibilita la fabricación directa de multicapas con distinta geometría con solo encender y apagar el plasma durante la deposición, tal y como demuestra la Figura 2.9
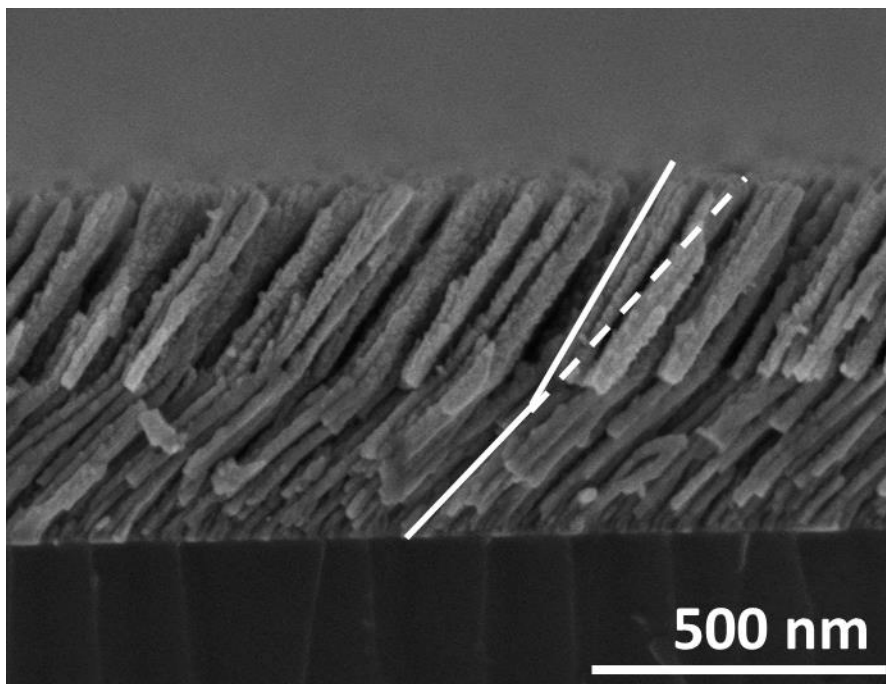
Fig.2.9: *Sección transversal de una bicapa de ITO. (abajo), 250 nm de ITO GLAD; (arriba) 250 nm de ITO PA- GLAD.*

El ITO es uno de los material más usados en la actualidad por su gran conductividad eléctrica y transparencia,[29,31] existiendo el riesgo de que su fabricación en forma de capa porosa pueda llevar consigo pérdidas considerables en conductividad. Para determinar el comportamiento eléctrico de las capas porosas de ITO se midieron curvas de intensidad –voltaje a lo largo del espesor (in depth) y mapas de conducitividad por AFM de las muestras que presentaron mayores cambios microestructurales, es decir la película asistida con plasma de O_2 y su análoga en ausencia de este, tal y como muestra la figura 2.10. Las curvas medidas muestran una respuesta eléctrica muy similar en las dos capas, obteniéndose para la capa GLAD valores de resistencia muy similares a una capa de ITO comercial. Este resultado confirma que a lo largo de la dirección de las columnas el material poroso presenta unas propiedades eléctricas similares a su análogo compacto.
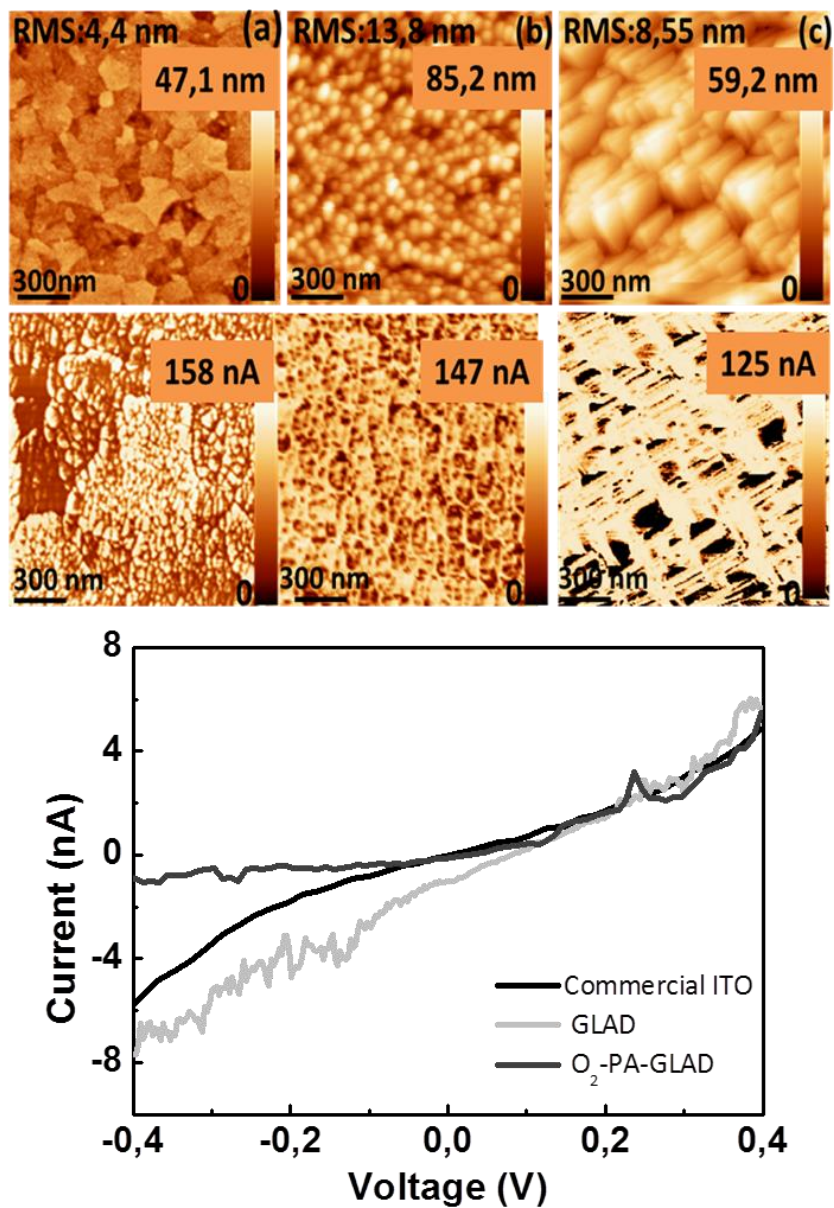
Figura 2.10 Imágenes de topografía (arriba) y mapas de conductividad, (abajo) de ITO comercial, (a) película crecida por GLAD (b) y película GLAD asistida por plasma de O_2(c) La gráfica muestra las Curvas I-V medidas por AFM.

Además, se realizaron medidas macroscópicas de conductividad a lo largo del espesor *(in–depth)* y medidas en superficie *(sheet resistivity)* de las láminas fabricadas[27]. Como resultado de las mismas (**tabla 2.1**) se pudo confirmar que las películas asistidas con plasma presentan dos valores diferentes de resistividad en la superficie según si se mide en dos direcciones perpendiculares, según el apilamiento de columnas *(bundling)* y perpendicular a estos.

Sample	In-depth resistivity $(\Omega*cm)(10^{-2})$	Sheet resistivity (bundling direction) $(\Omega*sq)(10^{-2})$	Sheet resistivity (perpendicular direction) $(\Omega*sq)(10^{-2})$
Commercial ITO plate	6,3	2,1	2,2
80º -GLAD	20,1	48,7	69,7
80º -O_2 Plasma	40,8	84,4	6624
80ºAr Plasma	19,5	55,5	123,1

Finalmente, como aplicación de esta anisotropía estructural y eléctrica de las capas PA-GLAD, se propuso la fabricación de nanocompuestos con respuesta plasmónica y comportamiento dicroico, usando para ello un proceso de electrodeposición de nanoparticulas oro. Los resultados de la figura 2.11 (izqda) muestran que la capa preparada en ausencia de plasma es ópticamente isotrópico debido a que las partículas formadas sobre la superficie de la película crecida son cuasi-esféricas (Véase SEM, Capítulo 3). Sin embargo, la película crecida en presencia de plasma (dcha) presentó un comportamiento dicroico cuando se ilumina con luz linealmente polarizada paralela y perpendicular a la dirección del *bundling*. Esta anisotropía en la forma de las partículas se ha relacionado con un crecimiento constreñido por el apilamiento de columnas. (Véase SEM en capítulo 3)
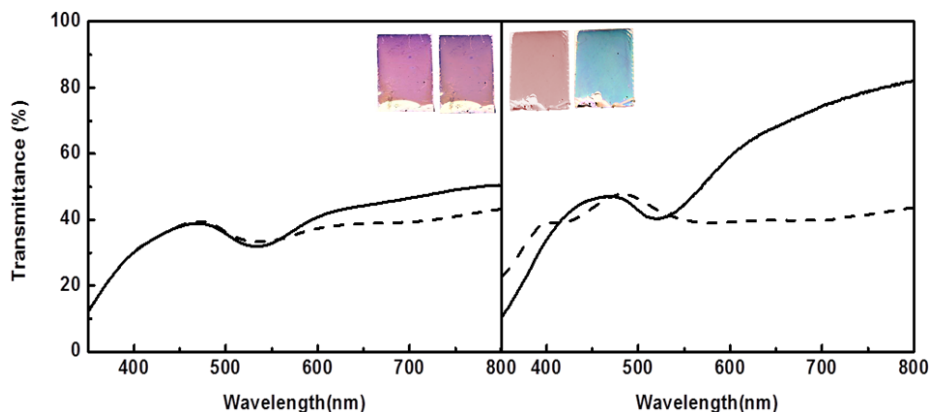
Figure 2.11. *Espectro de transmitancia de UV-vis con luz linearmente polarizada a 0º (línea discontinua) y 90º (línea continua) para nanopartículas de oro depositadas electroquímicamente sobre películas de ITO crecidas en ausencia de plasma (izqda) y películas de ITO asistidas por plasma de O₂ (dcha). Las imágenes muestran claramente las diferentes absorciones mostradas en los espectros de transmitancia..*

2.6.1 Conclusiones

Mediante la asistencia de plasma durante el crecimiento por ángulo rasante se ha conseguido controlar, modificar y mejorar el apilamiento de nanocolumnas y por tanto poder inducir el grado de anisotropía de las capas de ITO preparadas.

Los resultados obtenidos han mostrado que la microestructura de las películas de ITO crecidas por GLAD pueden modificarse por exposición de plasma durante su crecimiento. Se observó una disminución en el ángulo de las columnas así como la agregación de las mismas, hecho que se atribuye a un aumento en el coeficiente de pegado durante el crecimiento *(trapping probability)*(ver más detallado en Capítulo1 y 3).

Ambos tipos de películas presentaron valores similares de conductividad y resistividad a través de su espesor *(in –depth)*. Sin embargo, se determinó que la conductividad eléctrica en el plano en las películas de plasma presenta un carácter

anisotrópico que se asocia a la agregación de nanocolumnas a lo largo de la dirección de apilamiento *(bundling)*.

Gracias a esta nanoestructura orientada estas capas propician la electrodeposición de partículas alargadas de oro, las cuales presentan un comportamiento dicroico bajo acción de luz linealmente polarizada en direcciones perpendiculares.

2.7 Anisotropía óptica de láminas de ITO crecidas por ángulo rasante asistido por plasma para el grabado de información.

En este capítulo se desglosa el comportamiento óptico que presentan las capas de ITO fabricadas y caracterizadas en el capítulo anterior. Concretamente, este capítulo se centra en el estudio óptico de las capas en ausencia de plasma y de películas crecidas en presencia de un plasma de O_2, ambas depositadas a un mismo ángulo de deposición $(\alpha=80^\circ)$.

Se muestra cómo el crecimiento asistido por plasma influye en propiedades ópticas tales como la birrefringencia en el plano obteniéndose valores no descritos anteriormente en la bibliografía. En la parte final de este capítulo se propone una aplicación directa para codificación de información tanto a nivel macroscópico como en la microescala cuando estas capas de alta birrefringencia son expuestas a la luz polarizada o polarizadores cruzados.

Tal y como se mostró en la figura 2.8 del anterior capítulo, el crecimiento de ITO mediante plasma asistido genera el apilamiento de nanocolumnas a lo largo del eje perpendicular a la dirección del crecimiento, *(bundling)*. Este fenómeno se pone de manifiesto de manera más evidente, cuando se obtienen dos secciones transversales a lo largo del eje del *bundling* y perpendicular al *bundling (growing)* en un microscopio de haz iónico focalizado (FIB) observándose que en la película asistida por plasma de oxígeno las distancias intercolumnares son diferentes en ambas direcciones, tal y como muestra la Figura 2.12.
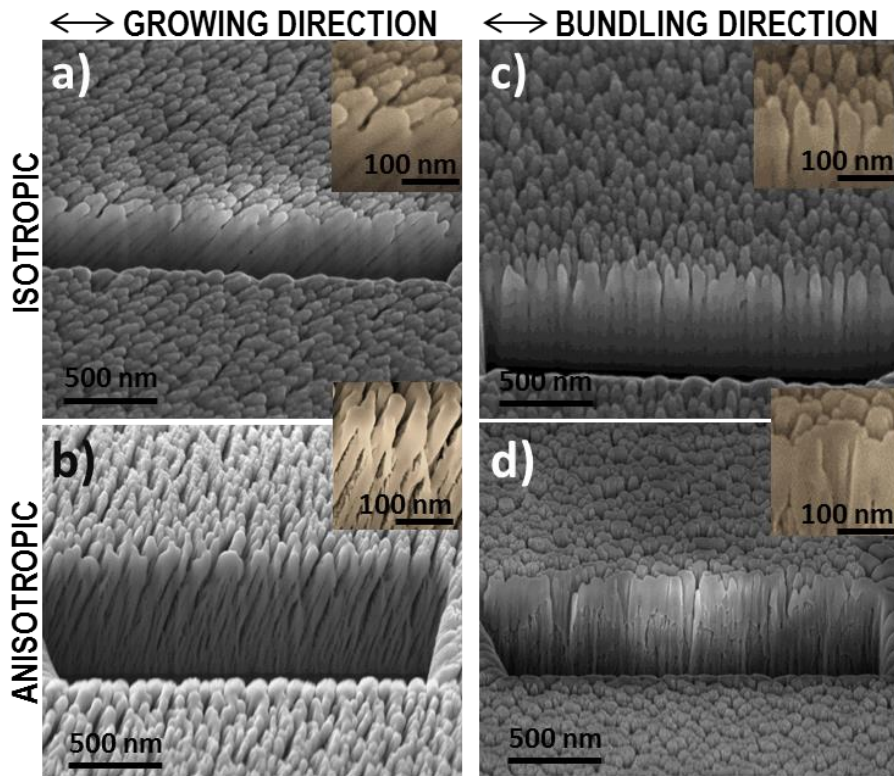
Figure 2.12. *Micrografías FIB en sección transversal de películas de ITO crecidas al mismo ángulo de deposición (80°) en ausencia de plasma (GLAD (a, c)) y en presencia de plasma de O_2(PA-GLAD ITO) (b, d)) Ambas nanoestructuras se analizaron en dos orientaciones perpendiculares(a, b) respecto del bundling(c, d).*

Esta anisotropía estructural produce que el camino óptico recorrido por la luz sea diferente actuando por tanto como una lámina retardadora (Ver más capítulo 4) Esto se traduce en una diferencia de índices de refracción entre los dos ejes perpendiculares entre sí, en este caso entre el eje de asociación de columnas *(bundling)* y el perpendicular a este *(growing)*. A este fenómeno se le denomina birrefringencia en el plano, y los valores de índice de refracción y de porosidad obtenidos para las nanoestructuras analizadas se muestran en la tabla 2.2.

	n (Slow index) bundling direction	n (fast index) Growing direction	Δn	Bundling porosity (%)	Growing porosity (%)
PA-GLAD	1,68	1,48	0,2	41	63
GLAD	1,79	1,79	0	27	27

Se puede observar que para la película PA-GLAD la birrefringencia en el plano es de 0,2, valor que está por encima de los recogidos hasta ahora en bibliografía[2,32] Para ello se ha realizado un exhaustivo estudio del comportamiento de estas láminas cuando se iluminan con luz polarizada y polarizadores cruzados para la rotación azimutal y polar.(Ver esquema capítulo 4).

Los cambios más interesantes se observaron al analizar las películas entre polarizadores cruzados girando en el plano azimutal (plano perpendicular al crecimiento de las columnas) tal y como se observa en la figura 2.13 d.

Para la película PA-GLAD aparece un máximo de transmitancia cuando la muestra se gira 45º respecto de los polarizadores cruzados, coincidiendo con el máximo desalineamiento del eje del *bundling* respecto a los ejes de polarización de los polarizadores cruzados tal y como muestra la figura 2.13 b. Para esta misma rotación la muestra isotrópica (ausencia de plasma) presenta un comportamiento totalmente diferente.(Ver más Capítulo 4)
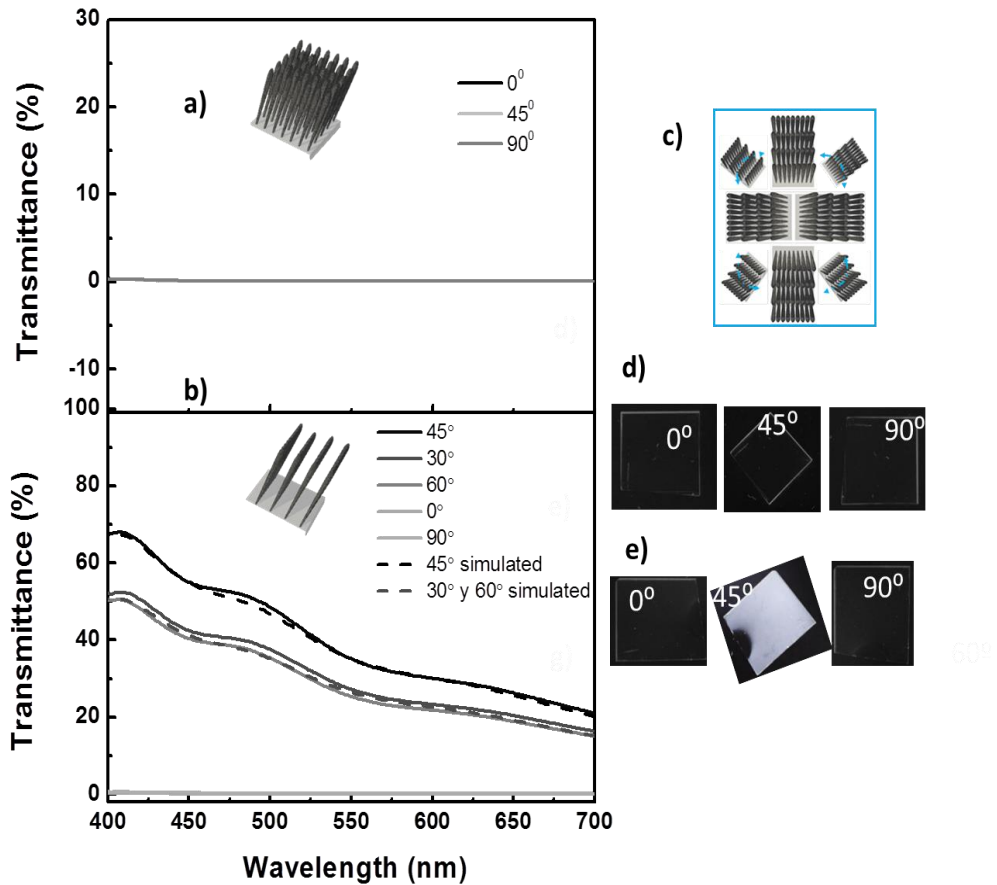
Figure 2.13: Espectros de transmitancia a través de polarizadores cruzados para la películas de ITO en ausencia de plasma (a) y asistida con plasma (b) para una rotación azimutal (c) Equema rotación azimutal. Imágenes de láminas de ITO crecidas en ausencia de plasma (d) y asistida por plasma (e) entre dos polarizadores cruzados para la rotación azimutal.

La combinación de la respuesta óptica de las láminas de ITO crecidas por ángulo rasante cuando se interponen polarizadores cruzados, con la posibilidad de crecer estas capas en distintas zonas de las muestra mediante máscaras permite el desarrollo de dispositivos de encriptación óptica, codificación de información o etiquetado invisible. En este capítulo se muestran varios ejemplos, a nivel macroscópico y microscópico de encriptación óptica empleando estos materiales nanoestructurados y orientados.

Procesos tan sencillos como usar tinta nos permite replicar la huella dactilar humana en una sola etapa de procesado, tal y como se observa en la Figura 2.14. En la misma se muestra cómo alineando el eje óptico (*bundling*) con los polarizadores cruzados la información acuñada (huella) en la superficie no es visible (figura 2.14a), mientras que con un simple giro de 45º (azimutal) se observa con detalle una imagen de la huella dactilar encriptada (figura 2.14 b). (Véase capítulo 4)

El efecto de birrefringencia fue tan evidente, que este tipo de encriptación se pudo llevar a cabo a nivel microscópico. Para ello se realizaron una serie de grabados por fotolitografía, tal y como muestran las figuras 2.14c-f. Las imágenes con un polarizador revelan que la información contenida en los grabados es totalmente invisible (figura2.14 c,e), mientras que con dos polarizadores cruzados se pudieron observar los motivos replicados por fotolitografía en dimensiones del orden de las decenas de micras.
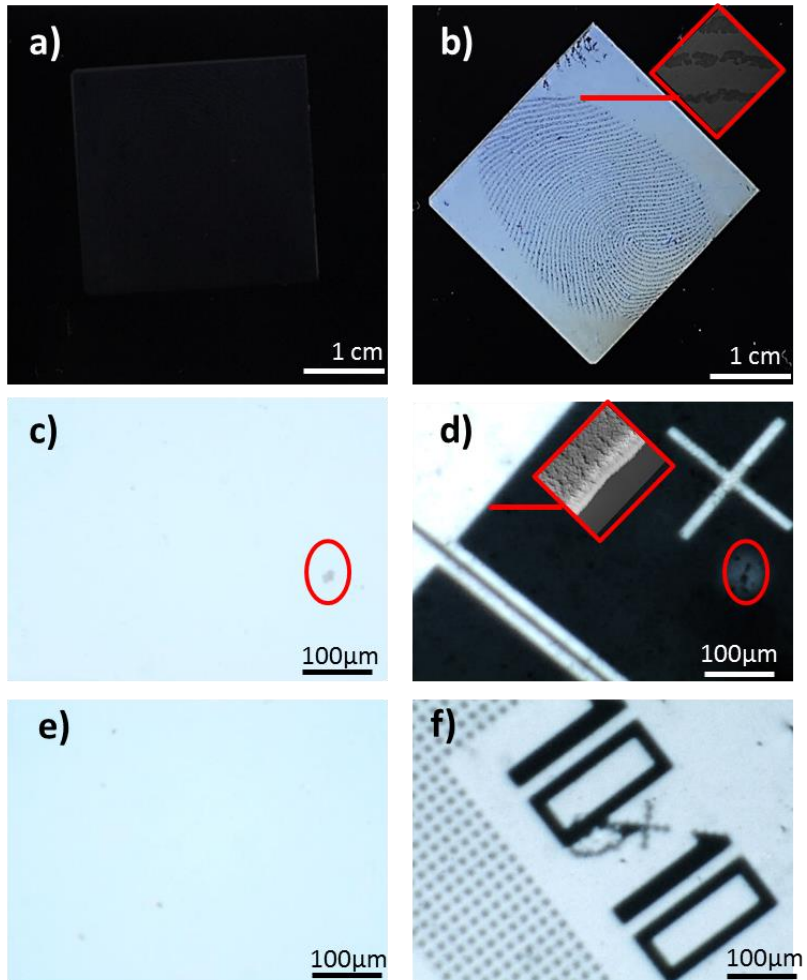
Figure 2.14: *a,b) Imágenes de huella dactilar encriptada en una lámina de ITO crecida mediante PA-GLAD entre polarizadores cruzados. a) eje óptico (bundling) alineado con los polarizadores cruzados. b) eje óptico desalineado respecto a los polarizadores cruzados. c-f) Imágenes de microscopía óptica de grabados por fotolitografía sobre las capas de PA-GLAD, con un polarizador (.c,e) y entre polarizadores cruzados (d,f.). Micrografías SEM de la película de ITO asistida con plasma tras la retirada de la tinta y del fotoresistor.(insets). Imperfección en la muestra, la cual verifica el fenómeno descrito (elipse roja)*

61

2.7.1 Conclusiones

En este trabajo se ha desarrollado una sencilla metodología para crecer películas delgadas de ITO con alta anisotropía estructural y birrefringencia óptica asistiendo mediante plasma durante el crecimiento. Esta anisotropía estructural está compuesta por columnas que presentan diferentes distancias intercolumnares a lo largo del eje de agregamiento *(bundling)* y el perpendicular a este *(growing)*.

Los valores obtenidos de birrefringencia para la película asistida por plasma muestra valores superiores a los registrados en la bibliografía para óxidos obtenidos por GLAD, (Δn=0,2). Estos valores se han extraído, tras la modelización de la respuesta óptica de las muestras a luz polarizada o polarizadores cruzados, obteniendo valores de índice de refracción diferentes y perpendiculares entre sí (1.48 y 1.68 para las direcciones de *growing* and *bundling)*.

El proceso de fabricación es totalmente compatible con el uso de máscaras o técnicas photolitográficas que permiten la fabricación directa de grabados dicroicos. Por tanto, esta metodología abre la puerta a procesos de encriptación donde el grabado solo podría ser legible con polarizadores en las configuraciones adecuadas.

2.8 Rejillas ajustables mediante curvado de sustratos poliméricos

Tanto en el capítulo que se comenta a continuación como en el siguiente, se estudian materiales nanoestructurados GLAD preparados sobre substrato flexible. Este tipo de materiales abre la puerta al desarrollo de propiedades vinculadas con la anisotropía de las capas usando sustratos más interesantes desde el punto de visto económico e industrial.

El objetivo inicial de este trabajo perseguía comprobar que el desarrollo estructural de las capas GLAD era similar cuando crecían sobre polímeros, analizando su adhesión frente a deformación mecánica. Estos objetivos iniciales fueron superados, ya que estos sistemas han permitido desarrollar nuevas funcionalidades ópticas y fluídicas asociadas a la anisotropía estructural inducida en los sistemas preparados cuando estos se someten a deformaciones mecánicas. En esa línea, los resultados de este capítulo permiten el desarrollo de dispositivos con aplicaciones potenciales para el etiquetado invisible, transductores optomecánicos o ventanas inteligentes[7,33–36].

Para este trabajo se han preparado películas GLAD de SiO_2 crecidas sobre polidimetilsiloxano (PDMS). Sobre estos sustratos poliméricos, la distribución de los nanocolumnas antes del proceso de deformación mecánica se ha caracterizado mediante microscopia electrónica de barrido, observándose geometrías similares a las obtenidas sobre sustrato rígido.(Véase Capítulo 5)

Tras su curvatura mecánica, las estructuras híbridas mostraron la formación de rupturas paralelas entre sí y a distancias controladas por la nanoestructura de la película depositada pero independiente del espesor y del ángulo de curvatura, tal y como se muestra en la Figura 2.15 (Ver más capítulo 5) . En este trabajo se ha podido poner de manifiesto que la anisotropía microestructural en el plano que presentan las películas de SiO_2 genera grietas paralelas separadas por un espaciado diferente según el sistema se deforma según ejes perpendiculares entre sí. Concretamente se puede observar que las distancias entre grietas en la dirección del *bundling* (eje x) son menores que en el eje perpendicular a este (*growing*-eje y).

Además, independientemente del tipo de deformación (cóncavo o convexo), las distancias entre grietas se mantienen constantes, siendo esta característica un hecho singular respecto al comportamiento de otros materiales referenciados en la bibliografía donde las distancias y el patrón de grietas dependen del tipo de doblado[37,38]
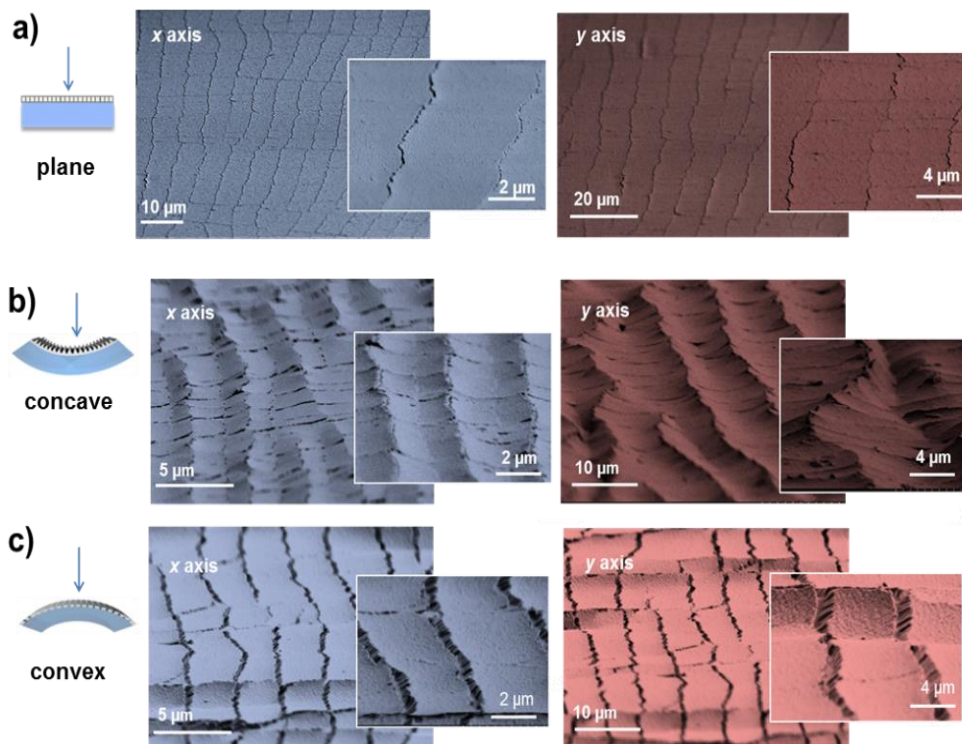
Figure 2.15. *a) Micrografías FESEM de dos láminas G-SiO₂/PDMS en posición plana después de doblarlo a lo largo del eje x (izq) y del eje y (dcha).b) Micrografías FESEM de las películas G-SiO₂/PDMS en posición cóncava durante su observación. c) Micrografías FESEM de las películas G-SiO₂/PDMS en posición convexa durante su observación. Todos los ejemplos corresponden a una película de 300 nm de espesor crecida a un ángulo de deposición 85°.*

Una propiedad destacable del sistema de grietas paralelas generado tras el proceso de deformación mecánica, es que estos nanocompuestos (G-SiO$_2$/PDMS) actúan como una rejilla óptica reversible.

La Figura 2.16a muestra que el sustrato de PDMS recubierto por la capa delgada de SiO$_2$ es transparente cuando se deforma en configuración convexa y cuando no se somete a ningún esfuerzo mecánico. (Ver esquema figura 2.16). Sin embargo, si este sistema compuesto se adapta a una geometría cóncava, su comportamiento óptico responde al de una rejilla de difracción, descomponiendo el haz de luz blanca en sus componentes.

Para confirmar este comportamiento óptico, estas láminas compuestas G-SiO$_2$/PDMS dieron lugar a patrones de difracción cuando se iluminaron con un láser (532 nm). Este comportamiento se produjo en dos direcciones de doblado (x e y según el esquema), siendo posible simular los patrones según un modelo de difracción tipo Fraunhofer, tal y como se observa en la figura 2.16b. En ese caso, el modelo asume una ondulación periódica, según se observa cuando la superficie de la lámina compuesta estaba deformada en posición cóncava (ver más detalles en capitulo 5).
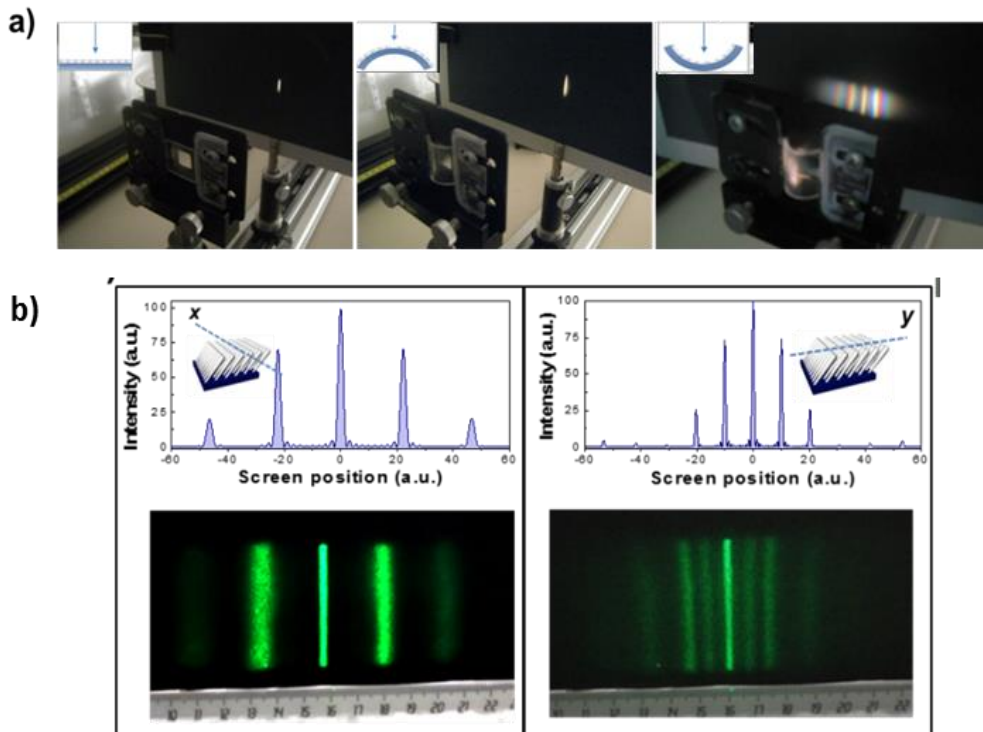
Figure 2.16. a) *Imágenes de un haz de luz blanca pasando a través de una lámina G-SiO$_2$-PDMS con grietas regulares inducidas por doblado. Cuando la luz blanca pasa a través de la lámina compuesta en configuración plana (izqda) y convexa (centro) no se observan cambios en la pantalla. Cuando la luz blanca pasa a través de la lámina en configuración cóncava (dcha) se produce un patrón de difracción sobre la pantalla. b) Patrones de difracción obtenidos por iluminación con un láser (532 nm) sobre el nanocompuesto de G-SiO$_2$/PDMS al ser curvado en los ejes" x" e" y" de doblado. Patrones de difracción Fraunhofer calculados para estos dos ejes de doblado.*

Una aplicación directa y sencilla del efecto óptico de difusión local que se observa cuando estos nanocompuestos se manipulan manualmente es el desarrollo de etiquetas invisibles (ver más en capítulo 5). La técnica GLAD permite el crecimiento nanocolumnar en distintas regiones a lo largo del sustrato mediante la deposición con máscaras. Un ejemplo de ello se muestra en la Figura 2.17 donde se ha depositado una capa delgada de SiO_2 sobre cada lámina de PDMS a ángulo rasante usando máscaras diferentes en ambas caras de la lámina de PDMS.
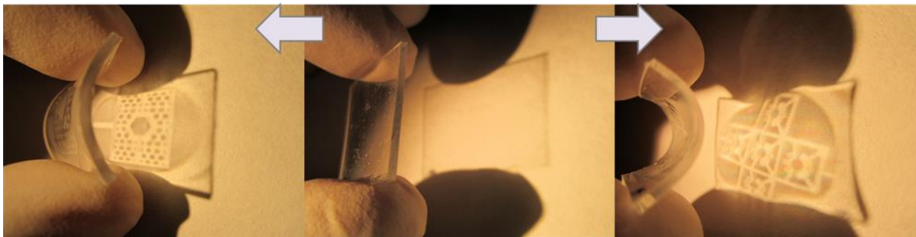
Figura 2.17. *Imágenes de la lámina de G-SiO_2/PDMS depositada en ambas caras con diferentes máscaras. La luz proyectada muestra el grabado impreso sobre la superficie cóncava mientras que el grabado en la superficie opuesta- convexa es invisible*

2.8.1 Conclusiones

Los resultados obtenidos han demostrado la fabricación de rejillas reversibles/conmutables por deformación mecánica de láminas de PDMS con películas de SiO_2 crecidas sobre su superficie. La simplicidad del proceso prueba que el proceso de fabricación puede realizarse en un solo paso, aplicando tensiones sin ninguna precaución especial o consideración sobre el ángulo de curvatura.

La deformación mecánica inducida por la primera manipulación da a lugar a la formación de estructuras periódicas de grietas micrométricas paralelas entre sí. Una vez formado el patrón de grietas, la estructura puede acomodarse a la deformación en los siguientes procesos de deformación sin incremento de las distancias entre grietas. Estas estructuras regulares son los elementos responsables de la respuesta óptica cuando la lámina se dispone en configuración cóncava. Estas

estructuras regulares vienen determinadas por la nanoestructura de la película y no por el proceso de deformación. Este hecho se confirma tras observar las distintas distancias que aparecen entre estructuras regulares cuando las láminas se doblan según dos direcciones anisotrópicas en el plano (*"bundling-eje x"* y *"growing-eje y"*).Se considera que estos resultados pueden usarse como punto de partida para el diseño de nuevas estrategias en campos tan diversos como el de los micro/nano grabados en fotónica, actuadores optomecánicos, etiquetado invisible y codificación de información

2.9 Mojado anisotrópico de capas de TiO$_2$ sobre sustratos PDMS controlado mediante actuación mecánica.

Como ya se ha explicado en el capítulo anterior el crecimiento de láminas nanoestructuradas crecidas por GLAD sobre polidimetilsiloxano (PDMS) genera estructuras regulares auto-organizadas cuando se someten a deformaciones mecánicas.

En el capítulo presente se muestra cómo se puede usar este tipo de estructuras regulares para el control y transporte selectivo de líquidos. Para ello, y a diferencia que el anterior capítulo, las capas nanoestrucutradas son de TiO$_2$, el cual, ha sido ampliamente reportado en numerosos trabajos de mojado y microfluídica[39–42].En este trabajo se persigue el control anisotrópico de mojado, aprovechando la generación de un sistema de estructuras regulares autoorganizadas de distintas dimensiones cuando estos nanocompuestos se manipulan manualmente en distintas direcciones.El deslizamiento y control de gotas de líquidos sobre la superficie nanoestructurada de TiO$_2$ crecido a ángulo rasante sobre PDMS de (G-TiO$_2$/PDMS) bajo manipulación manual es posible sin presencia de un comportamiento superhidrofóbico debido a la inducción de una rugosidad a doble escala a través de la aparición de estructuras regulares en la microescala que permite el control de líquidos.[7,43,44]

Este resultado posibilita el desarrollo de un dispositivo sencillo y flexible para el control de movimientos de gotas mediante manipulación manual. La importancia de este trabajo reside en la fabricación de dispositivos anisotrópicos para el control direccional del movimiento de líquidos, el cual es un campo emergente en la investigación y en el desarrollo industrial de la eficiencia energética dentro del área de las superficies auto-limpiables y la fabricación de válvulas y filtros microfluídicos[45].

La generación de estructuras regulares paralelas entre sí cuando el nanocompuesto GTiO$_2$/PDMS se curva en la dirección del *bundling* (c,d) y en la dirección perpendicular, *growing* (f,g) a este se muestra en la figura 2.18. Nuevamente las grietas generadas en este nanocompuesto presentan las mismas

69

tendencias observadas en el capítulo anterior, es decir las distancias entre grietas en la dirección del *bundling* son menores que en la perpendicular a este. Además tras el proceso de deformación las distancias entre grietas se mantienen tal y como se puede observar en la figura 2.19 a,b.

En este trabajo, se analizó el comportamiento microestructural de las láminas cuando estas se estiran con el objetivo de entender el comportamiento de los líquidos bajo estas condiciones de deformación, observándose un aumento de las distancias entre grietas en la dirección del estiramiento, tal y como muestra la figura 2.19 e,h
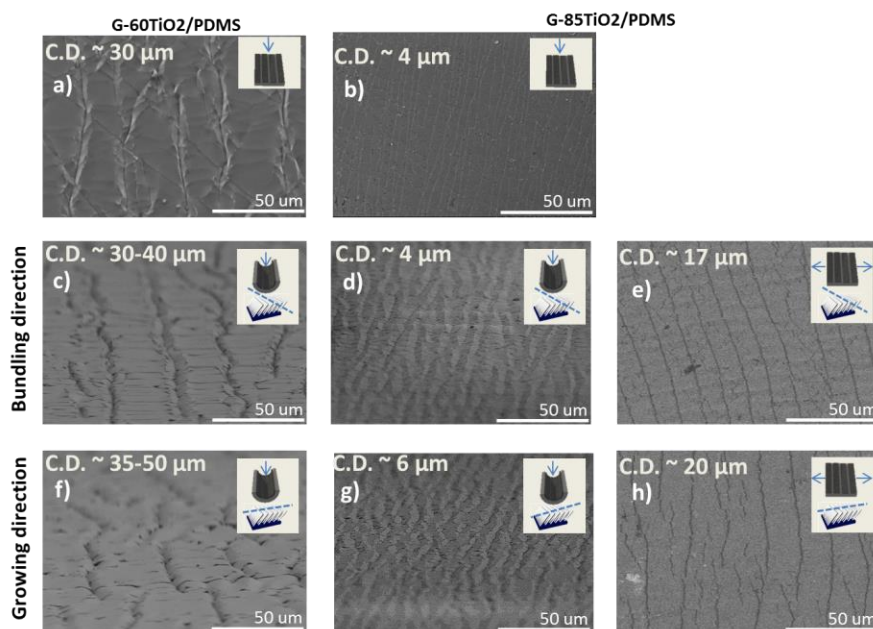
Figura 2.19. *a y b) Micrografías FESEM de dos láminas 60° y 85°G-TiO2/PDMS en configuración plana después del proceso de doblado.c-e) Micrografías FESEM de la superficie de las láminas 60°(izqda) y 85°(centro y dcha) G-TiO2/PDMS en posición cóncava a lo largo del eje de "bundling"). f-h) Micrografías FESEM de las películas 60°(izqda) y 85°(centro y dcha) G-TiO2/PDMS en posición cóncava a lo largo del eje perpendicular al "bundling". Micrografías FESEM de las películas 85°G-TiO2/PDMS en posición plana-estirada a lo largo del eje del "bundling" (e) y del eje perpendicular al "bundling" (h).*

Una vez comprobado el tipo de estructuras anisotrópicas generadas en el nanocomposite G-TiO$_2$/PDMS tras su deformación y teniendo en cuenta los resultados de anisotropía óptica obtenidos en el capítulo anterior, se desarrolló un estudio amplio sobre el deslizamiento de gotas de líquidos de distinta naturaleza polar (agua y diiodometano), con el fin de estudiar su comportamiento frente a distintas configuraciones de deformación mecánica.

A su vez, estos resultados se compararon con los obtenidos por una lámina de PDMS tal y como muestra la figura 2.20. En este caso, las gotas depositadas sobre la lámina de PDMS presentaron un deslizamiento equivalente tanto para la dirección normal como la paralela a la tensión/deformación aplicada. En comparación, el comportamiento de los líquidos sobre la superficie con la capa nanoestructurada se vieron muy afectados según el ángulo de deslizamiento, especialmente en el caso de gotas de diiodometano, presentando un comportamiento de deslizamiento anisotrópico. Este comportamiento singular se atribuye a la diferente micro y nano estructura de la superficie según el eje sobre el que se aplique la tensión y se produzca la deformación correspondiente, así como al efecto de su comportamiento diferente en las configuraciones cóncava, convexa o estirada. (Estudio detallado en el capítulo 6)
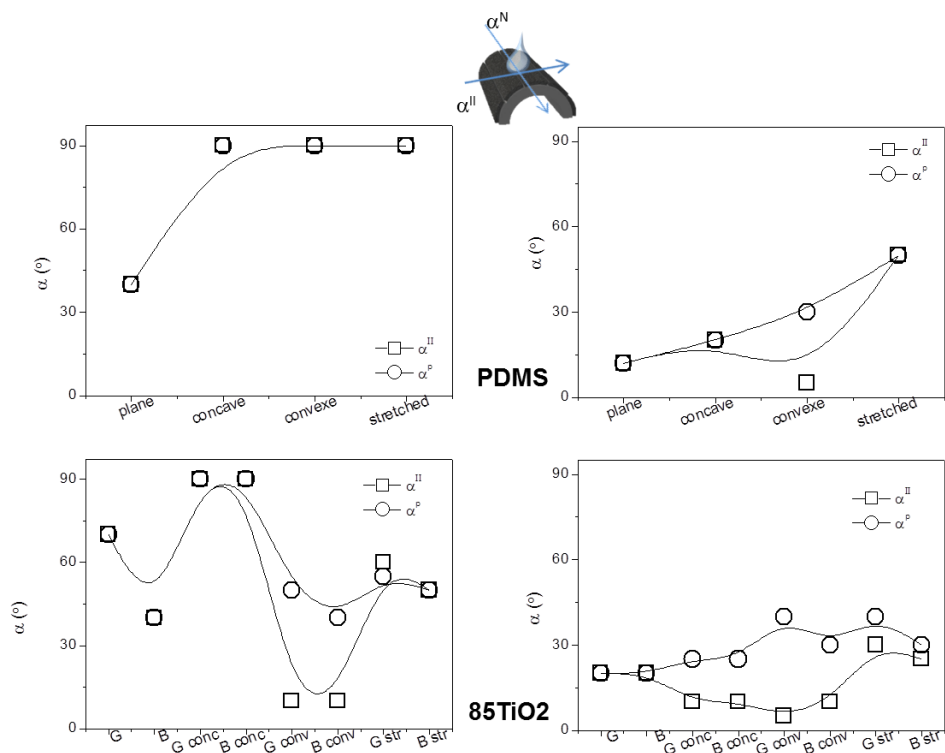
Figura 2.20. *Estudio de deslizamiento de una gota de agua (izqda) y diiodometano (dcha) sobre una lámina de PDMS (arriba) y 85ºG-TiO2/PDMS (abajo).*

Una apreciación visual de los efectos anteriores resulta también muy ilustrativa de la existencia de fenómenos de mojado anisotrópico sobre las superficies deformadas. Así, sobre una superficie inclinada no deformada de PDMS, una gota de agua se mantiene anclada incluso para inclinaciones muy considerables y sólo se desprende de la superficie cuando se coloca en posición vertical y los efectos gravitatorios exceden a las tensiones superficiales. Sin embargo, para una posición vertical, el movimiento o deslizamiento de una gota de agua resulta restringido sobre la superficie de la lámina $G60ºTiO_2/PDMS$ cuando se curva en posición convexa con el eje de doblado ajustado a la dirección del *growing*. Por el contrario, cuando la lámina se deforma en la dirección del *bundling*, la gota de agua abandona la superficie. Los distintos comportamientos se pueden

observar en la conjunto de imágenes que muestra la figura 2.21. La explicación de los mismos hay que buscarlos en la distinta nanoestructuración superficial inducida por el doblado y la exposición de la gota de agua a zonas de PDMS de las grietas en el caso de que el doblado deje zonas del sustrato expuestas. (Ver más Capítulo 6.)
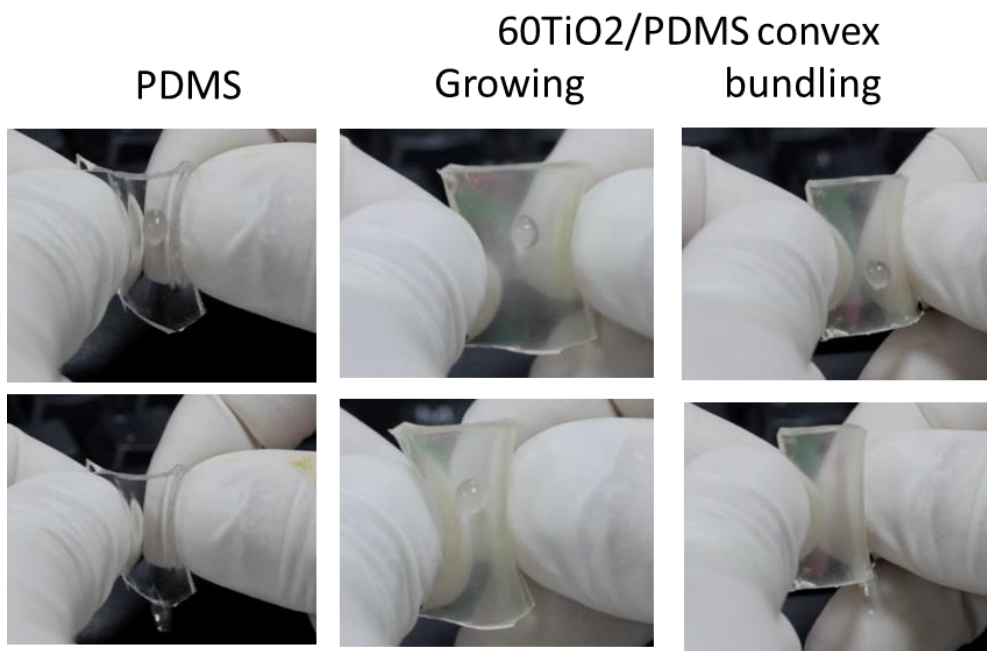
Figura2.21 Deslizamiento selectivo de agua por deformación mecánica de la superficie de G-60ºTiO$_2$/PDMS en función del dirección de deformación. La gota de agua se ancla sobre la superficie de G-60ºTiO$_2$/PDMS cuando se curva en la dirección perpendicular al bundling(growing) mientras que se desprende cuando la lámina se dobla según la dirección del bundling

2.9.1 Conclusiones

Se ha demostrado que mediante la manipulación manual de sustratos de PDMS recubiertos de nanocolumnas inclinadas de TiO_2, el control y transporte selectivo/guiado de gotas de líquidos es posible sin la necesidad de generar superficies superhidrofóbicas debido a la inducción de una doble rugosidad. La rugosidad generada se debe a la distribución nanocolumnar que ofrece este tipo de crecimiento más el patrón de grietas y arrugas (*wrinkling*) que se generan al deformar la lámina del sustrato flexible con la capa nanoestructurada sobre su superficie.

La retención/deslizamiento controlados de gotas de agua es posible deformando las láminas G-TiO_2/PDMS en posición cóncava y convexa. Mientras, estirando las láminas de G-TiO_2/PDMS, se exhibe un comportamiento omnifóbico haciendo posible el control de líquidos no polares sobre la superficie. Además, se han encontrado dos niveles de anisotropía de mojado: 1) el mojado según la dirección del *bundling* (eje x) de la estructura de TiO_2 es mayor que en la dirección perpendicular a este, 2) el deslizamiento sobre la dirección paralela a la tensión aplicada externamente es mejor que sobre la normal a este, especialmente para líquidos no polares.

En conclusión, las láminas de TiO_2/PDMS han resultado materiales eficaces para el control dinámico del mojado de líquidos con grandes perspectivas de uso para el desarrollo de dispositivos microfluídicos selectivos o filtros de separación agua/aceite bajo manipulación manual o mecánica.

REFERENCES

(1)   Ohring, M. In *Materials Science of Thin Films (Second Edition)*; Ohring, M., Ed.; Academic Press: San Diego, 2002; pp 1–56.

(2)   Hawkeye, M. M.; Taschuk, M. T.; Brett, M. J. *Glancing angle deposition of thin films: engineering the nanoscale*; 2014.

(3)   Murray, W. A.; Barnes, W. L. *Adv. Mater.* **2007**, *19* (22), 3771–3782.

(4)   Beaudry, A. L.; LaForge, J. M.; Tucker, R. T.; Li, P.; Taschuk, M. T.; Brett, M. J. *Cryst. Growth Des.* **2013**, *13* (1), 212–219.

(5)   Sanchez-Valencia, J. R.; Toudert, J.; Borras, A.; Barranco, A.; Lahoz, R.; de la Fuente, G. F.; Frutos, F.; Gonzalez-Elipe, A. R. *Adv. Mater.* **2011**, *23* (7), 848–853.

(6)   Oliva-Ramirez, M.; González-García, L.; Parra-Barranco, J.; Yubero, F.; Barranco, A.; González-Elipe, A. R. *ACS Appl. Mater. Interfaces* **2013**, *5* (14), 6743–6750.

(7)   Malvadkar, N. A.; Hancock, M. J.; Sekeroglu, K.; Dressick, W. J.; Demirel, M. C. *Nat. Mater.* **2010**, *9* (12), 1023–1028.

(8)   Liu, Y.-J.; Zhang, Z.-Y.; Dluhy, R. A.; Zhao, Y.-P. *J. Raman Spectrosc.* **2010**, *41* (10), 1112–1118.

(9)   González-García, L.; Parra-Barranco, J.; Sánchez-Valencia, J. R.; Barranco, A.; Borrás, A.; González-Elipe, A. R.; García-Gutiérrez, M.-C.; Hernández, J. J.; Rueda, D. R.; Ezquerra, T. A. *Nanotechnology* **2012**, *23* (20).

(10)   Lintymer, J.; Martin, N.; Chappé, J.-M.; Delobelle, P.; Takadoum, J. *Surf. Coat. Technol.* **2004**, *180-181*, 26–32.

(11)   Yamada, A.; Takakura, W.; Ikeda, S.; Ueda, Y. *Phys. Status Solidi Appl. Res.* **2002**, *189* (3), 753–757.

(12)   Abelmann, L.; Lodder, C. *Thin Solid Films* **1997**, *305* (1–2), 1–21.

(13)   Van Kranenburg, H.; Lodder, C. *Mater. Sci. Eng. R Rep.* **1994**, *11* (7), 295–354.

(14)   Robbie, K.; Brett, M. J. *J. Vac. Sci. Technol. Vac. Surf. Films* **1997**, *15* (3), 1460–1465.

(15)   Marcu, A.; Viespe, C. *Sens. Actuators B Chem.* **2015**, *208*, 1–6.

(16)   Albrecht, O.; Zierold, R.; Patzig, C.; Bachmann, J.; Sturm, C.; Rheinländer, B.; Grundmann, M.; Görlitz, D.; Rauschenbach, B.; Nielsch, K. *Phys. Status Solidi B* **2010**, *247* (6), 1365–1371.

(17)   Hrudey, P. C. P.; Westra, K. L.; Brett, M. J. *Adv. Mater.* **2006**, *18* (2), 224–228.

(18)   Chung, J. Y.; Youngblood, J. P.; Stafford, C. M. *Soft Matter* **2007**, *3* (9).

(19)   Gonzalez-García, L.; Parra-Barranco, J.; Sanchez-Valencia, J. R.; Ferrer, J.; Garcia-Gutierrez, M.-C.; Barranco, A.; Gonzalez-Elipe, A. R. *Adv. Funct. Mater.* **2013**, *23* (13), 1655–1663.

(20)   Hara, K.; Kamiya, M.; Hashimoto, T.; Okamoto, K.; Fujiwara, H. *Thin Solid Films* **1988**, *158* (2), 239–244.

(21)   Itoh, K.; Ichikawa, F.; Takahashi, Y.; Tsutsumi, K.; Noguchi, Y.; Okamoto, K.; Uchiyama, T.; Iguchi, I. *Jpn. J. Appl. Phys.* **2006**, *45* (4R).

(22) Nicolas Filippin, A.; Borras, A.; Rico, V. J.; Frutos, F.; González-Elipe, A. R. *Nanotechnology* **2013**, *24* (4), 045301.

(23) Van Dijken, J. G.; Brett, M. J. *J. Vac. Sci. Technol. Vac. Surf. Films* **2012**, *30* (4).

(24) Xue, C.-H.; Jia, S.-T.; Zhang, J.; Ma, J.-Z. *Sci. Technol. Adv. Mater.* **2010**, *11* (3).

(25) Flickyngerová, S.; Netrvalová, M.; Šutta, P.; Novotný, I.; Tvarožek, V.; Gašpierik, P.; Bruncko, J. *Thin Solid Films* **2011**, *520* (4), 1233–1237.

(26) Lintymer, J.; Gavoille, J.; Martin, N.; Takadoum, J. *Surf. Coat. Technol.* **2003**, *174*, 316–323.

(27) Vick, D.; Brett, M. J. *J. Vac. Sci. Technol. Vac. Surf. Films* **2006**, *24* (1), 156–164.

(28) Anner, G. E. In *Planar Processing Primer*; Springer Netherlands, 1990; pp 359–399.

(29) Granqvist, C. G.; Hultåker, A. *Thin Solid Films* **2002**, *411* (1), 1–5.

(30) Soref, R. A.; Rafuse, M. J. *J. Appl. Phys.* **1972**, *43* (5), 2029–2037.

(31) Leem, J. W.; Yu, J. S. *Opt. Express* **2011**, *19 Suppl 3*, A258–A268.

(32) Hodgkinson, I.; Wu, Q. hong. *Appl. Opt.* **1999**, *38* (16), 3621–3625.

(33) Calvo, M. E.; González-García, L.; Parra-Barranco, J.; Barranco, A.; Jiménez-Solano, A.; González-Elipe, A. R.; Míguez, H. *Adv. Opt. Mater.* **2015**, *3* (2), 272–272.

(34) Nagai, H.; Irie, T.; Takahashi, J.; Wakida, S. *Biosens. Bioelectron.* **2007**, *22* (9–10), 1968–1973.

(35) Yin, H.-E.; Huang, F.-H.; Chiu, W.-Y. *J. Mater. Chem.* **2012**, *22* (28).

(36) Maruyama, T.; Hirakata, H.; Yonezu, A.; Minoshima, K. *Appl. Phys. Lett.* **2011**, *98* (4).

(37) Kim, P.; Hu, Y.; Alvarenga, J.; Kolle, M.; Suo, Z.; Aizenberg, J. *Adv. Opt. Mater.* **2013**, *1* (5), 381–388.

(38) Chung, J. Y.; Nolte, A. J.; Stafford, C. M. *Adv. Mater.* **2011**, *23* (3), 349–368.

(39) Guldin, S.; Kohn, P.; Stefik, M.; Song, J.; Divitini, G.; Ecarla, F.; Ducati, C.; Wiesner, U.; Steiner, U. *Nano Lett.* **2013**, *13* (11), 5329–5335.

(40) Wang, J.-H.; Shih, T.-K.; Chen, C.-F.; Chen, K.-C.; Chen, C.-C.; Whang, W.-T.; Huang, G. S.; Su, H.-Y. *Opt. Commun.* **2008**, *281* (15-16), 3953–3956.

(41) Deng, Z.-Y.; Wang, W.; Mao, L.-H.; Wang, C.-F.; Chen, S. *J. Mater. Chem. A* **2014**, *2* (12).

(42) Nakata, K.; Udagawa, K.; Ochiai, T.; Sakai, H.; Murakami, T.; Abe, M.; Fujishima, A. *Mater. Chem. Phys.* **2011**, *126* (3), 484–487.

(43) Kang, S. M.; Lee, C.; Kim, H. N.; Lee, B. J.; Lee, J. E.; Kwak, M. K.; Suh, K.-Y. *Adv. Mater.* **2013**, *25* (40), 5756–5761.

(44) Wu, D.; Wang, J.-N.; Wu, S.-Z.; Chen, Q.-D.; Zhao, S.; Zhang, H.; Sun, H.-B.; Jiang, L. *Adv. Funct. Mater.* **2011**, *21* (15), 2927–2932.

(45) Rahmawan, Y.; Xu, L.; Yang, S. *J. Mater. Chem. A* **2013**, *1* (9).

+

Chapter 3

Anisotropic In-plane Conductivity and Dichroic Gold Plasmon Resonance in Plasma Assisted ITO Thin Films e-Beam Evaporated at Oblique Angles

3.1 Introduction

Such as was commented in Chapter 1, Indium tin oxide (ITO) presents excellent conductivity, high optical transmission and the relatively easy up-scaling of manufacturing processes, being a key transparent electronic material.[1] Only its cost and the relative scarcity of indium have prompted the search for other alternative transparent and conductive (TCO) films.[2]

ITO thin films have been prepared by a large variety of procedures including wet (i.e., sol-gel, spray, dip-coating, etc.[3,4]) or dry, (i.e., vacuum and plasma) methods of deposition, these latter including e-beam evaporation or magnetron sputtering.[5–8] Recently, porous nanostructured ITO thin films and related stacked nanostructures have been prepared by deposition at glancing angles (GLAD thin films)(Chapter 1).[9–13]

By this manufacturing process, the substrates form an oblique angle with respect to the flux direction of the deposition material usually generated by e-beam or magnetron sputtering.[14–16] Metals,[17,18] oxides,[19–22] semiconductors[23,24] and molecular materials[25] have been prepared in the form of thin films by using this methodology.

Their microstructure consists of tilted nanocolumns which, extending from the interface with the substrate up to the surface, confer the films outstanding optical, adsorption or magnetic properties.[26–32]GLAD-ITO nanostructured layers have been also stacked in the form of 1D photonic crystals[33,34] that depict singular Bragg reflection and conductivity performances.[35,36] On the other hand, branched ITO nanostructures have been also prepared by GLAD evaporation under conditions inducing a vacuum liquid-solid (VLS) growth.[37–41] In these systems the electrical conductivity is expected to be higher along the direction of the specific elements in their nanostructure.

In the present Chapter, has been developed an experimental strategy consisting of plasma assisting the growth of e-beam GLAD ITO thin films, which is explained in the next section.

In literature, GLAD thin films have been grown under the effect of a beam of accelerated ions.[42]Once formed, compact ITO thin films have been also subjected to plasma etching to induce the growth of nanopillar structures.[12] However, to our knowledge, there are no previous essays where a plasma is used to assist the growth of e-beam GLAD thin films during deposition.

Besides describing the experimental procedure,in this work is presented a characterization of the GLAD-ITO films prepared both by direct e-beam evaporation or by assisting the deposition with Ar or O_2 plasmas supplied with a low pressure plasma source.

Scanning electron microscopy (SEM), topographic atomic force and electrical scanning microscopy (AFM), gracing incidence small angle X-ray scattering (GISAXS), besides sheet and in-depth conductivity measurements have been utilized for the characterization analysis of the samples. It will be shown that, besides changes in the nanocolumns orientation, an outstanding effect of plasma assisting the film growth is the bundling association of the individual nanocolumns[14,43] that define a preferential direction rendering anisotropic in-plane conductivity[44]. A preliminary discussion about this anisotropic bundling association of nanocolumns under the action of a plasma has been carried out within the frame of the trapping mechanism concept[45,46]recently proposed by us to account for the tilting angle of nanocolumns beyond the heuristic tangent and cosine rules.[47]

To illustrate the possibilities of application of this type of anisotropy in microstructure and electrical properties, is proposed the preparation of dichroic thin films formed by the electrochemical deposition of gold nanostructures on the anisotropic ITO films.

In Chapter 1 has been shown that anisotropic gold or silver nanostructures presenting a dichroic plasmon resonance behavior can be prepared by different chemical or physical methods making use of a template effect of the bundles developed in GLAD SiO_2 thin films.[48,49]

In the present chapter, contrary to the electrochemical deposition of isotropic and spherical gold nanoparticles found on conventional ITO films,[50,51]a

surface template effect of the plasma assisted GLAD-ITO layers has prompted the electrochemical deposition of anisotropic gold nanostructures with a clear dichroic behavior of their surface plasmon resonance absorption.

3.2 Experimental set up

For this work, ITO thin films have been prepared in an e-beam evaporator set-up previously described f in chapter 2 [19] [46] . Values of α= 60º, 70º, 80º and 85º have been used for the films deposited in the absence of plasma, while only α=80º was used when assisting the film growth with a plasma. This limitation stems from geometrical constrains of the deposition chamber where this value of α is determined by the position of the plasma source. The film growth was exposed under Ar, O_2 And Ar:O_2 mixtures.

The experimental set-up used for the plasma assisted GLAD of thin films is shown in Figure 1. The utilized plasma source was a microwave (MW) operated device (2.45 GHz, 460 W) consisting of a bell jar supplied through its upper part with the plasma gas (O_2, Ar and mixtures of these two gases). The major challenge of this modification of GLAD-PVD technique was get to connect plasma in a pressure range of evaporation process, for this reason the fource can work under "Electron Cyclotron Resonant" conditions (ECR).A pressure of 10^{-4} torr was always kept in the interior of the deposition chamber during e-beam evaporation, either in the presence or in the absence of the plasma.

Although no direct measurement of the pressure is possible in the bell jar of the plasma source, a value of 3-5x10^{-4} torr is expected in its interior. An evaporation rate of 0.7-1.0 A s^{-1} was set at the sample position. The plasma source was ignited before moving away a shutter that was covering the substrates for their protection.
In addition, for this experimental set-up, mass flow meters were adapted to control and carry out depositions under several gas mixtures.

To adapt this plasma source in conventional GLAD chamber is necessary to restrict the area of hold samples, which let a direct contact with the plasma for all

substrates. Therefore, in this chapter and chapter 4, Plasma GLAD thin films have been grown at constant deposition angle (80°).
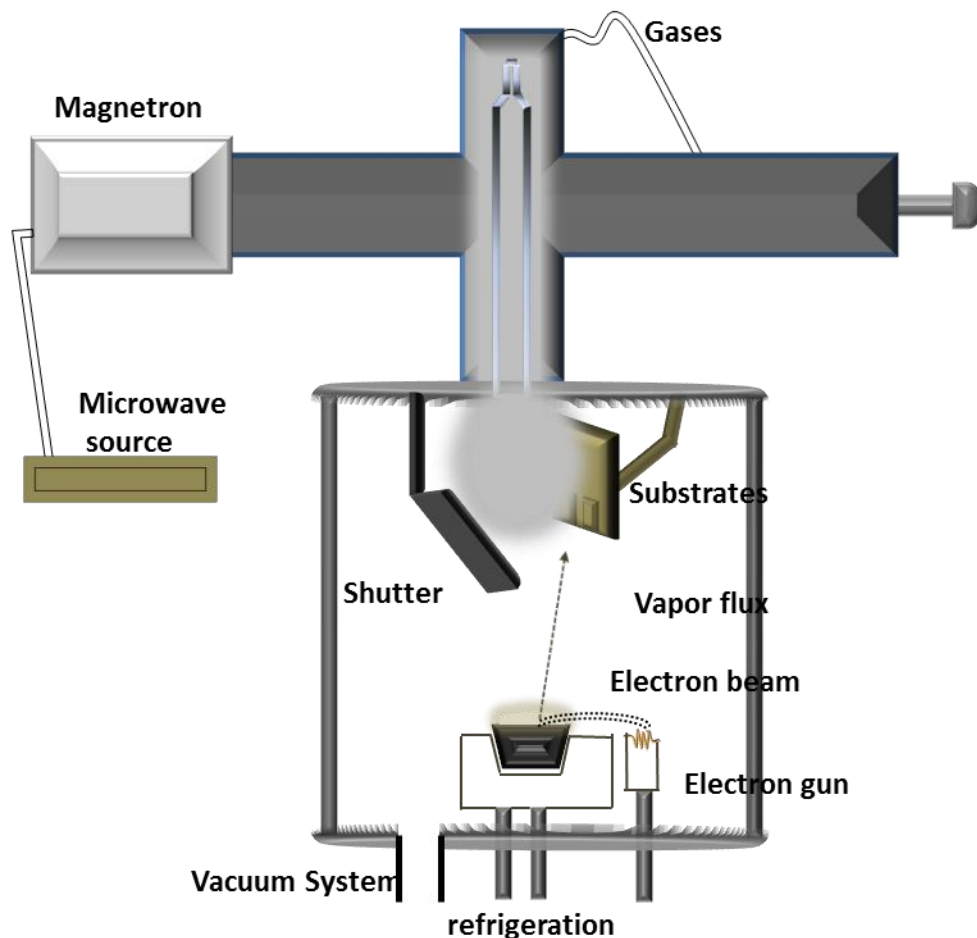
Figure 3.1. Scheme of the experimental set up used for the e-beam deposition of ITO films in an GLAD configuration while assisting their growth with a downstream plasma.

The ITO target, consisting of pellets supplied by Kurt J. Lesker. (In_2O_3/SnO_2 90%/10% (w/w)), were placed in a graphite crucible for e-beam bombardment. GLAD thin films were prepared on silicon wafers and quartz plates for specific characterization essays. Commercial ITO plates, supplied by VisionTek Systems Ltd (4 ohms/sq ITO 370 nm thick ITO), were used as substrates for the

GLAD of ITO films intended for the electrochemical deposition of gold and other characterization studies.

3.2.1 Thin films characterization

The microstructure of the films was characterized for the samples prepared on silicon wafers. They were diced for their lateral examination with a SE microscope HITACHI-S-5200 operated at 2KV.

GISAXS characterization studies were carried out at the P03 synchrotron beam-line of the PETRA III facility (Hamburg), using a wavelength of 0.168 Å and a sample to detector distance of 2.5 m.[52] The scattering signal was recorded with a 2D detector (Pilatus 300k fast with 172 μm pixel size). For each sample two different patterns were recorded, either by placing the films oriented with the tilted nanocolumns facing the polarization plane of the X-ray beam or in the direction perpendicular to it. Only spectra for this latter configuration, where the X-ray impinges perpendicular to the plane containing the tilted nanocolumnar structure, will be presented here for discussion. Details about data acquisition and calculation can be found in previous publications.[19,53,54] All examined films had a similar thickness of 500 nm.

In-depth elemental profiles and average Sn/In ratios were determined by Rutherford Back Scattering (RBS). The spectra were taken in a 3 MeV tandem accelerator at the CNA (Sevilla, Spain) with a proton beam of 1.5 MeV. Back scattered particles were recollected with a tilted Si detector at 165º for the sample holder tilted by 7º with respect to the beam. The RBS spectra were simulated with the SIMRNA software.[55]

AFM characterization of the surface of the films was carried out with a Nanotec Dulcinea microscope (Spain). Scanning conductivity measurements were carried out with a current sensing module supplied with a conductive tip NT-MDT with a gold cover. The diameter of the conductive tip was 70 nm and it presented a resonance frequency of 190-325 KHz and a force constant of 5.5-22.5 N/m.

3.2.2 Electrical measurements

Cross section and sheet resistance (although this term usually applies to homogeneous and compact thin films, we keep it here for simplicity) measurements were done with a Kietley 2635A System SourceMeter. For cross section measurements, GLAD thin films were grown on commercial ITO plates. Electrical measurements were done between the conductive substrate and a copper contact on the surface. Films grown on a quartz plate were used for sheet resistance determination. The measurements were done between two copper contacts deposited on the surface. These electrodes were spherical conductive adhesive copper spots of 3 mm diameter separated by 8 mm. The I-V curves were obtained with a compliance of 10^{-3} A. The used voltage ranged between $-4*10^{-3}$ to $4*10^{-3}$ V.

3.2.3 Electrochemical deposition of gold

Films with a ~1.5 cm^2 working area were polarized at room temperature in a rectangular three-electrode electrochemical cell made of quartz. A saturated Ag/AgCl and a platinum foil were employed as reference and counter electrodes, respectively. Electrochemical measurements were performed with a computer controlled Autolab PGSTAT30 potentiostat. Gold was electrodeposited by the application of a constant current density (-300 µA cm^{-2}) during 400 seconds in an aqueous solution of 0.1 M $HAuCl_4$ in acetone as reported in refs.[56,57]

UV-Vis transmittance spectra were recorded during and after the electrochemical measurements with a DH-2000 light source equipped with halogen and deuterium lamps and a QE65000 high-resolution spectrophotometer from Ocean Optics.

3.3 Results

3.3.1 Morphology of GLAD and GLAD plasma assisted ITO thin films

Figure 3.2 shows normal and cross section SEM micrographs of a series of ITO thin films prepared in the absence of plasma at different zenithal angles from 60º to 85º under a pressure of 10^{-4} torr of O_2.

These micrographs show that the evaporated material aggregates in the form of individual tilted nanocolumns extending from the interface with the substrate to the surface of the film, due to shadowing effect explained in Chapter 1.

As the film thickness increases, these nanocolumns slightly bend to higher angles with respect to the perpendicular to the surface. Although this bending precludes a straightforward determination of the orientation angle (β) of nanocolumns for the whole film thickness, a rough estimation of β approaching the bended nanocolumns to straights gives average values around 45º for all the films, with negligible changes from β~41º for α=60º to β~46º for α=85º.

These values contrast with the tilting angles determined for thinner films of approximately 200 nm when the nanocolumns are not yet bended. In this case, well defined β values varying from ca. 25º (α=60º) to 43º (α=85º) can be determined.[45]

These tilting angles do not agree with the predictions of the heuristic tangent rule,[58] a discrepancy that we have recently explained by assuming a trapping process for the ballistic particles flying close to the deposited nanostructures.[45]

Another remarkable feature of these GLAD ITO nanostructures is that they are rather smooth and do not depict the typical feather-like termination characteristic of the nanocolumns of TiO_2 and other oxides evaporated in an GLAD configuration.[19,21] Other authors have obtained similar thin film microstructures for e-beam GLAD ITO films.[11,12]
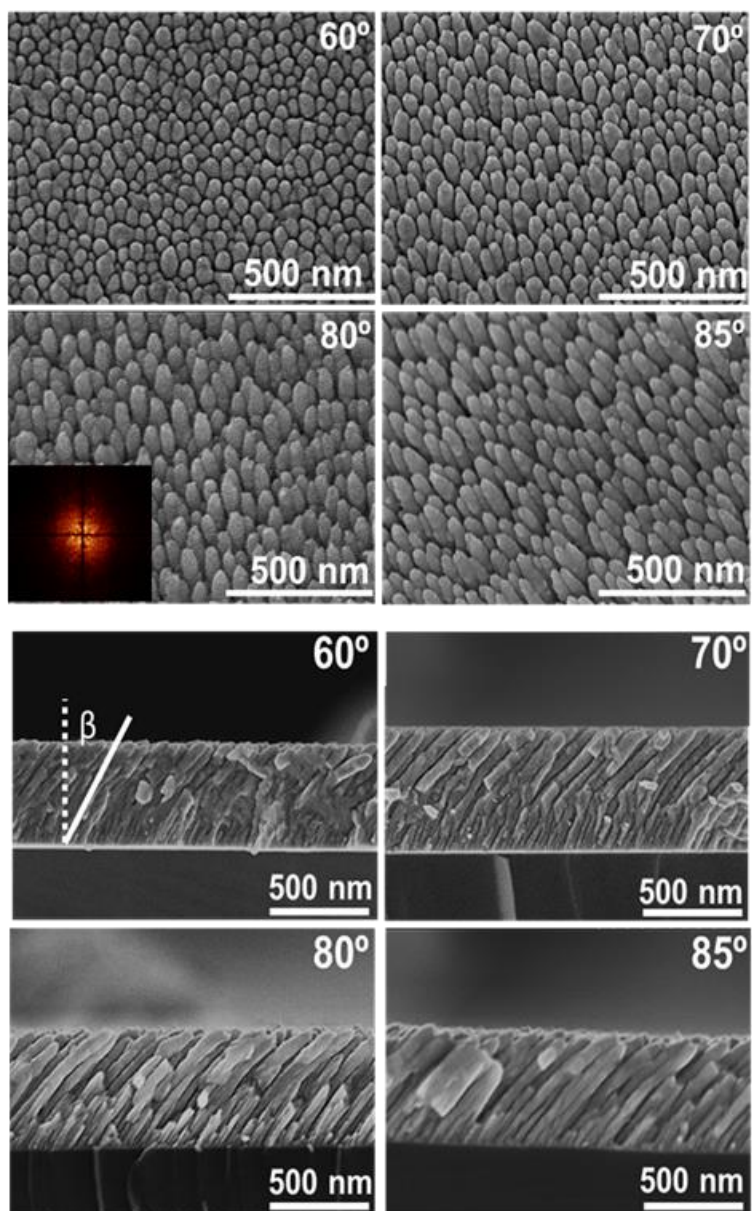
Figure 3.2. *Normal (top) and cross section (bottom) SEM micrographs of ITO thin films prepared by GLAD at the indicated zenithal angles from 60º to 85º in the presence of an oxygen pressure of 10^{-4} torr. The inset in the 80º normal SEM micrograph is the FFT of this image.*

When the growing films were exposed to plasma at a similar pressure of 10^{-4} torr, the morphology of the films experienced significant changes that affected the shape, size, agglomeration and tilting angle of the nanocolumns.

Figure 3.2 shows a series of normal and cross section SEM micrographs corresponding to ITO thin films prepared at a zenithal angle of 80º in the presence of several types of plasmas. As explained in the experimental section other evaporation angles were not possible because of experimental restrictions.

An outstanding characteristic of the microstructure of these plasma assisted GLAD thin films is that the nanocolumns are not isolated but associate in the form of bundles[14,43,48,49,59] that stretch along a direction perpendicular to the incoming flux of evaporated material.

In the first chapter was explained that bundling association of nanocolumns in GLAD thin films is a common phenomenon reported for a large variety of materials.[14,43,59]

.
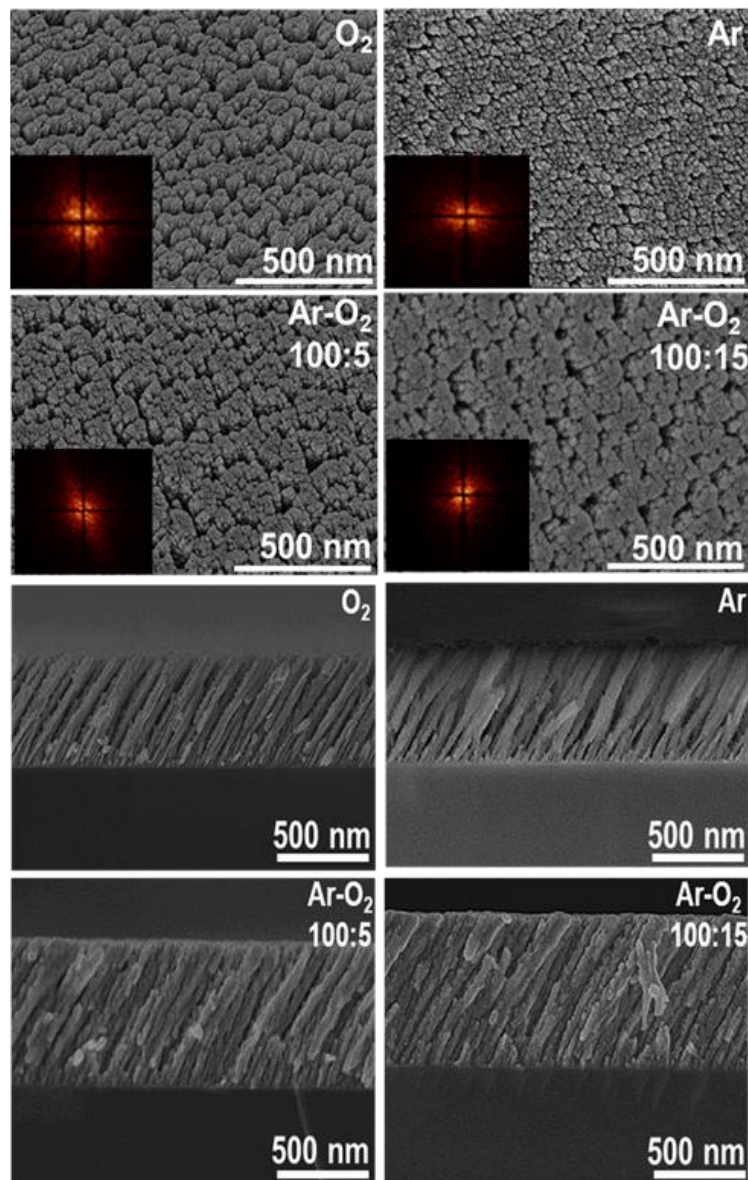
Figure 3.3*. Normal (top) and cross section (bottom) SEM micrographs of ITO thin films prepared by GLAD at a zenithal angle of 80º while assisting their growth with different types of plasma at an overall pressure of 10-4 torr. The insets in the normal SEM micrographs correspond to the FFT diagrams obtained from the normal SEM micrographs in each case (see text).*

Another important characteristic of the plasma assisted GLAD-ITO thin films is that the tilting angle β stays around 30 º, varying only slightly with the type of plasma gas (see Table 3.1).

A different growing mechanism for the plasma assisted GLAD-ITO thin films is clearly evidenced in Figure 3.4 showing a cross section micrograph of a stacked bilayer of ITO films sequentially deposited in the absence (bottom) and in the presence (top) of oxygen plasma.
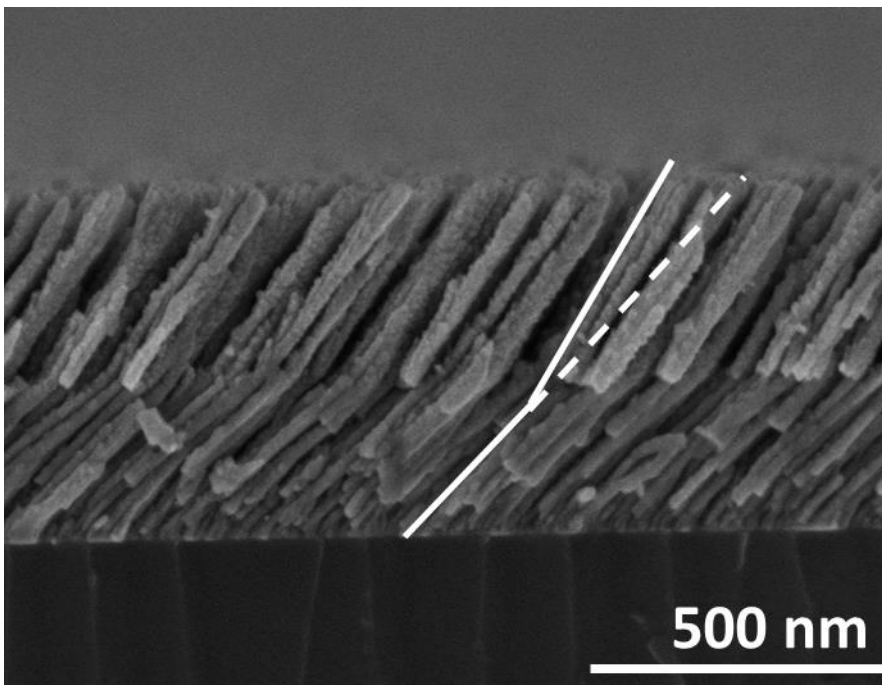
Figure 3.4. SEM cross section micrograph of a ITO bilayer prepared by GLAD, where the bottom layer has been prepared in the absence of plasma and the top layer by assisting the growth with a plasma of oxygen.

Table 3.1. Tilting angle of nanocolumns in the GLAD ITO films grown by assisting the thin film growth with different plasmas.

Plasma type	Tilting angle β
O_2	30º
Ar	24º
Ar:O2(100:5)	26º
Ar:O2 (100:15	25º
ITO GLAD 80º	46º

In Chapter 1 was demonstrated that GISAXS analysis of GLAD thin films can be a very powerful technique to retrieve information about possible anisotropy in the bulk and to determine the existence of specific correlation distances between the nanocolumnar features.[53,54]

Figure 3.5 shows a series of GISAXS patterns of ITO thin films deposited at different zenithal angles in the absence of plasma and for the plasma assisted films deposited at α=80º.

Except for the pattern of the ITO compact thin film (i.e., a commercial ITO plate), the patterns recorded for the GLAD films are characterized by an asymmetric shape indicative of a tilted orientation of the nanocolumns with respect to the film surface.[53,54] Moreover, the development in all cases of well-defined maxima proves the existence of specific correlations distances between the basic microstructural units of the films (i.e., the existence of a repetitive distance that, on average, separate these microstructural units).
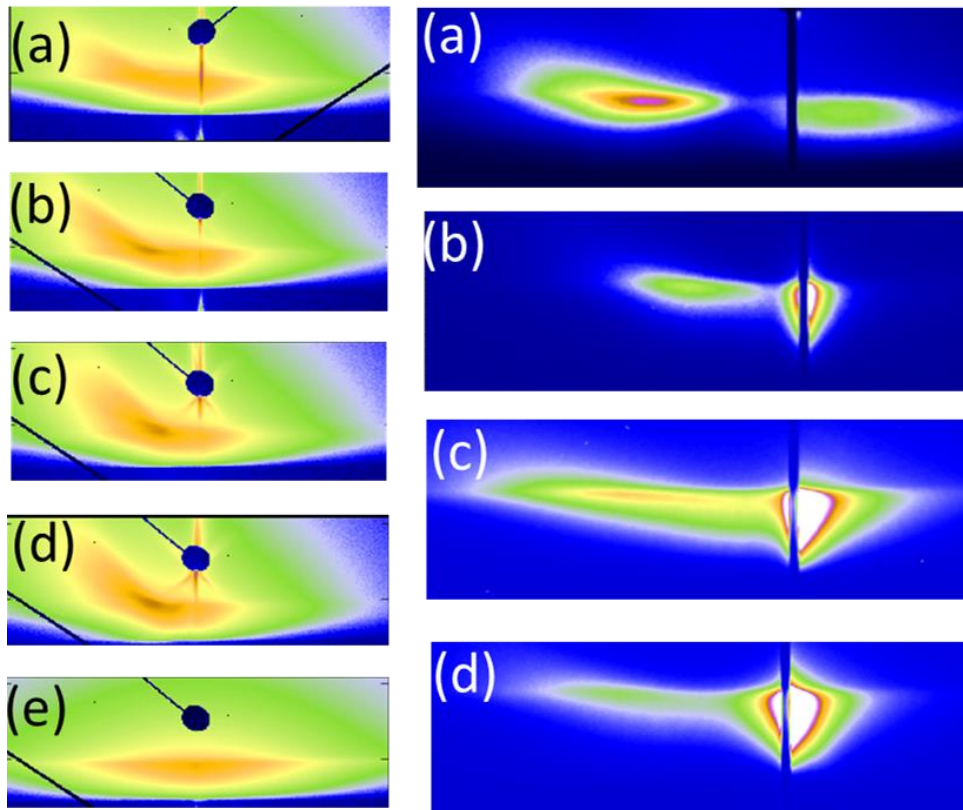
Figure 3. 5. *GISAXS patterns of ITO thin films. (left) Thin films deposited at different zenithal angles α in the absence of plasma: 60° (a), 70° (b), 80° (c), 85° (d), compact ITO thin films (e). (right) Thin films deposited at α=80° under the assistance of the following plasmas: Ar (a), O_2 (b), Ar:O_2 (100:5) (c), Ar:O_2 (100:15) (d). The color scale is indicative of the scattering intensity.*

Figure 3.6 shows the values of the grain sizes estimated from the Bearing plots of the AFM images that are higher than GISAXS correlation distances (see Table 3.2). Similar differences were found in a previous work for GLAD TiO_2 thin films reported in previous work of the group.
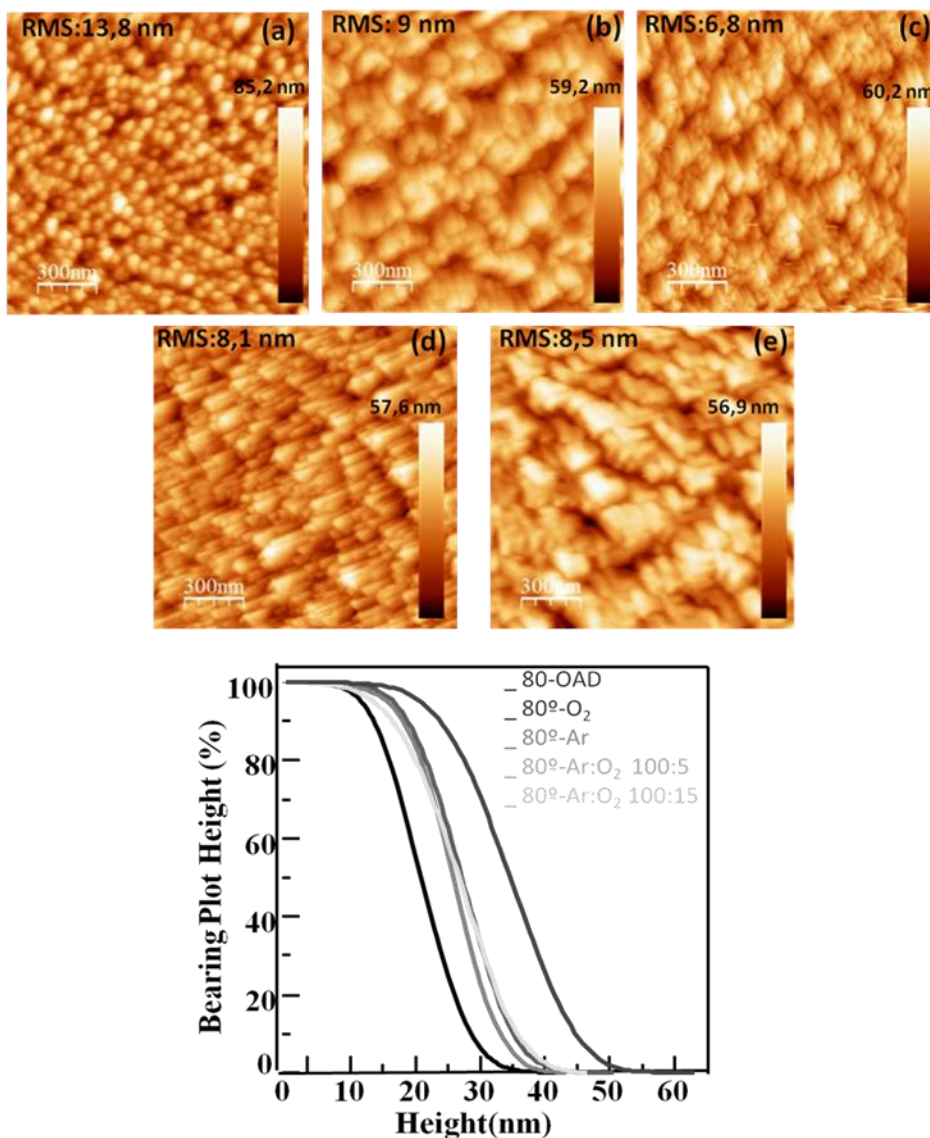
Figure 3.6.*- AFM images (top) of the surface of the ITO thin films, 80º GLAD (a) 80º-O₂ plasma (b), 80º-Ar plasma (c), 80º-ArO₂ 100:5 plasma (b), 80º-ArO₂ 100:15 plasma (d).Bearing plots (down) determined from the surface roughness estimated of the AFM images of the films. Average grain sizes are approximated to by the height values at 50% of the plot height.*

Table 3.2 summarizes the values of these correlation distances for the examined films and show that the average separation between nanostructures in the O_2 plasma assisted films is slightly larger than in the evaporated films or in the films grown in the presence of a plasma of Ar.

Since the GISAXS values are averaged through the whole thickness of the films and the nanocolum width usually increases with this parameter[60,61] it is expected that the surface periodicity deduced from an AFM analysis of roughness defined by the nanocolumn termination differs from the GISAXS correlation distances.

Table 3.2 Correlation distances determined from GISAXS patterns and surface periodicity determined from the AFM images of the same samples.

Zenithal deposition angle/type of plasma	GISAXS correlation distances (nm)	Averaged urface grain sizes deduced from AFM images (nm)
60º	11	-
70º	14	-
80º	16	25
85º	18	-
80º -O2 plasma	17	37
80º- Ar plasma	23	32
80º Ar:O2 plasma (100:5)	17	30
80º Ar:O2 plasma (100:15)	18	31

Figures 3,7 shows additional differences in surface topography between the GLAD and GLAD plasma assisted thin films can be also deduced from a detailed analysis of their normal SEM micrographs showing that at the surface of the plasma assisted films the nanocolumns are interconnected in the form of extended bundles.
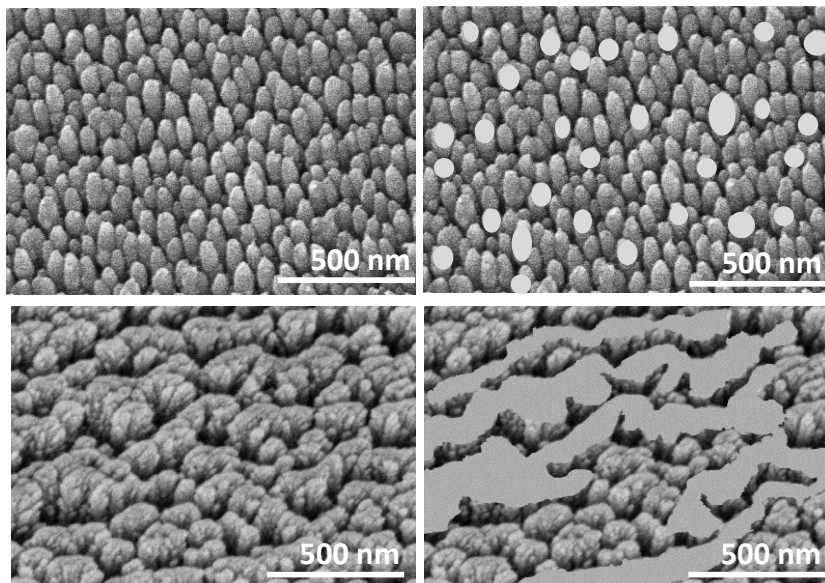
Figure 3.7.- SEM images of the surface of the ITO thin films, 80º GLAD (top) 80º-O_2 plasma (down). The plotted areas in the right side images highlight the surface zones that are interconnected in the two cases.

This visual assessment is confirmed by the 2D Fourier transform (FFT) plots of these images reported as insets in Figures 3.2 and 3.3 that depict an asymmetric shape for the plasma GLAD thin films, but a symmetric rounded shape for the 80º thin films deposited in the absence of plasma.

This difference sustains that in the plasma assisted films the surface grains are associated in the form of bundles along a preferential direction perpendicular to the incoming material flux. A similar conclusion can be gained by looking to the topographic AFM profiles along these two perpendicular directions.

The comparison between the line profiles of the 80º GLAD and the 80º GLAD O_2 plasma assisted films along two perpendicular directions clearly confirms the existence of a preferential bundling association direction of nanocolumns in the latter case is showed in the figure 3.8

For the O_2 plasma sample, the roughness variation amplitude is higher in the direction perpendicular to the vapor flux than in the parallel direction, while is

rather similar irrespective of the chosen direction for the sample prepared in the absence of plasma.
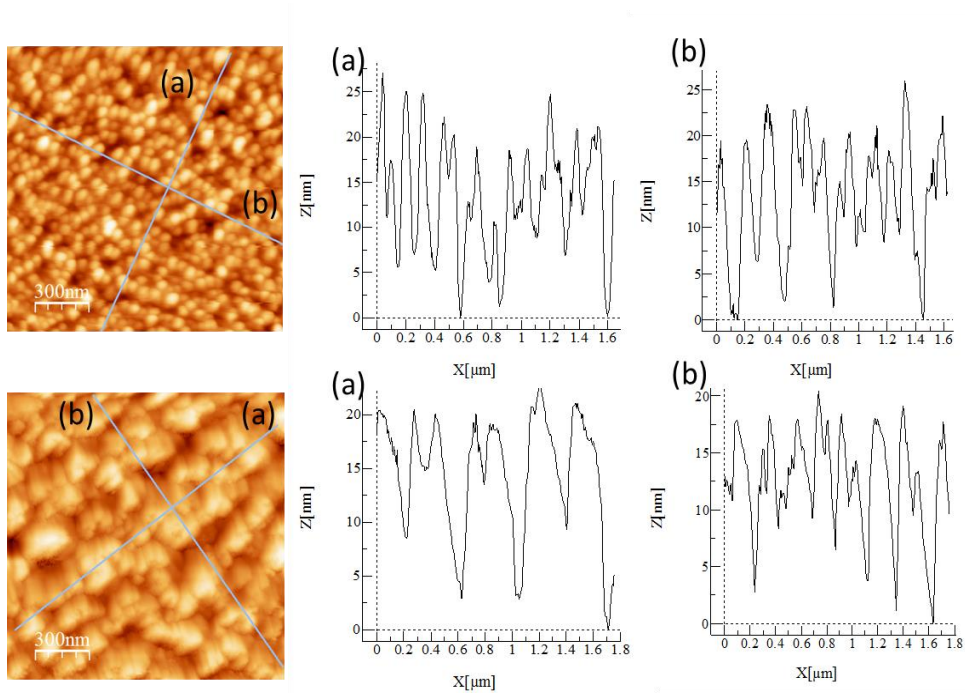
Figure 3.8.- *Left) AFM images of the surface of the ITO thin films, 80º GLAD (top) and 80º-O$_2$ plasma (down). Right) Line profiles measured for these samples along a perpendicular (a) and parallel (b) directions to the material flux as indicated in the AFM images.*

3.3.2 Chemistry, crystalline structure and porosity

E-beam evaporation of complex materials like ITO may induce changes in stoichiometry due to the preferential evaporation of one of the components. The "as-prepared" ITO thin films deposited in the absence of plasma were amorphous when examined by X-ray diffraction and presented a dark coloration indicating a certain lack of oxygen with respect to the stoichiometric mixed oxide.

The plasma assisted films, although also amorphous, were less dark when their growth was assisted with a plasma of oxygen (or mixtures oxygen plus argon). As evidenced by SEM analysis in figure 3.9, after annealing in O$_2$ at 350ºC for 6

hours all the GLAD ITO films became transparent and crystalline and kept a microstructure similar to that of the original samples
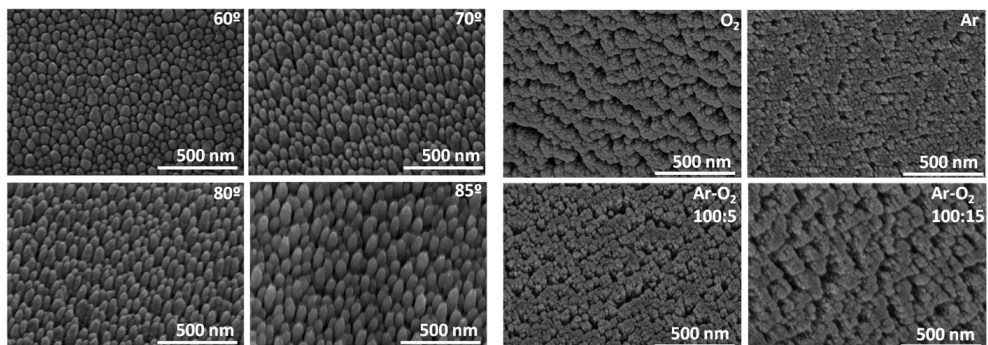
Figure 3.9*- Normal SEM micrographs after calcinations treatment of ITO thin films prepared by GLAD at the indicated zenithal angles from 60º to 85º and ITO thin films prepared by GLAD at a zenithal angle of 80º while assisting the growth of the films with different types of plasma.*

The X-ray diagrams of the annealed samples reported in Figure 3.10 are characterized by well defined peaks attributed to ITO (see for comparison the equivalent diagram for the commercial ITO film) and, in the case O_2 or mixtures of O_2/Ar plasma assisted films, some small peaks due to SnO_2. This minority segregation of tin oxide did not significantly affect the conductivity or optical properties of the films (see below) and no further discussion will be carried out here on this question.
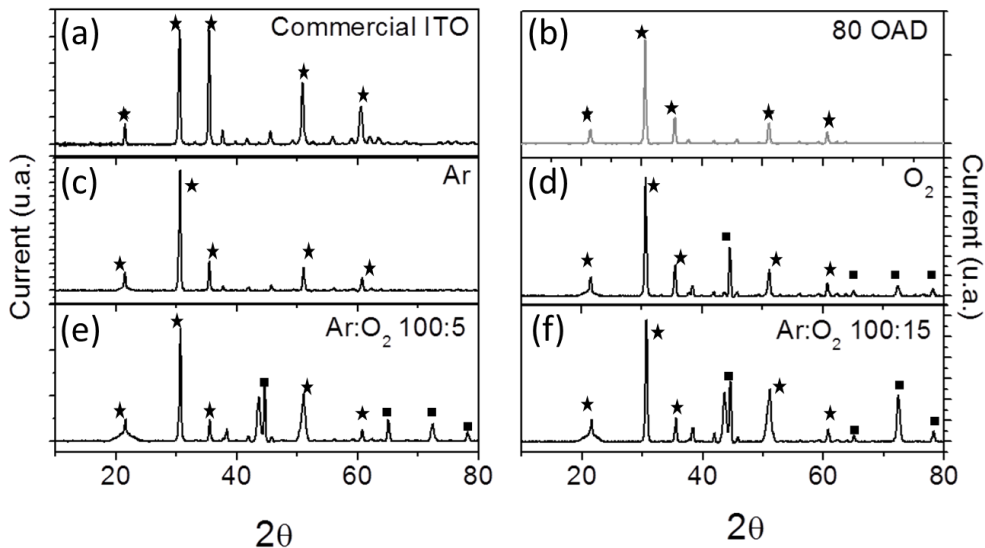
Figure 3.10 *XRD diagrams of the ITO thin films after their annealing in oxygen at 350º. (a) Commercial ITO included for comparison. (b)-(f) diagrams of GLAD and GLAD plasma assisted thin films as indicated. Peaks highlighted with a star correspond to crystalline ITO, those denoted with squares to a SnO_2 segregated phase.*

The O/(In+Sn) atomic ratio and the elemental depth distribution of the films were determined by RBS. The results of this analysis (see Table 3.3) show that the relative content of oxygen is higher in the plasma assisted films and that it slightly increases after annealing, in agreement with the color bleaching induced by this treatment. The relatively higher content of oxygen determined for the plasma assisted film agrees with the enrichment in Sn deduced from the XRD diagrams (Figure 3.10) (in In_2O_3 the O:In ratio is 1.5, while it is 2 for SnO_2).

Table 3.3. Mass thickness, elemental percentages and ratios and density of GLAD ITO thin films determined by RBS

Sample	Mass thickness (10^{15}at/cm^2)	[Sn]+[In] (%at)	[O] (%at)	[O]/ [Sn]+[In]	Density g/cm^3
ITO-80º	2250	39	61	1,56	3,7
ITO-80º/300ºC	2400	39	61	1,56	4,3
ITO –O2 plasma	2700	27	48	1,77	3,5
ITO-O2 plasma /300ºC	2400	32	59	1,84	3,9
ITO-Ar plasma	2700	30	55	1,83	3,8
ITO-Ar plasma/300ºC	2500	35	61	1,74	4,3
Commercial ITO	1450	39	61	1,56	7,2

Film densities were also determined by comparing their mass thicknesses obtained by RBS with the actual thicknesses estimated by direct observation of the cross section micrographs in Figures 3.2 and 3.3. In comparison with the density determined for the commercial ITO, the densities gathered in Table 3.3 for the GLAD films are consistent with porosities of the order of 40-50% of their total volume, in good agreement with similar oxide thin films prepared by e-beam GLAD.[19] It is also worth stressing that the pore volume remains almost unaltered by annealing, thus confirming that the microstructure does not significantly vary after this treatment (Figure 3.9).

3.3.3 Electrical conductivity

The annealed GLAD films were transparent in the visible and presented a significant absorption in the near infrared, a typical characteristic attributed to a high concentration of free electrons in TCO materials.[1,2] To characterize the electrical transport properties of the GLAD thin films we have measured their conductivity both at microscopic and macroscopic levels.

The scanned conductivity maps reported in Figure 3.11 show that most surface features with a high conductivity roughly coincide with the protrusions observed in the topographic AFM images. This proves that in the GLAD ITO thin films the in-depth conductivity mainly involves a preferential charge transport through the nanocolumns of the films. Moreover, the measured I-V curves at these sites reveal similar local conductivity values for the GLAD and commercial ITO films and a transport pattern approaching an ohnmic behavior in all cases.
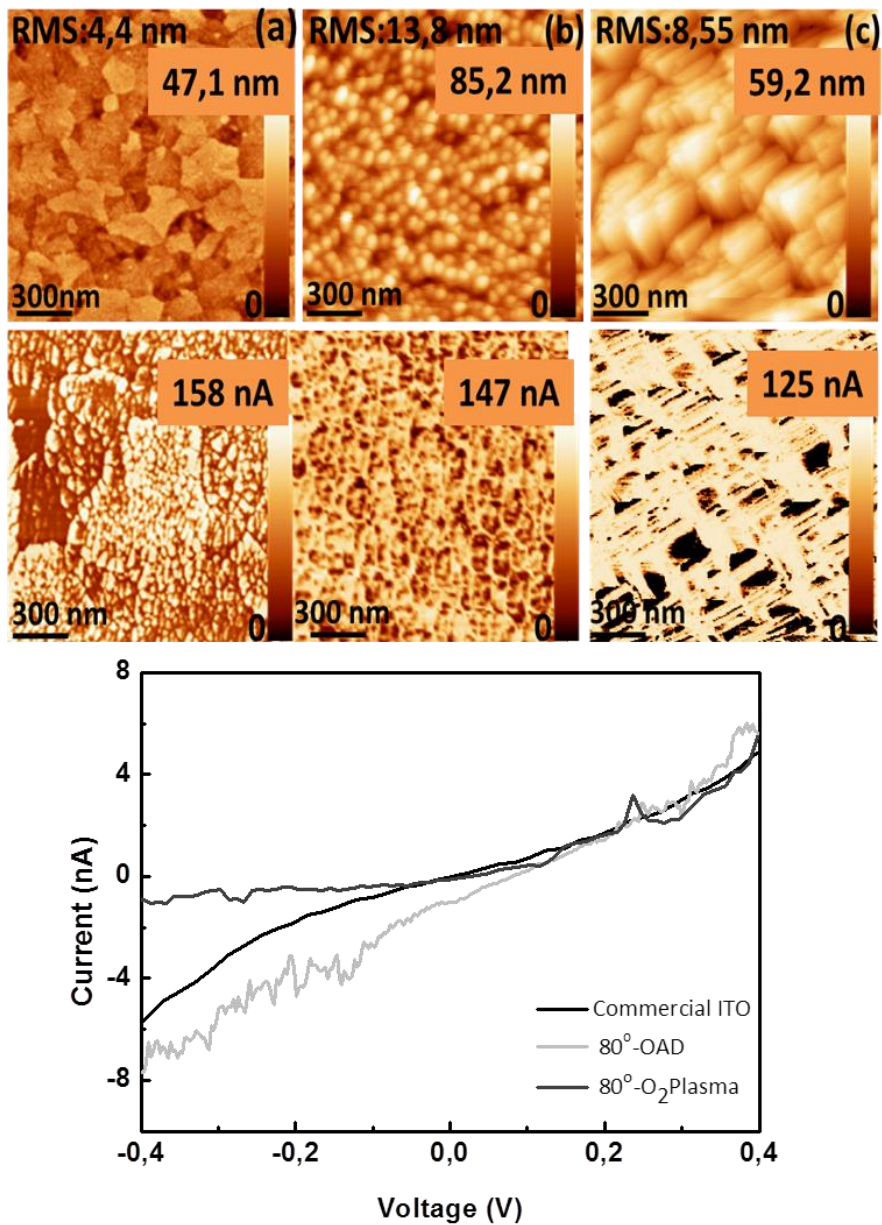
Figure 3.11. Topographic (top) and conductive scanning microscopy (down) images recorded for a commercial ITO film (a) and the indicated GLAD thin films: 80º GLAD (b) and 80º-O_2 plasma (c). The graphs in panel (d) correspond to I-V curves measured with the AFM tip placed on a position with a maximum conductivity.

Although the similar conductivities at microscopic level between the compact and GLAD ITO films supports that the electronic characteristics of the examined materials are rather similar, this does not imply that their macroscopic conductivity should be similar too.

Macroscopic cross-section and "sheet" conductivity measurements were carried out as described in the experimental section and the obtained I-V curves depicted a typical resistive Ohnmic behavior. The resistivity values reported in Table 3.4 show that the in-depth and sheet conductivities of the commercial ITO films used as reference are higher than those of the GLAD ITO films, a difference that must be attributed to the smaller density and nanocolumnar microstructure of these samples.

Table 3.4. Sheet and in-depth resistivity values of GLAD and GLAD plasma assisted ITO films

Sample	In-depth resistivity $(\Omega*cm)(10^{-2})$	Sheet resistivity (bundling direction) $(\Omega*sq)(10^{-2})$	Sheet resistivity (perpendicular direction) $(\Omega*sq)(10^{-2})$
Commercial ITO plate	6,3	2,1	2,2
80º -OAD	20,1	48,7	69,7
80º -O_2 Plasma	40,8	84,4	6624
80ºAr Plasma	19,5	55,5	123,1

In addition, while the sheet conductivities in the commercial ITO films are equivalent for two perpendicular surface directions, quite different conductivity values were determined in the plasma assisted films along the bundling and perpendicular directions.

This difference proves that the bundling direction defines a preferential electrical pathway due to the lateral association of nanocolumns and that these pathways are disrupted in the perpendicular direction. The difference is particularly worth noting for the O_2 plasma film where the resistivity in the direction perpendicular to the bundling direction is comparatively very high. To our

knowledge no similar in-plane electrical anisotropy has been previously reported for other GLAD thin films.

3.3.4 Surface anisotropy and fabrication of dichroic thin films

A typical application of ITO thin films consists of using them as electrodes for different purposes, including the development of sensors, nanoparticle deposition, etc.[50,51,62,63] Herein, we propose to exploit the bundling surface and conductivity anisotropies of the plasma assisted GLAD thin films for the development of dichroic thin films. In previous works on plasmon anticounterfeiting films we proposed the use of GLAD SiO_2 thin films as hosts or templates for, respectively, the fabrication of embedded anisotropic gold nanoparticles[51] or Ag surface nanostrips after evaporation and laser treatment.[50] The strategy proposed here consists of using the plasma assisted GLAD ITO films as electrodes to directly deposit Au nanostructures with surface plasmon resonance activity.[50,51]

Electrochemical deposition of gold on the GLAD ITO films leads to the formation of nanoparticles and/or nanostructures both on the film surface and in its interior. The normal and cross section SEM micrographs reported in Figure 3.12 show that small gold nanoparticles form on the surface of the 80º GLAD-ITO film, mainly at the tip of the nanocolumns. A reduced number of nanoparticles also form in the interior of the film. By contrast, in the plasma assisted GLAD ITO films, gold forms elongated aggregates in the hollow surface regions separating the nanocolumnar bundles, as well as in the pores separating these bundles in the interior of the films.

The total amount of gold deposited in each case was similar and corresponded to approximately $3,7*10^{15}$ atoms/cm^2 of gold as determined from the total current exchanged during the deposition process.
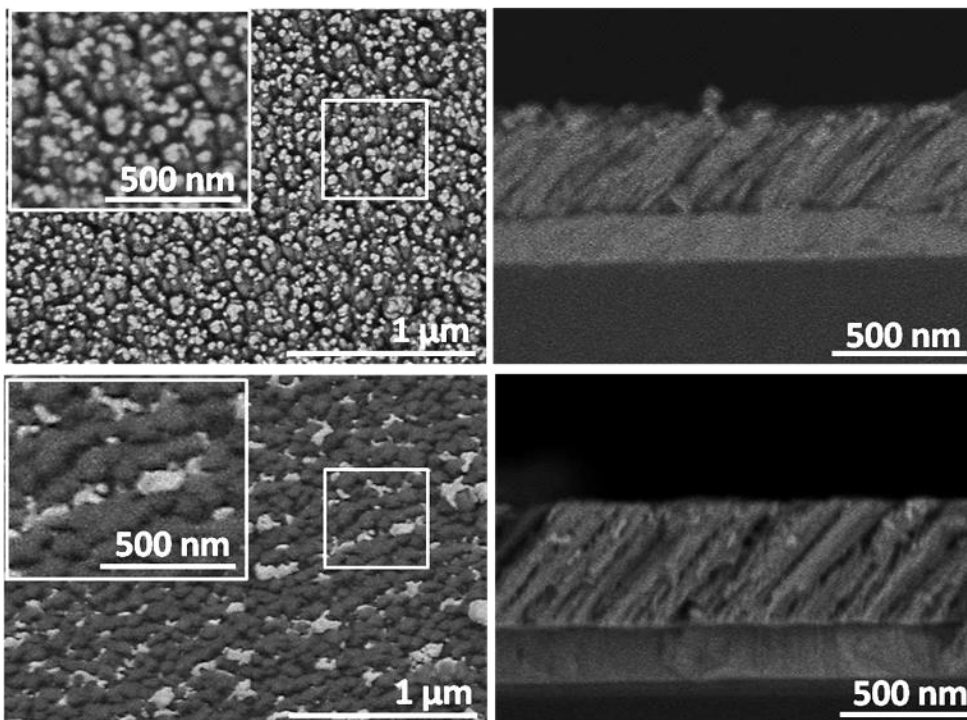
Figure 3.14. *Normal (left) and cross section (right) SEM micrographs of 80°- GLAD (top) and 80°-O$_2$ Plasma (down)ITO thin films after the electrochemical deposition of gold. The enlarged views included as insets in the normal SEM micrographs show the different shape of the gold aggregated formed on the surface of these two types of thin films.*

The different distribution of gold in the two kinds of ITO films yields two types of surface plasmon resonances. Figure 3.13 shows the UV-vis spectra recorded with linearly polarized light for two azimuthal orientations of the films defined along the bundling direction in the plasma assisted GLAD films (0° polarization) or the perpendicular to it (90° polarization).

For these two orientations, the spectra of the evaporated ITO films depict a similar absorption band at 535 nm attributed to the surface plasmon resonance of the electrochemically deposited gold nanoparticles.[50,51,64,65] Conversely, in the plasma assisted film, azimuthally turning the sample leads to significant changes in the absorption spectra. At 0°, the spectrum is characterized by a well-defined

resonance peak at 520 nm, while at 90º it depicts a less resolved structure where two brGLAD and little resolved bands at 580 nm and 700 nm can be seen.

This change renders a clear variation in the color of the sample as evidenced by the photographs shown in the Figure. A similar behavior has been reported in previous studies on anisotropic gold nanoparticles embedded in GLAD SiO_2 thin films.[49] This dichroic behavior can be attributed to a different plasmon resonance response when aligning the polarization vector of the light along the longest or shortest dimensions of the gold nanostructures.[66]
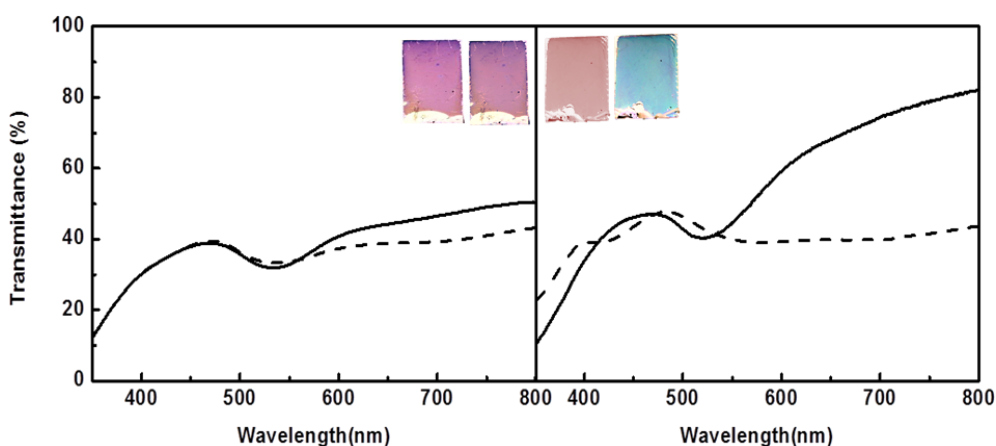
Figure 3.13. *UV-vis transmittance spectra recorded with linearly polarized light 0º (dashed line) and 90º (full line) for gold electrochemically deposited on a 80º GLAD ITO (left) and 80º-O_2 Plasma ITO (right). The images clearly show the different aspect of the films examined with the two orientations of the polarized light.*

3.4 Discussion

Such as have been comented in the Chapter 1 , the bundling association of nanocolumns has been neither sufficiently explained nor exploited to get new complex nanostructures. In general, it is more common in metals[17] than in oxides[13,19,20] and therefore it seems associated with the different mobility and/or trapping probability of the species impinging onto the growing films.

In a recent discussion about the heuristic "tangent rule"[45] relating the tilting angle of the nanocolumns (β) with the zenithal evaporation angle (α). R. alvarez et all have proposed that this dependence can be explained by assuming that the deposition particles flying close to the surface can be trapped before impinging onto it. Such a trapping mechanism would cast an effective shadowing behind the growing nanostructures that would depend on an effective "trapping parameter" different for each material.

Using a Monte Carlo simulation model, it has been demonstrated demonstrated that β decreases for higher trapping probabilities, having a value of approximately 0.3 for GLAD ITO. The decrease in the tilting angle found here for the plasma assisted GLAD films would imply an increase in this parameter to a value close to one. Although the reasons accounting for this increase in the surface trapping probability in the presence of a plasma still require an specific investigation, we can anticipate that the electrical field associated to the sheath formed on the surface of the growing film exposed to the plasma[67] must be a critical factor enhancing the trapping probability of the deposition particles.

Besides a change in the nanocolumnar orientation, the morphological analysis of the plasma assisted films are characterized by an enhancement in the bundling association of the nanocolumns. The hypothesis of an enhancement of the trapping probability under the action of the plasma can also explain the development of bundling since this phenomenon would not only occur at the nanocolumn tips but also at their sides, whereby favoring their lateral growth and association such as have been explained in chapter 1.

Similarly to other GLAD metal oxides prepared at room temperature where only pure ballistic deposition processes are involved[1], the "as-deposited" ITO samples were amorphous. To get transparency in the visible, absorption in the NIR and electrical conductivity, the films were annealed in air at 350ºC, a treatment that produces their crystallization and complete oxidation.

The crystalline GLAD ITO films presented sheet and in-depth conductivities that differ from those of dense ITO films, a difference that has been related to their microstructure formed by tilted and separated nanocolumns.

Distinct in-depth and sheet electrical conductivities have been reported for a wide variety of thin film materials[68,69] characterized by a different arrangement of the microstructural or molecular units in-depth or laterally. The additional in-plane anisotropy found in the plasma assisted GLAD ITO thin films is an outstanding new feature that we have linked with the association of nanocolumns in the form of bundles and the definition of separated conductivity path-ways along them.

The prospects of use of this feature are enormous and in the present work we have exploited a first possibility consisting of the electrochemical fabrication of dichroic films based on the surface plasmon resonance response of gold nanostructures. The different shape of the deposited aggregates found on the GLAD and GLAD plasma assisted ITO films must be related with local variations in the electrical potential at the surface. On GLAD thin films the homogenous distribution of equally sized and round nanoparticles formed on the tips of the nanocolumns (cf. Figure 3.12) must be associated with an enhancement of the electrical field at these sit

3.5 Conclusions

The previous results and discussion have shown that the microstructure of GLAD ITO thin films can be modified by exposing the growing films to a plasma. The observed decrease in the tilting angle and the bundling association of nanocolumns have been attributed to a higher trapping probability of the evaporated particles along their trajectory in the vicinity of the film.

Both the GLAD and the plasma assisted GLAD ITO films present different in-depth and sheet conductivities as expected for their porous and nanocolumnar structure. In addition, the anisotropic in-plane conductivity behavior found in the plasma assisted samples has been associated with the definition of preferential conductivity tracks along the bundling direction of nanocolumns.

The surface anisotropy of these samples has been utilized in the present work for the electrochemical deposition of elongated gold nanoparticles. The obtained composite films present a dichroic behavior when examined with polarized light. It is expected that these anisotropic thin films can be used for other applications where transparency and in-plane electrical anisotropy are relevant issues.

REFERENCES

(1)   Granqvist, C. G.; Hultåker, A. *Thin Solid Films* **2002**, *411* (1), 1–5.

(2)   Kumar, A.; Zhou, C. *ACS Nano* **2010**, *4* (1), 11–14.

(3)   Sunde, T. O. L.; Garskaite, E.; Otter, B.; Fossheim, H. E.; Sæterli, R.; Holmestad, R.; Einarsrud, M.-A.; Grande, T. *J. Mater. Chem.* **2012**, *22* (31), 15740–15749.

(4)   Wang, T.; Radovanovic, P. V. *J. Phys. Chem. C* **2011**, *115* (2), 406–413.

(5)   Kim, S. I.; Jung, T. D.; Song, P. K. *Thin Solid Films* **2010**, *518* (11), 3085–3088.

(6)   Jung, Y. S.; Lee, S. S. *J. Cryst. Growth* **2003**, *259* (4), 343–351.

(7)   Ikenoue, T.; Sakamoto, S.; Inui, Y. *Phys. Status Solidi C* **2014**, *11* (7-8), 1237–1239.

(8)   Ali, H. M.; Mohamed, H. A.; Mohamed, S. H. *Eur. Phys. J. Appl. Phys.* **2005**, *31* (2), 87–93.

(9)   Sood, A. W.; Poxson, D. J.; Mont, F. W.; Chhajed, S.; Cho, J.; Schubert, E. F.; Welser, R. E.; Dhar, N. K.; Sood, A. K. *J. Nanosci. Nanotechnol.* **2012**, *12* (5), 3950–3953.

(10)   Zhong, Y.; Shin, Y. C.; Kim, C. M.; Lee, B. G.; Kim, E. H.; Park, Y. J.; Sobahan, K. M. A.; Hwangbo, C. K.; Lee, Y. P.; Kim, T. G. *J. Mater. Res.* **2008**, *23* (09), 2500–2505.

(11)   Rider, D. A.; Tucker, R. T.; Worfolk, B. J.; Krause, K. M.; Lalany, A.; Brett, M. J.; Buriak, J. M.; Harris, K. D. *Nanotechnology* **2011**, *22* (8), 085706.

(12)   Van Dijken, J. G.; Brett, M. J. *J. Vac. Sci. Technol. Vac. Surf. Films* **2012**, *30* (4), 040606.

(13)   Leem, J. W.; Yu, J. S. *Opt. Express* **2011**, *19 Suppl 3*, A258–A268.

(14)   Van Kranenburg, H.; Lodder, C. *Mater. Sci. Eng. R Rep.* **1994**, *11* (7), 295–354.

(15)   Hawkeye, M. M.; Taschuk, M. T.; Brett, M. J. *Glancing angle deposition of thin films: engineering the nanoscale*; 2014.

(16)   Hawkeye, M. M.; Brett, M. J. *J. Vac. Sci. Technol. Vac. Surf. Films* **2007**, *25* (5), 1317.

(17)   Chen, L.; Lu, T.-M.; Wang, G.-C. *J. Appl. Phys.* **2012**, *112* (2), 024303.

(18)   Hara, K.; Kamiya, M.; Hashimoto, T.; Okamoto, K.; Fujiwara, H. *Thin Solid Films* **1988**, *158* (2), 239–244.

(19)   González-García, L.; Parra-Barranco, J.; Sánchez-Valencia, J. R.; Barranco, A.; Borrás, A.; González-Elipe, A. R.; García-Gutiérrez, M.-C.; Hernández, J. J.; Rueda, D. R.; Ezquerra, T. A. *Nanotechnology* **2012**, *23* (20), 205701.

(20)   Schulz, U.; Terry, S. G.; Levi, C. G. *Mater. Sci. Eng. A* **2003**, *360* (1-2), 319–329.

(21)   Wang, S.; Xia, G.; He, H.; Yi, K.; Shao, J.; Fan, Z. *J. Alloys Compd.* **2007**, *431* (1-2), 287–291.

REFERENCES

(22) Basnet, P.; Larsen, G. K.; Jadeja, R. P.; Hung, Y.-C.; Zhao, Y. *ACS Appl. Mater. Interfaces* **2013**, *5* (6), 2085–2095.

(23) Merkel, J. J.; Sontheimer, T.; Rech, B.; Becker, C. *J. Cryst. Growth* **2013**, *367*, 126–130.

(24) Ehsani, M. H.; Rezagholipour Dizaji, H.; Azizi, S.; Ghavami Mirmahalle, S. F.; Hosseini Siyanaki, F. *Phys. Scr.* **2013**, *88* (2), 025602.

(25) Yang, B.; Duan, H.; Zhou, C.; Gao, Y.; Yang, J. *Appl. Surf. Sci.* **2013**, *286*, 104–108.

(26) González-García, L.; González-Valls, I.; Lira-Cantu, M.; Barranco, A.; González-Elipe, A. R. *Energy Environ. Sci.* **2011**, *4* (9), 3426–3435.

(27) Oliva-Ramirez, M.; González-García, L.; Parra-Barranco, J.; Yubero, F.; Barranco, A.; González-Elipe, A. R. *ACS Appl. Mater. Interfaces* **2013**, *5* (14), 6743–6750.

(28) He, Y.; Zhao, Y. *Nanoscale* **2011**, *3* (6), 2361.

(29) Martin, P. M. *Handbook of deposition technologies for films and coatings science, applications and technology*; Elsevier: Amsterdam; Boston, 2010.

(30) Parra-Barranco, J.; Oliva-Ramirez, M.; Gonzalez-Garcia, L.; Alcaire, M.; Macias-Montero, M.; Borras, A.; Frutos, F.; Gonzalez-Elipe, A. R.; Barranco, A. *ACS Appl. Mater. Interfaces* **2014**, *6* (15), 11924–11931.

(31) Schmidt, D.; Kjerstad, A. C.; Hofmann, T.; Skomski, R.; Schubert, E.; Schubert, M. *J. Appl. Phys.* **2009**, *105* (11), 113508.

(32) Xi, J.-Q.; Schubert, M. F.; Kim, J. K.; Schubert, E. F.; Chen, M.; Lin, S.-Y.; Liu, W.; Smart, J. A. *Nat. Photonics* **2007**, *1* (3), 176–179.

(33) Schubert, M. F.; Kim, J. K.; Chhajed, S.; Schubert, E. F. Ellison, M. J., Ed.; 2007; pp 667403–667403 – 7.

(34) Kim, J. K.; Chhajed, S.; Schubert, M. F.; Schubert, E. F.; Fischer, A. J.; Crawford, M. H.; Cho, J.; Kim, H.; Sone, C. *Adv. Mater.* **2008**, *20* (4), 801–804.

(35) Poxson, D. J.; Kuo, M.-L.; Mont, F. W.; Kim, Y.-S.; Yan, X.; Welser, R. E.; Sood, A. K.; Cho, J.; Lin, S.-Y.; Schubert, E. F. *MRS Bull.* **2011**, *36* (06), 434–438.

(36) Yan, X.; Mont, F. W.; Poxson, D. J.; Cho, J.; Schubert, E. F.; Kim, M.-H.; Sone, C. *J. Appl. Phys.* **2011**, *109* (10), 103113.

(37) Beaudry, A. L.; Tucker, R. T.; LaForge, J. M.; Taschuk, M. T.; Brett, M. J. *Nanotechnology* **2012**, *23* (10), 105608.

(38) Tucker, R. T.; Beaudry, A. L.; LaForge, J. M.; Taschuk, M. T.; Brett, M. J. *Appl. Phys. Lett.* **2012**, *101* (19), 193101.

(39) Taschuk, M. T.; Tucker, R. T.; LaForge, J. M.; Beaudry, A. L.; Kupsta, M. R.; Brett, M. J. *J. Appl. Phys.* **2013**, *114* (24), 244304.

(40) Beaudry, A. L.; LaForge, J. M.; Tucker, R. T.; Li, P.; Taschuk, M. T.; Brett, M. J. *Cryst. Growth Des.* **2013**, *13* (1), 212–219.

(41) Beaudry, A. L.; LaForge, J. M.; Tucker, R. T.; Sorge, J. B.; Adamski, N. L.; Li, P.; Taschuk, M. T.; Brett, M. J. *Nano Lett.* **2014**, *14* (4), 1797–1803.

(42) Sorge, J. B.; Taschuk, M. T.; Wakefield, N. G.; Sit, J. C.; Brett, M. J. *J. Vac. Sci. Technol. A* **2012**, *30* (2), 021507.

(43) Zhao, Y.; He, Y.; Brown, C. *Appl. Phys. Lett.* **2012**, *100* (3), 033106.

(44) Lalany, A.; Tucker, R. T.; Taschuk, M. T.; Fleischauer, M. D.; Brett, M. J. *J. Vac. Sci. Technol. Vac. Surf. Films* **2013**, *31* (3), 031502.

(45) Alvarez, R.; Lopez-Santos, C.; Parra-Barranco, J.; Rico, V.; Barranco, A.; Cotrino, J.; Gonzalez-Elipe, A. R.; Palmero, A. *J. Vac. Sci. Technol. B* **2014**, *32* (4), 041802.

(46) Sánchez-Valencia, J. R.; Blaszczyk-Lezak, I.; Espinós, J. P.; Hamad, S.; González-Elipe, A. R.; Barranco, A. *Langmuir* **2009**, *25* (16), 9140–9148.

(47) Tait, R. N.; Smy, T.; Brett, M. J. *Thin Solid Films* **1993**, *226* (2), 196–201.

(48) Sanchez-Valencia, J. R.; Toudert, J.; Borras, A.; Barranco, A.; Lahoz, R.; de la Fuente, G. F.; Frutos, F.; Gonzalez-Elipe, A. R. *Adv. Mater.* **2011**, *23* (7), 848–853.

(49) Gonzalez-García, L.; Parra-Barranco, J.; Sanchez-Valencia, J. R.; Ferrer, J.; Garcia-Gutierrez, M.-C.; Barranco, A.; Gonzalez-Elipe, A. R. *Adv. Funct. Mater.* **2013**, *23* (13), 1655–1663.

(50) Wang, L.; Mao, W.; Ni, D.; Di, J.; Wu, Y.; Tu, Y. *Electrochem. Commun.* **2008**, *10* (4), 673–676.

(51) Ma, Y.; Di, J.; Yan, X.; Zhao, M.; Lu, Z.; Tu, Y. *Biosens. Bioelectron.* **2009**, *24* (5), 1480–1483.

(52) Roth, S. V.; Döhrmann, R.; Dommach, M.; Kuhlmann, M.; Kröger, I.; Gehrke, R.; Walter, H.; Schroer, C.; Lengeler, B.; Müller-Buschbaum, P. *Rev. Sci. Instrum.* **2006**, *77* (8), 085106.

(53) Alvarez, R.; García-Martín, J. M.; Macías-Montero, M.; Gonzalez-Garcia, L.; González, J. C.; Rico, V.; Perlich, J.; Cotrino, J.; González-Elipe, A. R.; Palmero, A. *Nanotechnology* **2013**, *24* (4), 045604.

(54) González-García, L.; Barranco, A.; Páez, A. M.; González-Elipe, A. R.; García-Gutiérrez, M.-C.; Hernández, J. J.; Rueda, D. R.; Ezquerra, T. A.; Babonneau, D. *ChemPhysChem* **2010**, *11* (10), 2205–2208.

(55) Gil-Rostra, J.; Chaboy, J.; Yubero, F.; Vilajoana, A.; González-Elipe, A. R. *ACS Appl. Mater. Interfaces* **2013**, *5* (6), 1967–1976.

(56) Kanno, Y.; Suzuki, T.; Yamauchi, Y.; Kuroda, K. *J. Phys. Chem. C* **2012**, *116* (46), 24672–24680.

(57) Dudin, P. V.; Unwin, P. R.; Macpherson, J. V. *J. Phys. Chem. C* **2010**, *114* (31), 13241–13248.

(58) Palik, E. D. *Handbook of Optical Constants of Solids*; Academic Press, 2012.

(59) Pillai, P. P.; Pacławski, K.; Kim, J.; Grzybowski, B. A. *Adv. Mater.* **2013**, *25* (11), 1623–1628.

(60) Fractal Concepts in Surface Growth | Condensed matter physics, nanoscience and mesoscopic physics http://www.cambridge.org/us/academic/subjects/physics/condensed-

REFERENCES

matter-physics-nanoscience-and-mesoscopic-physics/fractal-concepts-surface-growth (accessed Nov 28, 2014).

(61)   Karabacak, T.; Singh, J.; Zhao, Y.-P.; Wang, G.-C.; Lu, T.-M. *Phys. Rev. B* **2003**, *68* (12).

(62)   Schaming, D.; Renault, C.; Tucker, R. T.; Lau-Truong, S.; Aubard, J.; Brett, M. J.; Balland, V.; Limoges, B. *Langmuir* **2012**, *28* (39), 14065–14072.

(63)   Kasik, I.; Mrazek, J.; Podrazky, O.; Seidl, M.; Aubrecht, J.; Tobiska, P.; Pospisilova, M.; Matejec, V.; Kovacs, B.; Markovics, A.; Szili, M. *Sens. Actuators B Chem.* **2009**, *139* (1), 139–142.

(64)   Chourou, M. L.; Fukami, K.; Sakka, T.; Ogata, Y. H. *Phys. Status Solidi C* **2011**, *8* (6), 1783–1786.

(65)   Sakai, N.; Fujiwara, Y.; Arai, M.; Yu, K.; Tatsuma, T. *J. Electroanal. Chem.* **2009**, *628* (1-2), 7–15.

(66)   Murray, W. A.; Barnes, W. L. *Adv. Mater.* **2007**, *19* (22), 3771–3782.

(67)   Conrad, J. R.; Radtke, J. L.; Dodd, R. A.; Worzala, F. J.; Tran, N. C. *J. Appl. Phys.* **1987**, *62* (11), 4591–4596.

(68)   Yan, H.; Park, S. H.; Finkelstein, G.; Reif, J. H.; LaBean, T. H. *Science* **2003**, *301* (5641), 1882–1884.

(69)   Zhang, M.; Fang, S.; Zakhidov, A. A.; Lee, S. B.; Aliev, A. E.; Williams, C. D.; Atkinson, K. R.; Baughman, R. H. *Science* **2005**, *309* (5738), 1215–1219.

Chapter 4

Highly birefringent Indium Tin Oxide thin films grown by Plasma Assisted Glancing Angle Deposition for advanced labeling applications

4.1 Introduction

Indium tin oxide (ITO) thin films are widely used as transparent conductive coatings for many opto-electronic applications such as displays, solar cells or organic light emitting diodes, among others[1]. Due to its high transparency in the visible, ITO has also found other potential applications as infrared-reflecting films, defrosting or antistatic films or, in the form of multilayers with thickness modulated refraction index, for anti-reflective films or Bragg photonic crystals.[2–5] The potential of ITO films for all these applications resides in the facile up-scaling of their synthesis by many procedures using wet (i.e., sol-gel, spray, dip-coating[6,7],) or dry,(i.e., vacuum and plasma) deposition methods, these latter including e-beam evaporation or magnetron sputtering.[8–11]

Birefringent materials, characterized by exhibiting different refraction indexes along their principal axes, have been studied in single crystal form for more than three centuries. At present, they have encountered many applications in different technological domains of advanced photonics as in liquid crystal displays (LCDs)[12], second harmonic generators, light modulators or waveplates[13–15]. Birefringence, can be induced in synthetic materials by several ways such as stress application during molding of plastics or by inducing anisotropy during their fabrication as in glass fibers[16].

Glancing Angle Deposition (GLAD) is a well stablished technique to engineer the microstructure of thin films, typically formed by tilted nanocolumns where, for a given material, the void volume and tilting angle are determined by the angle of deposition. The modulation of density in these films provides an useful tool to tune their refractive index. Moreover, the anisotropic arrangement of the nanocolumns in this type of thin films provides a means for the modulation of birefringence due to the difference in

density and refraction indices along a fast (n_f) and slow (n_s) axis directions. We will show in this work that a way to enhance the birefringence of GLAD thin films is by inducing the nanocolumn association along the direction perpendicular to the evaporated material flux during the film growth [17–21]. This association or *bundling* is inherent for many oxides or metals grown by GLAD.[22–24](REF) Tuning this effect by applying complex movements of the substrates during growth or the utilization of seeded substrates has been reported by different authors[17,18].(REF)

In chapter 3 has been reported that the assistance of the growth of ITO thin films with a plasma of oxygen during GLAD induces an enhancement in the nanocolumnar bundling[22] and a high anisotropy in the in-plane conductivity of the films. In this chapter we study the optical birefringence of these oxygen Plasma Assisted (PA-) GLAD ITO thin films and show that this procedure provides a straightforward way of generating a giant optical anisotropy. Besides determining the optical birefringence of these films, we have simulated their optical behavior and correlate it with the characteristics of the thin film microstructure. To our knowledge, the maximum birefringence obtained with traditional GLAD technique is 0.07 for TiO_2[17,20,25], which can be increased by complex sample rotations up to 0.16.[25] In this work we have succeeded in getting a giant birrefringence of 0.20, to our knowledge the highest value ever reported for GLAD thin films. As an additional output of this work, we have profited from this extraordinary high birefringence to develop an efficient procedure of optical encryption capable of reproducing for example fingerprints or microelectronic circuits and be used for advanced anti-counterfeiting applications [22,24,26].

.

4.2 Experimental set up.

Thin film preparation

ITO thin films have been prepared in an e-beam evaporator set-up previously described in previous works[2–5]. The design of the experimental set-up used for the plasma assisted GLAD was shown in Chapter 3. Herein, ITO thin films were deposited under two experimental conditions, in the absence of plasma and by assisting their growth with an oxygen plasma. The two types of thin films were prepared at the same deposition angle (α= 80º).

ITO was e-beam evaporated from pellets supplied by Kurt J. Lesker. (In_2O_3/SnO_2 90%/10% (w/w)) that were placed in a graphite crucible for e-beam bombardment. GLAD thin films were prepared on silicon wafers and quartz plates for FIB-SEM and optical characterization, respectively.

Thin film characterization

The microstructure of the films was characterized for the samples prepared on silicon wafers. Bundling and growing orientation were determined by a dual beam FIB/SEM (Focus ion beam/Scanning electron microscopy) system (Zeiss 1540 XB) supplied with Ga ions accelerated by a voltage of 30KV and 1 pA. The working distance was 4.9 mm. Normal view micrographs were obtained in a SE microscope HITACHI-S-5200 operated by at 2KV.

The optical response of the films was studied by optical spectral transmittance measurements with a beam impinging at normal and polar inclined incidences in the 250-800 nm range with a 1 nm monochromatic step. The monochromatic incident beam was collimated, and linearly polarized. Measurements with cross polarizers were taken in the wavelength range 400-700 nm. Azimuthal and Polar angular dependency of the UV.-vis

transmittance spectra were carried out with a Cary 100 instrument from Varian using a goniometer to rotate the sample at positive and negative angles (-60º to 60º) 60º around the Z, X and Y-axis defined in Figure 2 with polarizations of light, p (electric field of the light parallel to the plane of incidence) and s (perpendicular). These sample rotations are relevant with regard to orientation and distribution of nanocolumns. Figure 4.1 shows a scheme of a tilted nanocolumnar film and the description of the three rotations used for analysis: azimuthal rotation where the sample plane is maintained fixed and two polar rotations around the growing (x) and bundling (y) axis. The effect of these three rotations upon the optical response of the birefringence films were analyzed using two orthogonal light polarizations, s and p.
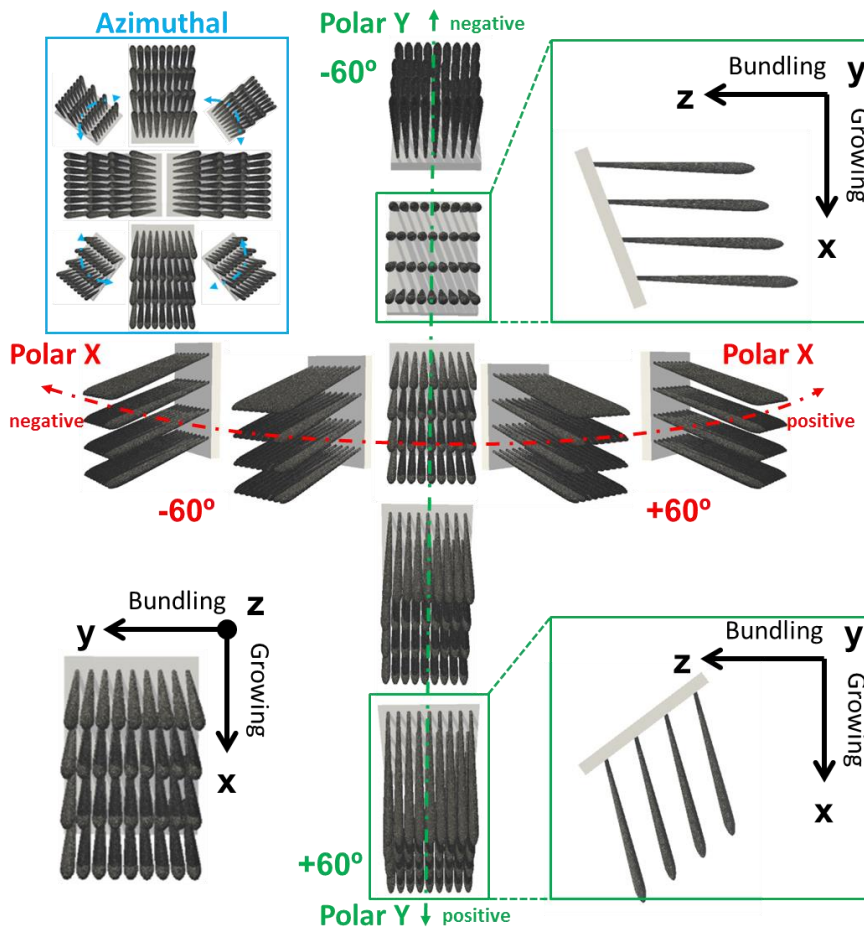
Figure 4.1. *Scheme of a tilted columnar film with a strong bundling association and sample rotations used for the experiments. By the azimuthal rotation (top left square) the sample plane is maintained fixed and the sample is turned around the z azis of the coordinate system (z). By the polar rotation the sample is turned around the axis x and y. Due to the anisotropy of the tilted nanocolumnar morphology, these two rotations are not equivalent. They correspond to a polar around the bundling axis or polar Y (green schemes) and polar around the growing direction or polar X (red scheme). These three different rotations were analyzed with two orthogonal light polarizations, s and p.*

Simulation of optical response towards polarized light

Simulation of the optical response of the ITO thin films was done using WVASE software by considering a uniaxial birefringent model consisting on two layers, one with a high refractive index characteristic of bulk ITO and a second layer with a low refractive index. The optical response of each layer was accounted for by two refractive indices, one in the direction of bundling (n_b) and the second along the incoming direction of the flux material during deposition (n_g). According to this description, each layer was considered as a uniaxial birefringent medium, with the optical axis oriented along the normal to the bundling direction.

In this model, birefringence was interpreted as a difference in the percentage of porosity between the bundling direction and its perpendicular. Porosity was simulated according to Bruggeman effective medium approximation, considering bulk ITO as compact media and the void fraction filled with air. To properly describe the experimental data, each layer was characterized by different absorption coefficients and dispersion values according to the Cauchy theory.

The optical axis (THETA angle in WVASE) was fixed to 60º off surface normal, coinciding with the experimental tilting of the nanocolumns in the films. To determinate the orientation of the projection of the optical axis on the samples surface we used a PHI angle of 90º (growing direction) and 0º (bundling direction)

Unfortunately, the spectra taken under polar rotation for the PA-GLAD films could not be simulated due to software restrictions unable to select the axis coordinates for polar rotations of anisotropic materials.

Fingerprint encoding.

A fingerprint was transferred to a glass substrate by using ink. Then a PA-GLAD layer of ITO was deposited and the sample was immersed in ethanol for 20 min to dissolve the ink and release the ITO thin film deposited on it. As a result, the areas previously covered with ink had no thin film material deposited, while the others remain intact.

ITO micropattern by Photolithography.

Micropatterning by photolithography was carried out in a clean room by spin coating (4,000 rpm/min, acceleration of 6,000 rpm/s² during 60 s) the photoresin 51813 onto PA-GLAD ITO thin films. The samples were annealed during 2 minutes at 115^0C in air and then exposed during 6.5 seconds to UV light (λ=250nm) using a previously aligned mask. The non UV-exposed resin was then removed by immersing the samples in the developer MF319 during 35 seconds and then rinsing with water. Finally, the non-covered regions of the samples were etched in a solution of H_2O:HCl (1:1) during 1.30 min. The resin rests were cleaned with acetone

4.3 Results and discussion.

### 4.3.1 Microstructure of GLAD and PA-GLAD thin films

In the chapter 3 has been demonstrated that the microstructure of GLAD thin films can be modified by assisting their growth with a plasma. Under these conditions it occurs the aggregation or budnling of the nanocolumns in the direction perpendicular to the material flux. Concretely, under oxygen plasma conditions, ITO thin films present an outstanding anisotropic

microstructure where bundling association is enhanced in comparison with traditional GLAD ITO thin films.

Cross section FIB micrographs of GLAD and PA-GLAD ITO thin films are presented in Figure 4.2 a)-d). Both samples were imaged with SEM, (GLAD (a,c) and PA-GLAD (b,d)) for two different orientations to better visualize the differences between growing (a,b) and bundling (c,d) directions. For the GLAD case (a, c), the intercolumnar distances are small and very similar for the two orientations. By contrast, the PA-GLAD anisotropic samples present a much higher intercolumnar distance along the growing axis (b) than along the bundling direction (d). The micrograph taken along the growing direction (Figure 4.2 b) shows a well-defined tilted nanocolumnar morphology with large intercolumnar distances of around 30-40 nm, while images along the bundling direction shows a continuous material in the form of a "wall".

Figures 4.2 e-h) show surface SEM views (e,f) and AFM topography images (g,h) of both samples. The topography of the GLAD sample (e) appears as a random granular distribution over the surface. This topography corresponds to the tips of the independent nanocolumns characteristic of the isotropic case. The bundling and growing directions are displayed in the figure along the (x) and (y) lines. The linear profiles along these two directions extracted from the AFM images depict a very similar contour for the GLAD case. By contrast, the topography of the PA-GLAD sample presents a granular appearance highly elongated along the bundling direction. Consequently, the line profile along the bundling direction depicts very broad features separated around 40 nm, in good agreement with the observations by SEM.
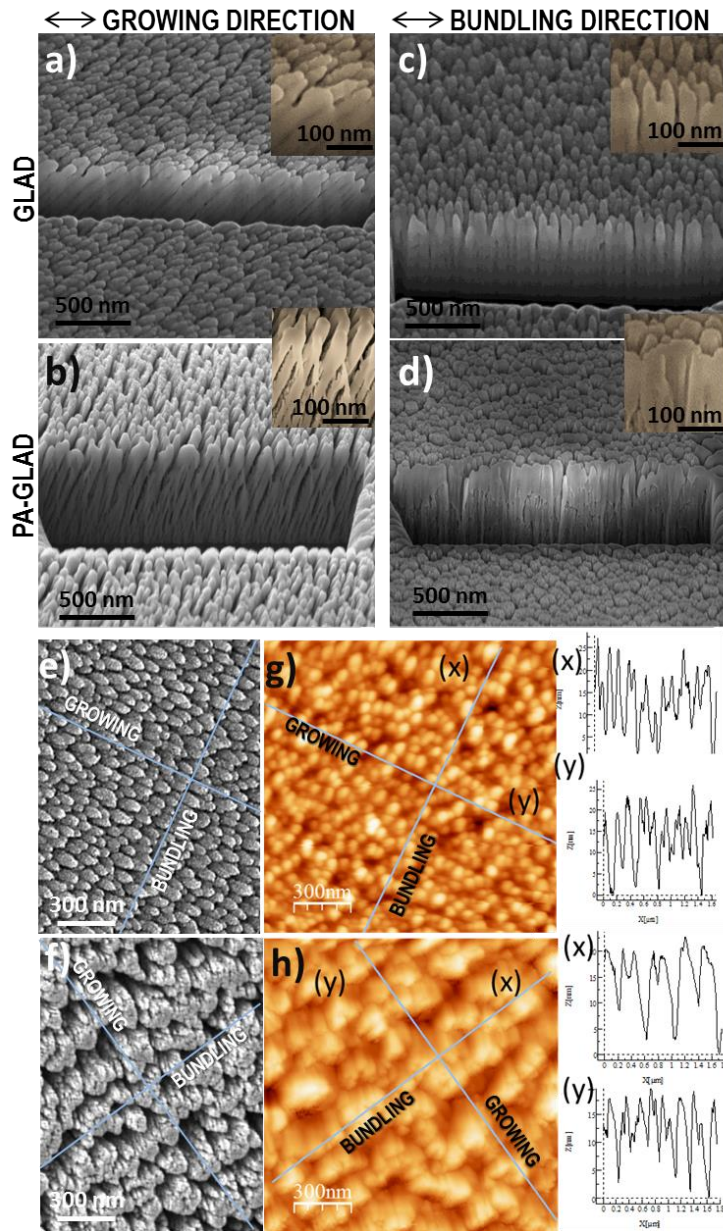
Figure 4.2. *Cross section SEM micrographs obtained by FIB for GLAD (isotropic, a,c) and PA-GLAD (anisotropic, b,d) ITO thin films. Both samples were analyzed under two perpendicular orientations along the growing (a, b) and bundling (c, d) directions. Top view SEM micrographs of GLAD (e) and PA-GLAD ITO (f). AFM images of the ITO thin film surfaces of GLAD (g) PA-GLAD (h). Right) Line profiles measured for these samples along a bundling(x) growing direction(y)*

127

4.3.2 Birrefringence of PA-GLAD thin films

In chapter 3 we showed that the bundling anisotropy obtained in oxygen PA-GLAD samples is responsible for an in-plane anisotropic conductivity. It is likely that bundling aggregation of nanocolumns also affects the optical properties of the sample.

Figure. 4.3 shows the optical transmittance spectra recorded at different azimuthal orientations of the GLAD and PA-GLAD ITO samples with respect to the polarization plane of light. The transmittance of GLAD ITO thin film (top) is independent on the polarization of light, a behavior that is typical for isotropic thin films. However, the structurally anisotropic PA-GLAD thin film (bottom) depicts different absorption spectra according to its azimuthal orientation. A lower/higher transmittance was measured when the polarized light was aligned along the growing/bundling directions. This behavior is consistent with the microstructural anisotropy observed in Figure 4.2 and can be accounted for by the following terms: when the bundling direction is aligned/misaligned with respect to the polarization plane of light, the effective refractive index and consequently the dispersion coefficient have higher/lower values, a feature that leads to an decrease/increase in the transmittance at low wavelengths.
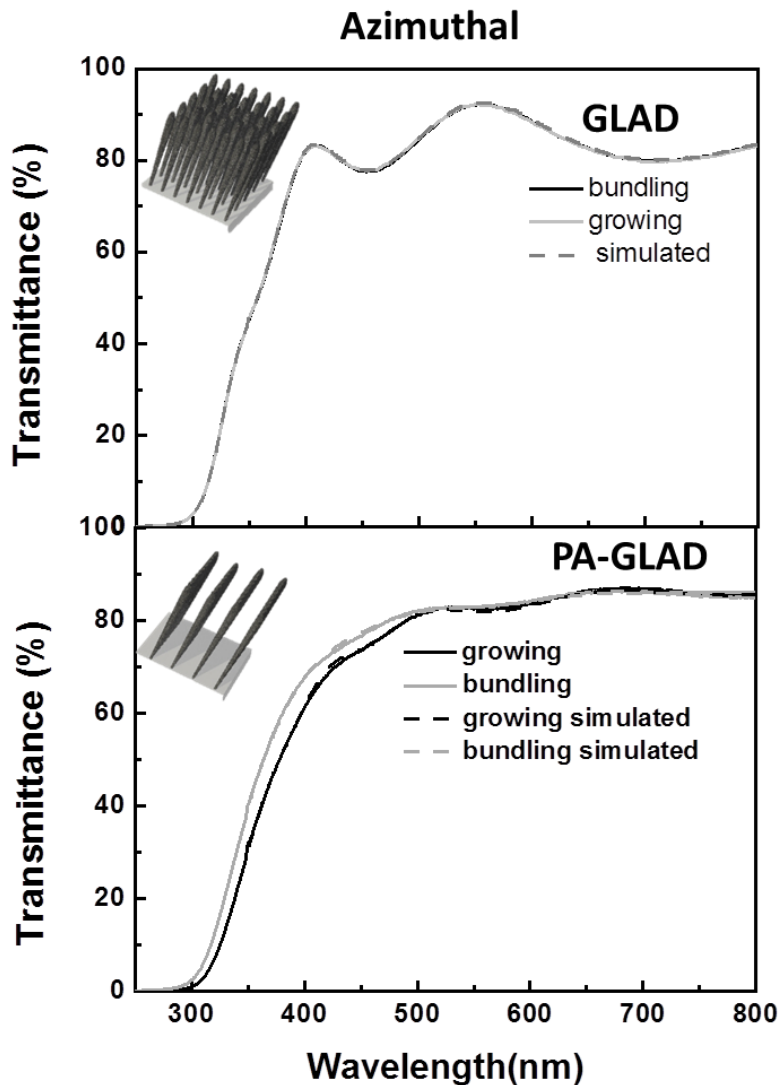
Figure 4.3. *Transmittance spectra recorded with polarized light while azimuthally rotating the GLAD (top) and the PA-GLAD ITO (bottom) thin films (full lines). Simulation of experimental spectra using the WASE software (dash lines)*

To understand the optical properties of GLAD and PA-GLAD thin films we proceed to the simulation of experimental spectra using the WASE software (see Experimental Section). The simulated transmittance spectra of

the azimuthally rotated GLAD and PA-GLAD films are shown in Figure 2 a) and b), respectively. The good agreement between the experimental and simulated curves proves the reliability of the assumptions of the optical model.

Table 4.1 shows the refraction indices values deduced from this analysis along the fast and slow axis, the difference between them (birefringence) and the porosities estimated along the bundling and growing directions. It is apparent from this table that while the GLAD sample presents an isotropic behavior with a porosity of 27% (calculated with respect to the bulk ITO), the PA-GLAD sample is anisotropic and presents a birefringence of 0.2 (λ=550 nm) and porosities along bundling and growing axes of 41% and 63%, respectively. To our knowledge, this is by far the highest birefringence obtained for metal oxide GLAD thin films at fixed angles[17] or by means of the SBD[27] technique, where maximum birefringence values of Δn=0.08 for ITO, or 0.16 for TiO_2 have been reported.

	n (Slow index) bundling direction	n (fast index) Growing direction	Δn	Bundling porosity (%)	Growing porosity (%)
PA-GLAD	1,68	1,48	0,2	41	63
GLAD	1,79	1,79	0	27	27

4.3.3 Optical anisotropy by rotating along polar angles

The alignment of the nanocolumns with respect to the polarization plane of light is expected to affect the thin film optical properties when rotating around the polar axis such as explained in Figure 4.1 Moreover, the tilted and aggregated nanocolumnar structure opens the way to anisotropic

optical responses when rotating along the polar axis, such as we have shown in previous works[22].

The transmittance spectra with polarized light of the GLAD thin films rotated around the polar axis X and Y depict an almost isotropic behavior and very little change in transmittance. Only a little difference in transmittance is found for p/s polarizations, an effect generally observed for any interface between two materials of different refraction index, even for the fused silica/ air interface such as showed Figure 4.3
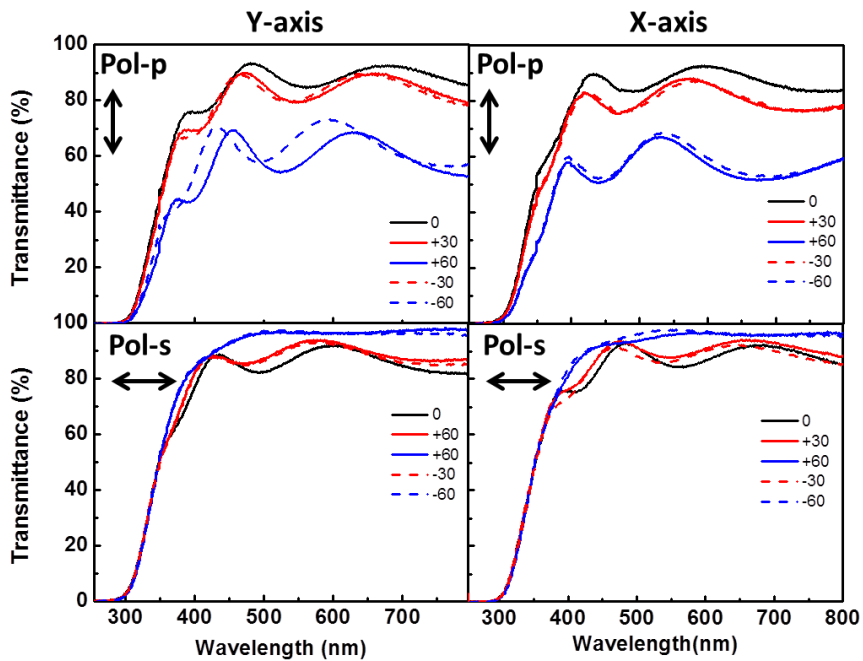
Figure 4. 3 *"p" and "s" polarized transmittance spectra for X and Y- polar rotations of GLAD ITO sample. The polar rotation was performed for positive and negative angles from -60º to 60º.*

Polar rotation of PA-GLAD ITO thin films leads to substantial changes in transmittance. The samples present an isotropic behavior when using either "p" or "s" polarized light and were rotated around the X-axis, showing similar transmittance values for negative and positive polar rotation angles such as shown in Figure 4.4. By contrast, these films present an anisotropic angular behavior when rotated around the Y-axis (c.f.Figure 4.4 a,c In this case, transmittance of "p" polarized light (a) is significantly different for positive and negative rotations. These differences are even higher for "s" polarized light (d). This distinct behavior can be related with the tilted alignment of the columns and the birefringence associated to the *bundling* both contributing to induce different refractive indices when the nanocolumns are aligned along the incoming direction of light or in another direction. For-30º polar rotation around Y-Axis, the polarization plane of light coincides with the tilting direction of nanocolumns in the PA-GLAD (scheme in Figure 4.1). Meanwhile, the rotation around X-Axis yields similar spectra for positive and negative angles, and therefore do not produce any difference for positive and negative angles. The spectra at -60º to 60º agree with the alignment and misalignment of the tilted nanocolumns for X and Y polar rotations.
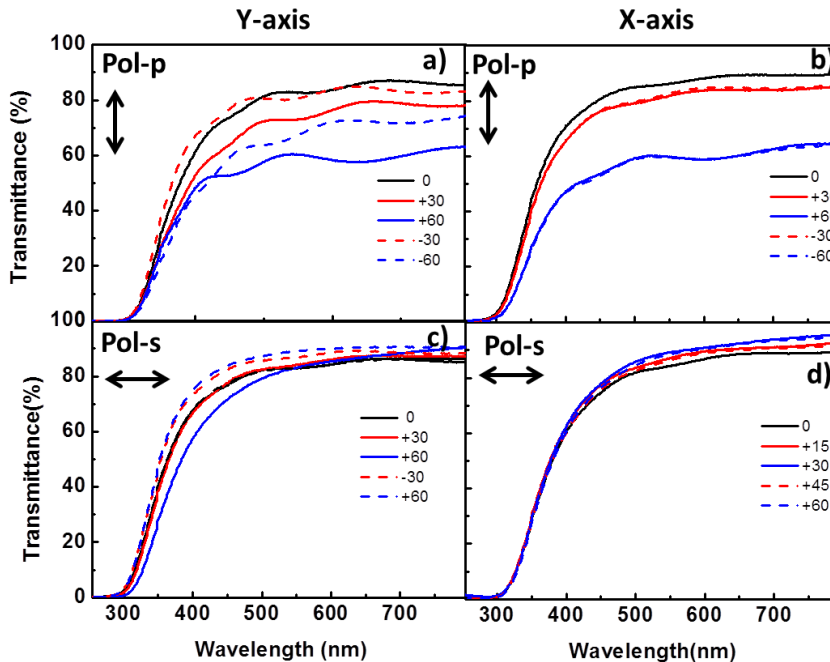
Figure 4.4. "p" and "s" polarized transmittance spectra for X and Y- polar rotations of PA-GLAD ITO sample. The polar rotation was performed for positive and negative angles from -60º to 60º.

4.3.4 PA-GLAD thin films as retarders

The giant birefringence of the anisotropic PA-GLAD ITO thin films can be directly visualized using two linear polarizers. When a birefringent sample is located in between two crossed polarizers, the outcoming light depends on the azimuthal orientation of the sample. Figure 4.5 shows that for GLAD (a) there is no light transmission regardless of the azimuthal orientation of the sample, while azimuthally rotating the PA-GLAD (b) sample light transmission occurs for certain orientations and reaches a maximum intensity when the bundling/growing directions form an angle of

45º with the polarization plane of light (see Figure 4.5 b). This effect can be visually observed in the photographs reported in Figure 4.5 e and f).

This behavior is typical of waveplates, an optical device characterized for introducing a phase shift between the two polarization components of a light wave and occurs when the polarized light forms a certain angle with respect to the slow or fast axes, with a maximum phase shift at 45º. This effect is known as retardation and responds to the equation

$$\Gamma(\lambda_0) = \frac{2\Pi \ \Delta n(\lambda_0) \ t}{\lambda_0} \quad (1)$$

with $\Delta n(\lambda_0)$ the birefringence for a given wavelength, t the thickness of the film, and λ_0 the wavelength of light in vacuum. From this equation it is apparent that GLAD sample ($\Delta n \approx 0$) would not induce any retardation and therefore no light would be transmitted when it is located in between two crossed polarizers, regardless of its orientation. Meanwhile, the anisotropic PA-GLAD ITO sample presents a retardation of Γ (500nm) = 0.40Π, calculated from Equation (1).

In the previous experiments the thickness of the PA-GLAD sample was optimized to approach a quarter waveplate to maximize the light transmitted through the crossed polarizer setup (note that this is only true for a given wavelength due to the inverse dependence with λ see Equation 2) where a retardation around $\Pi/2$ can be found for a thickness of 550 nm. The plot of the retardation value as a function of the wavelength in Figure 4.5.b) shows that it effectively reaches the expected value of $\Pi/2$ at 440 nm, very close to the experimental λ of maximum transmittance (420 nm) (in the ideal case for the crossed polarizers setup, a transmission of ca. the 70% light ($\sqrt{2}/2$) would be obtained).

In agreement with this retarder behavior, the y-axis rotation to -30 degrees (perfect columnar alignment) enhances the overall transmission of light

whereas the rotation to +60 attenuates completely the transmission to zero. This behavior can be accounted for by considering that the birefringence of the PA-GLAD samples is induced by the bundling association of the tilted nanocolumns and that the alignment of the nanocolumns with the incoming light plane enhances this effect. When the nanocolumns are misaligned by +60º with respect of the polarization plane, the effective refractive index should be similar in the bundling and along the columns, showing almost no birefringence. The scheme in Figure 4.5 g) shows the three scenarios of columnar alignment with respect to the polarization plane of light at -30 degrees (left), at 0 degrees (middle) and misalignment at +60 degrees (right), where the different birefringence for the three cases can be visualized. The pictures of figure 3g illustrate this effect showing that the alignment of the nanocolumns at -30º permits the transmission of light through the crossed polarizers setup and allows to read very clearly the words CSIC. On the contrary, the misalignment of the columns at +60º does not permit the transmission of light. This situation is repeated every 180 degrees, so that the spectra at -30º/+60º coincide with those recorded at +150º/240º as it is shown in Figure 3c).
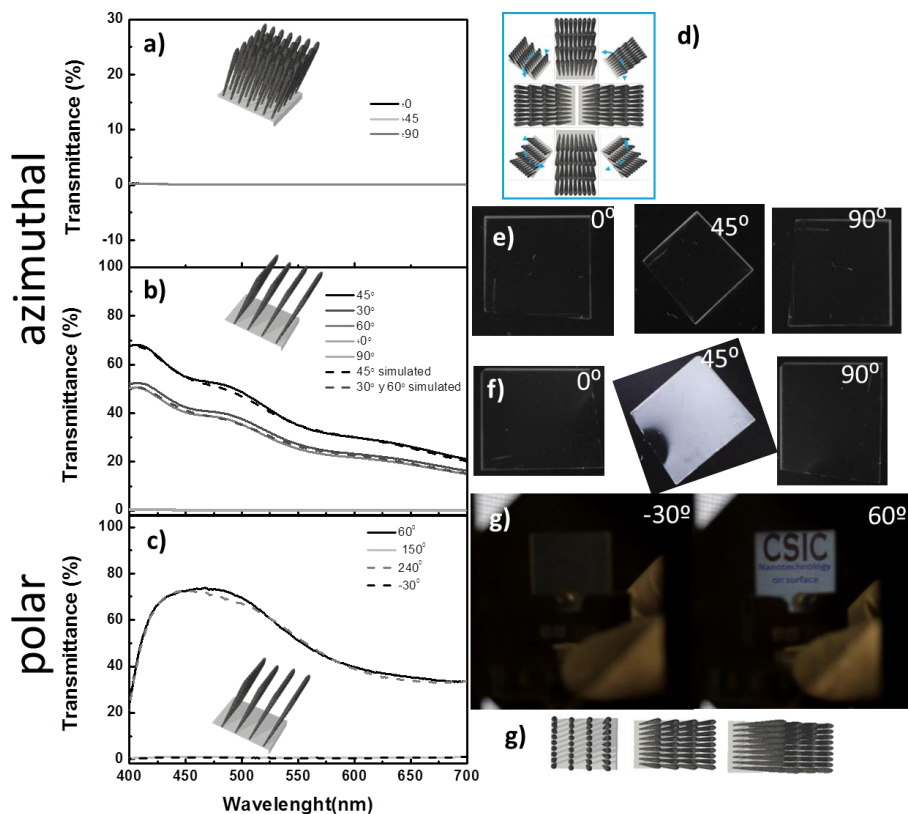
Figure 3. *Crossed polarizers transmittance spectra for azimuthal rotation of GLAD(a) and PA-GLAD thin films(b) and images taken for these azimuthal orientations (e) and (f). Azimuthal rotation scheme (d). Crossed polarizers transmittance spectra for Y- polar rotation of PA-GLAD thin films for a fixed azimuthal orientation of 45°. For Y-axis polar rotation, transmittance values are close to 0 for 60° and transmittance values are close 70 for -30°. These mimimum or maximum of transmittance coincide when the nanocolums are totally aligned or misaligned respect to the polarization plane of light(g). This situation is repeated every 180°, so that the spectra at -30°/+60° coincide with those at +150°/240°.*

4.3.5 Optical encoding

The giant birefringent of PA-GLAD ITO thin films can be used to develop optical encoding procedures compatible with the use of masks[22,24]. A

first possibility consists of visualizing a given pattern sample by examining it through cross polarizers. An example of this possibility is shown in Figure 4.6 for finger print encoding. In this example a fingerprint is printed with ink on a substrate followed by the PA-GLAD deposition of a ITO film and soaking of the sample in ethanol to remove the ink. Figure 4.6 a) and b) show that the fingerprint is not visible when the sample is placed between two crossed polarizers at 0º of azimuthal orientation (a) but it is clearly visible when the sample is placed between two crossed polarizers at 45º of azimuthal orientation (b). In this situation there is a misalignment of bundling/growing direction to respect the polarized state The inset in Figure 4b) shows a representative SEM picture of the fingerprint patterned area.

Another strategy for encoding information using PA-GLAD thin films consists of using photolithography. Figures 4c,d-f illustrate this possibility for an engraved micro-electronic circuits. The left photograph c), taken with linearly polarized light (similar pictures where obtained with natural light), show no hint of micro-pattern. By contrast, when the picture was taken through crossed polarizers, the patterned areas covered with the PA-GLAD thin films were bright while the others remain dark (d).Both situation were obtained when the sample was at 45º of azimuthal rotation The pictures in c) and d) show a zone with a defect (encircled in red), which is visible in both images. The inset in d) shows a SEM picture of a zone with portions free (left) or covered (right) by the ITO thin film. The photoligraphic patterns demonstrated that the PA-GLAD thin films are fully compatible with the use of masks and the patterns can be easily controlled to the scale of microns or below.
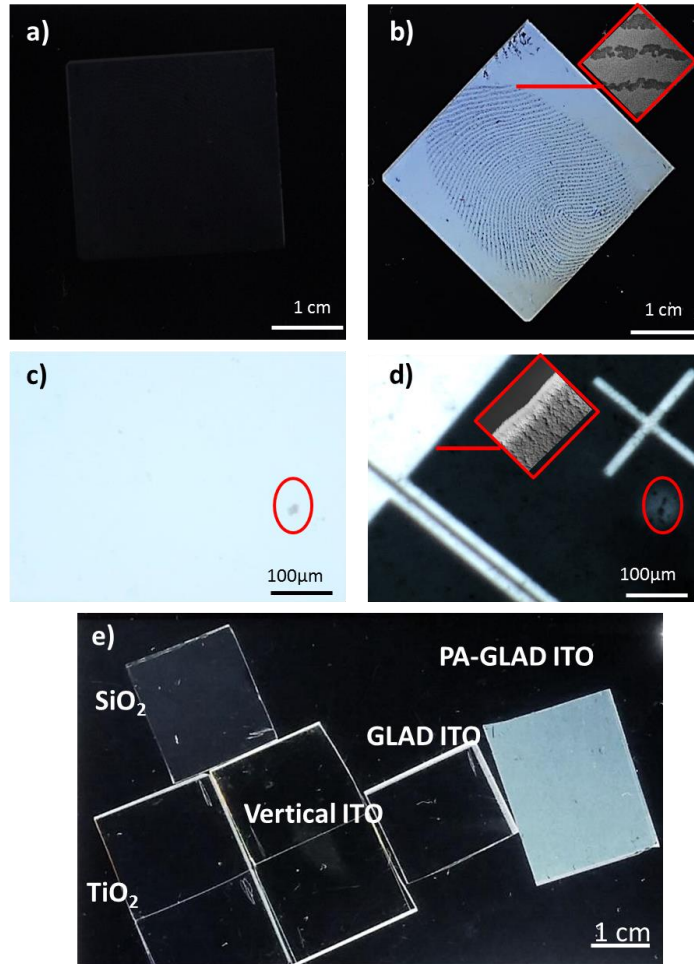
Figure.4.6 *a) and b) Fingerprint encoding on PA-GLAD ITO thin films. The finger print is not visible for the sample oriented at 0º (azimuthal orientation) with respect to the polarization lane, but it is visualized when examined through two crossed polarizers at a azimuthal orientation of 45º (b). The inset in d) shows a representative SEM picture of the fingerprint patterned area (c,d) Micro-patterns encoded on PA-GLAD ITO films by photolithography when they are examined by illumination with linearly polarized light(c) and when are examined through two crossed polarizers(d)) at 45º of azimuthal orientation . (Rounded in red) selected rea defect showing that it is visible in both images. Images taken for PA-GLAD ITO, GLAD ITO and comparison with SiO$_2$,TiO$_2$ thin films prepared by traditional GLAD at 80º when are examined through two crossed polarizers (e).*

The giant birefringence ($\Delta n = 0.2$) of the PA-GLAD thin films sustains their behavior as quarter waveplates if their thickness is adjusted to ca. 500 nm. To make apparent their high birefringence, the optical response of PA-GLAD ITO films was compared with a set of samples prepared by traditional GLAD at 80º of ITO, TiO_2 and SiO_2, as well as vertical columns of ITO obtained by rotating samples during deposition (all the samples have a similar thickness of around 500 nm). It is quite clear in the pictures in Figure 4.6 e), taken with the samples located in between crossed polarizers at 45º, that the anisotropic PA-GLAD ITO film is the only sample which transmits a high intensity of light. Although a detailed study of the birefringence obtained for different materials prepared by traditional GLAD is out of the scope of this work[21,23], the comparison shown in Figure 4e) further confirms that the Plasma Assisted GLAD is a very efficient technique to enhance the birefringence of GLAD thin films.

it

4.4 Conclusions

In this work we have developed a methodology to grow highly anisotropic and birefringent ITO thin films by assisting the deposition with oxygen plasma. Besides its relative simplicity, the method is quite reliable and scalable to large areas. The films present a highly anisotropic structure composed by tilted columns with very different columnar separation along the bundling and growing directions. Simulating the optical response of the samples with polarized light and azimuthal rotation with the software WVASE has evidenced a complex birefringent behavior due to the bundling aggregation of nanocolumns. The refractive indexes deduced by modelling had values of 1.48 and 1.68 along the growing and bundling directions, respectively. The resulting birefringence of 0.2 is the highest obtained by GLAD of metallic oxides. In addition, the nanocolumnar tilting orientation and bundling association of nanocolumns give rise to a complex birefringent response when turning the samples around both their polar and azimuthal axis, specially when the rotation modifies the orientation of the nanocolumns with respect to the polarization plane of light (i.e., around the y-AXIS).

The deposition process turned out to be fully compatible with the use of masks or photolitographyc techniques and permits the direct fabrication of highly dichroic patterns. This combined methodology opens a new methodology for encryption where the patterned code would only be readable with two polarizers oriented according to a correct geometrical arrangement.

.

REFERENCES

(1)   Granqvist, C. G.; Hultåker, A. *Thin Solid Films* **2002**, *411* (1), 1–5.

(2)   Schubert, M. F.; Kim, J. K.; Chhajed, S.; Schubert, E. F. Ellison, M. J., Ed.; 2007; pp 667403–667403 – 7.

(3)   Kim, J. K.; Chhajed, S.; Schubert, M. F.; Schubert, E. F.; Fischer, A. J.; Crawford, M. H.; Cho, J.; Kim, H.; Sone, C. *Adv. Mater.* **2008**, *20* (4), 801–804.

(4)   Poxson, D. J.; Kuo, M.-L.; Mont, F. W.; Kim, Y.-S.; Yan, X.; Welser, R. E.; Sood, A. K.; Cho, J.; Lin, S.-Y.; Schubert, E. F. *MRS Bull.* **2011**, *36* (06), 434–438.

(5)   Yan, X.; Mont, F. W.; Poxson, D. J.; Cho, J.; Schubert, E. F.; Kim, M.-H.; Sone, C. *J. Appl. Phys.* **2011**, *109* (10).

(6)   Sunde, T. O. L.; Garskaite, E.; Otter, B.; Fossheim, H. E.; Sæterli, R.; Holmestad, R.; Einarsrud, M.-A.; Grande, T. *J. Mater. Chem.* **2012**, *22* (31), 15740–15749.

(7)   Wang, T.; Radovanovic, P. V. *J. Phys. Chem. C* **2011**, *115* (2), 406–413.

(8)   Kim, S. I.; Jung, T. D.; Song, P. K. *Thin Solid Films* **2010**, *518* (11), 3085–3088.

(9)   Jung, Y. S.; Lee, S. S. *J. Cryst. Growth* **2003**, *259* (4), 343–351.

(10) Ikenoue, T.; Sakamoto, S.; Inui, Y. *Phys. Status Solidi C* **2014**, *11* (7-8), 1237–1239.

(11) Ali, H. M.; Mohamed, H. A.; Mohamed, S. H. *Eur. Phys. J. Appl. Phys.* **2005**, *31* (2), 87–93.

(12) Yang, C.-S.; Tang, T.-T.; Pan, R.-P.; Yu, P.; Pan, C.-L. *Appl. Phys. Lett.* **2014**, *104* (14).

(13) Kikuta, H.; Ohira, Y.; Iwata, K. *Appl. Opt.* **1997**, *36* (7), 1566–1572.

(14) Yasumaru, N.; Miyazaki, K.; Kiuchi, J. *Appl. Phys. A* **2003**, *76* (6), 983–985.

(15) Corrielli, G.; Crespi, A.; Geremia, R.; Ramponi, R.; Sansoni, L.; Santinelli, A.; Mataloni, P.; Sciarrino, F.; Osellame, R. *Nat. Commun.* **2014**, *5*.

(16) Ando, S.; Sawada, T.; Inoue, Y. *Electron. Lett.* **1993**, *29* (24), 2143.

(17) Hawkeye, M. M.; Taschuk, M. T.; Brett, M. J. *Glancing angle deposition of thin films: engineering the nanoscale*; 2014.

(18) Harris, K. D.; van Popta, A. C.; Sit, J. C.; Broer, D. J.; Brett, M. J. *Adv. Funct. Mater.* **2008**, *18* (15), 2147–2153.

(19) Rochon, P.; Gosselin, J.; Natansohn, A.; Xie, S. *Appl. Phys. Lett.* **1992**, *60* (1), 4–5.

(20) Van Popta, A. C.; Cheng, J.; Sit, J. C.; Brett, M. J. *J. Appl. Phys.* **2007**, *102* (1).

(21) González-García, L.; Parra-Barranco, J.; Sánchez-Valencia, J. R.; Barranco, A.; Borrás, A.; González-Elipe, A. R.; García-Gutiérrez, M.-C.; Hernández, J. J.; Rueda, D. R.; Ezquerra, T. A. *Nanotechnology* **2012**, *23* (20).

(22)   Gonzalez-García, L.; Parra-Barranco, J.; Sanchez-Valencia, J. R.; Ferrer, J.; Garcia-Gutierrez, M.-C.; Barranco, A.; Gonzalez-Elipe, A. R. *Adv. Funct. Mater.* **2013**, *23* (13), 1655–1663.

(23)   Sanchez-Valencia, J. R.; Toudert, J.; Borras, A.; Barranco, A.; Lahoz, R.; de la Fuente, G. F.; Frutos, F.; Gonzalez-Elipe, A. R. *Adv. Mater.* **2011**, *23* (7), 848–853.

(24)   Parra-Barranco, J.; Oliva-Ramirez, M.; Gonzalez-Garcia, L.; Alcaire, M.; Macias-Montero, M.; Borras, A.; Frutos, F.; Gonzalez-Elipe, A. R.; Barranco, A. *ACS Appl. Mater. Interfaces* **2014**, *6* (15), 11924–11931.

(25)   Hodgkinson, I.; Wu, Q. H.; Collett, S. *Appl. Opt.* **2001**, *40* (4), 452–457.

(26)   Drzaic, P. S. *J. Appl. Phys.* **1986**, *60* (6), 2142–2148.

(27)   Hodgkinson, I.; Wu, Q. hong. *Appl. Opt.* **1999**, *38* (16), 3621–3625.

Chapter 5

Bending induced self-organized switchable gratings on polymeric substrates

5.1. Introduction

After prolonged immersion in water the skin expands producing the universally experienced pruney fingers. Similar surface instabilities are ubiquitous in nature and arise whenever a stiff film coats a compliant substrate. The field of surface instabilities in engineered thin films is in continuous expansion since the pioneered publications by Whiteshides and co-workers on hierarchical surface patterning[1-3] inspiring a rich variety of applications such as optical gratings[2], nanofluidic manipulation,[4-6] controlled cell adhesion surfaces,[7] and others.[8,9] In addition, surface wrinkling is the basis of novel successful methodologies of thin film and coating properties characterization.[10-13]

Glancing angle deposition (GLAD) of evaporated layers is a well-established methodology for the fabrication of tilted oriented nanocolumnar thin films.[14-17] By this method the substrate surface is place at a glancing angle with respect to the evaporation source and this particular film microstructure is the result of shadowing effects during the film growth produced by the arriving of a vapor flux at a glancing angle ($\theta \geq 60°$) with respect to the substrate surface such as have been explained in Chapter 1.[14] In some materials like SiO_2, the tilted nanocolumns tend to aggregate along a direction perpendicular to the incoming vapor flux forming strongly anisotropic surfaces.[18] This process known as bundling[19] has been recently utilized for the fabrication of tunable dichroic optical structures.[20,21]

Herein we studied the process of self-structuring of transparent GLAD SiO_2 films deposited on PDMS when subjected to manual bending. The results demonstrate that the properties of the patterns generated by this extremely simply process are directly determined by the film nanostructure. Moreover, it is shown that the characteristics of this process differ from those reported for wrinkled surface structures and cracks patterns generated on PDMS by combining deposition/surface oxidation and uniaxial strains.[1-9] A thorough characterization of the system microstructure and its phenomenological optical behavior sustain the

ample possibilities open by the proposed methodology for the fabrication of foldable optical devices.

5.2 Experimental set up

For this work, GLAD SiO_2 and TiO_2 thin films were prepared by electron evaporation as reported elsewhere[21-23] at the glancing angles $\theta= 60º$, $70º$, $80º$, and $85º$. SiO_2 and TiO pellets were used as targets for the depositions of SiO_2 and TiO_2 thin films, respectively. The evaporations were carried out at a pressure of 10^{-4} torrs of oxygen to obtain stoichiometric films. A calibrated quartz crystal monitor was used to control the individual layer thicknesses for each type of films.

The temperature of the sample holder during the deposition of the SiO_2 film was measured to be only 2-4 degrees higher than room temperature. PDMS foils and Si(100) were used as substrates, the latter for the control of the evaporation process and thin film characteristics. The nanocolumnar films were studied without any additional treatment after deposition.The PDMS foils with a thickness of 1.5 mm were prepared by mixing the Sylgard 184 (DOW) two part silicon elastomer and degassing and curing the mixture at 80 ºC during 30 minutes. After this process, the foils were cut in pieces of 2 x 2 cm^2.

FESEM characterization was carried out with a Hitachi S4800 microscope. Planar views of thin films on Si(100) and PDMS were measured as deposited. The cross-sections of films on PDMS were measured after coating the films with a thin gold layer to reduce charging effects during the characterization.

The UV-Vis transmission of the films was measured with a Cary 100 spectrophotometer from Varian. Diffracted light pattern intensities were measured with a calibrated visible-light photometer PMMA2100 from Solar Light Co.

The curvature (κ) of the coated foils during the diffraction measurements is taken as the inverse of the radius of the circle that most closely approximates the curve in the position of the bending axis illuminated with the laser. The values were

calculated from pictures of the bent film sections in the sample holder during the measurements.

5.3. Results and discussion

5.3.1. Bending induce formation of parallel grooves.

In general, cracking of thin films is synonym of irreversible damage, delamination and/or device failure. Nevertheless, under certain well controlled conditions, a tensile stress applied to a film supported on a compliant substrate can induce the development of a regular pattern perpendicular to the resulting strain.[24,25] For example, patterns of cracks produced by uniaxial straining of plasma surface oxidized PDMS foils have been used for the fabrication of protein matrices[26] and nanofluidic channels.[27]

A simpler way of applying stress to a PDMS foil is by bending. We have found that when this elastomeric polymer coated with a relatively rigid silicon dioxide layer is bent, irregular cracks are formed to release the accumulated mechanical stress.

Figure S5.1 a-c in the Supporting Information (SI) shows a series of micrographs of PDMS foils bent after being coated with continuous SiO_2 thin films. These experiments have been conducted with SiO_2/PDMS systems fabricated by surface oxidation with an oxygen plasma[28] (cf. Figure S5.1a), plasma-enhanced chemical vapor deposition[29] (cf. Figure S5.1b) or electron evaporation of silica at normal incidence (cf. Figure S5.1c), respectively. In the three cases, the slight bending of the coated foils produce the formation of a series of irregular cracks whose number irreversibly increases with additional bending operations. This accumulated cracking is neither controllable nor reproducible and typically yields local delamination after a small number of bending events.

As it will be shown, bending a PDMS foil coated with a nanocolumnar SiO_2 thin film prepared by physical vapor deposition at glancing angles renders quite different results.

The room temperature GLAD deposition of SiO_2 on PDMS foils (hereafter called G-SiO_2/PDMS) yields anisotropic nanostructured thin films characterized by a tilted columnar microstructure as shown in Figure 5.1a. The figure shows as example the SEM images of a film deposited simultaneously on Si(100) and PDMS foil substrates. Apart from the charge effects that render difficult the observation of films on dielectric substrates such as PDMS by FESEM, the images demonstrate a similar nanocolumnar tilted arrangement in both cases.

The determined tilted angles of the nanocolumns are ~55º ±2º and ~53º ±2º for the film deposited on Si(100) and PDMS, respectively. Thus, it can be concluded that the PDMS substrate does not modify the properties of the glancing angle SiO_2 nanocolumnar thin films.

In the first chapter was explained that the nanocolumns tilting angle and porosity of oxide thin films deposited by GLAD increase gradually with the deposition angle while, simultaneously, the number of nanocolumns per unit area decreases.[17,23] Another characteristic microstructural effect sometimes encountered in this type of thin films is the preferential association of the nanocolumns in a direction perpendicular to the arrival flux of material.[19-21] This association is usually designed with the term bundling and it is known to enhance the surface anisotropy of the system. Clearly, in the G-SiO_2 thin film such bundling association of nanocolumns (see the example in Figure 5.1a) originates a strong film in-plane anisotropy.[17,19]
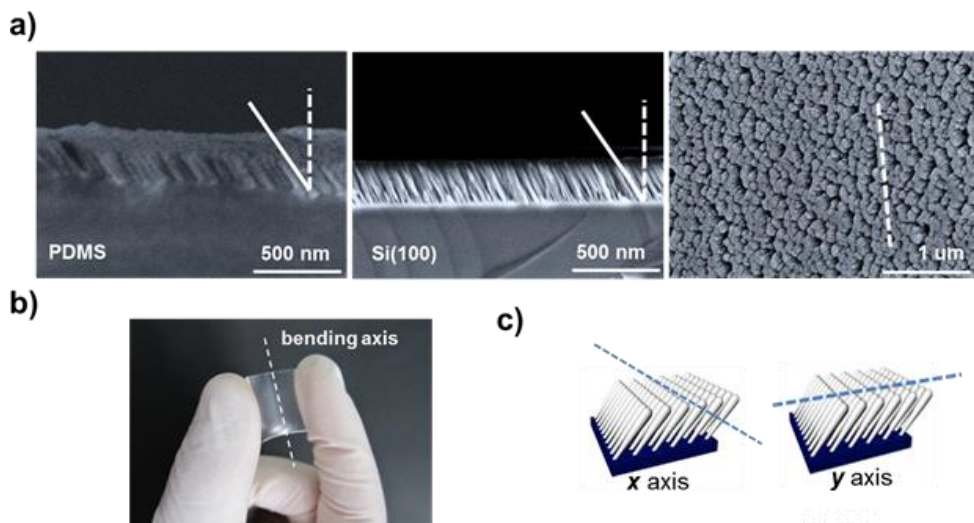
Figure 5.1. *Examples of tilted columnar G-SiO$_2$ films prepared by GLAD at 80º glancing incidence. a) Left and center: cross-sectional FESEM micrograph of films deposited on PDMS foil and Si(100) and right: FESEM planar view of the latter film showing the preferential column association or bundling along the direction marked by the dash line. The thicknesses of the films in the figures are ~250 nm. b) Picture showing the procedure required for structuring the surface of a PDMS foil coated with a G-SiO$_2$ thin film by simply bending the foil after deposition. c) The schemes show the two axis used for bending as defined with respect to the thin film anisotropic structure by taking the x axis along the nanocolumnar bundling direction.*

As shown in Figure 5.1 b, after thin film deposition, the G-SiO$_2$/PDMS foils were manually bent at curvatures $\kappa \ll 0.55$ cm^{-1} along the orthogonal *y* and *x* axis defined by the nanocolumnar growth and bundling directions respectively (see Figure 5.1c).

Figure 5.2 a shows that bending along the *x* axis a G85º-SiO$_2$/PDMS foil renders a set of parallel and homogeneously separated grooves that, from edge to edge, cover the whole film surface. These grooves, spaced by ~4 μm, result from a regular cracking of the deposited oxide and define a regular pattern parallel to the bending axis. This pattern remains unaltered after actuation on the film for more

149

than one thousand times (literally, as will be shown below). Bending the same foil along the **y** axis yields a similar pattern with a inter groove spacing of ~6 µm.
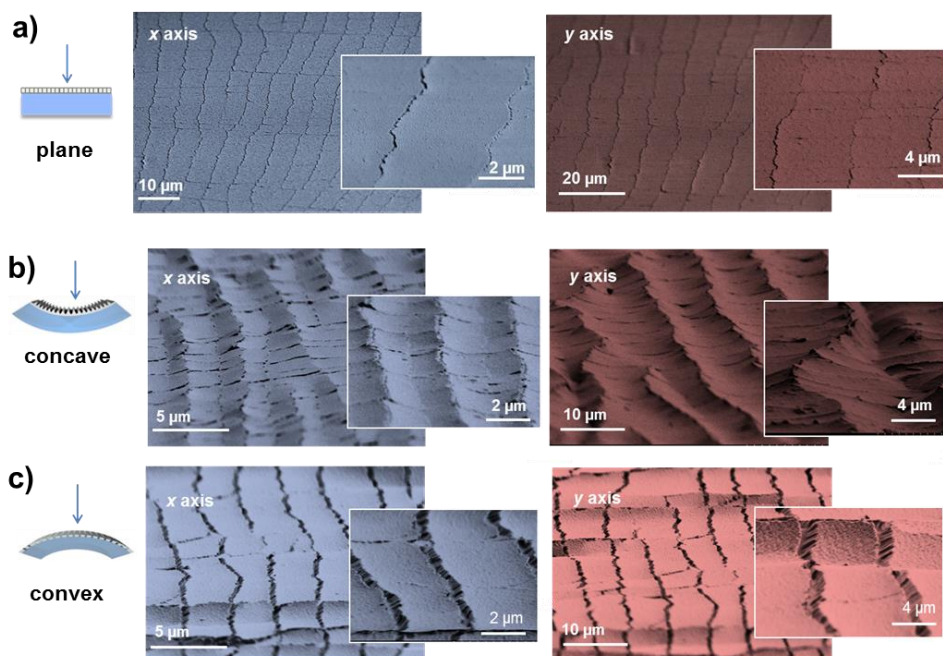
Figure 5.2. *a) FESEM micrographs of two G-SiO$_2$/PDMS flat surfaces after bending the coated foils along the x (left) and y (right) directions. b) FESEM micrographs of the films in a) while forming a concave surface during observation. c) FESEM micrographs of the films in a) while forming a convex surface during observation. The pictures and graphs in this figure correspond to ~300 nm thick G-85º-SiO$_2$ films.*

A set of G-SiO$_2$/PDMS foils with different oxide thicknesses have been prepared at different glancing angles of deposition to elucidate the relationship between thin film microstructure and surface patterning upon bending (see the examples gathered in Figure S5.2).

Figure 5.3 shows the experimental relationship between the groove spacing and the glancing angle of deposition by bending along the x and y axis. The groove spacing decreases linearly as the deposition angle increases, being the values corresponding to the y axis always higher than those corresponding to the x axis. Thus, a first conclusion of this analysis is that the inter-groove spacing can be greatly varied by just changing the deposition angle of the G-SiO$_2$ films.

Apart from this relationship between nanocolumnar structure and groove spacing, the experimental results also show that neither the film thickness nor the bending curvature had any appreciable influence on the pattern characteristics. We will come again to this point later in the text.

Further insight into the dynamics of the grooves upon successive bending was gained by keeping curved the G-SiO$_2$/PDMS foils during SEM observation. The micrographs in Figure 5.2 b taken for the film situated onto the concave side of the foil curved along the x or y bending axes show that the accumulated compressive stress releases through the formation of wrinkles consisting of a periodic distribution of valleys and ridges. This wrinkles arrangement is a direct transformation of the parallel groove pattern observed on the flat surfaces, with the wrinkling period and spacing coinciding with those of the initial cracks. By contrast, the normal view micrographs of the films placed on the convex side (Figure 5.2c) show the development of similarly spaced big grooves where the gap separating the cracked SiO$_2$ strips is larger than in the flat state. The checkered pattern partially observable in Figure 5.2b (right) is due to the additional parallel cracking line pattern perpendicular to the bending axis due to previous bending events.
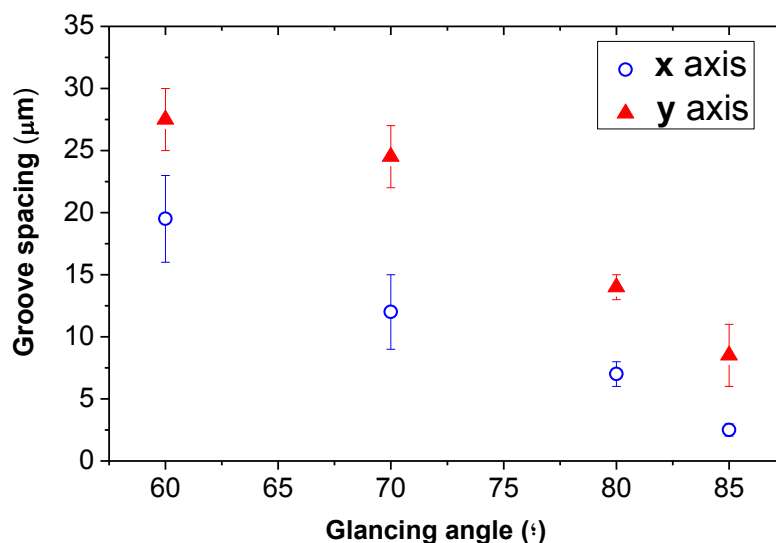
Figure 5.3. *Relationship between the experimental groove spacing values and the thin film nanostructure determined by the evaporation glancing angle for PDMS covered specimen bent along the x and y axes.*

5.3.2 Switchable light diffraction

A remarkable property of the groove structure generated by bending the G-SiO$_2$/PDMS surfaces is that they work as switchable optical gratings.

Figure 5.4a shows that the flat or bent foil covered with the G-SiO$_2$ film at the convex side was transparent. By contrast, when the foil is bent with the G-SiO$_2$ film at the concave side it behaves as a diffraction grating splitting the white light beam into its components. This phenomenon can be observed without using any optical set-up.
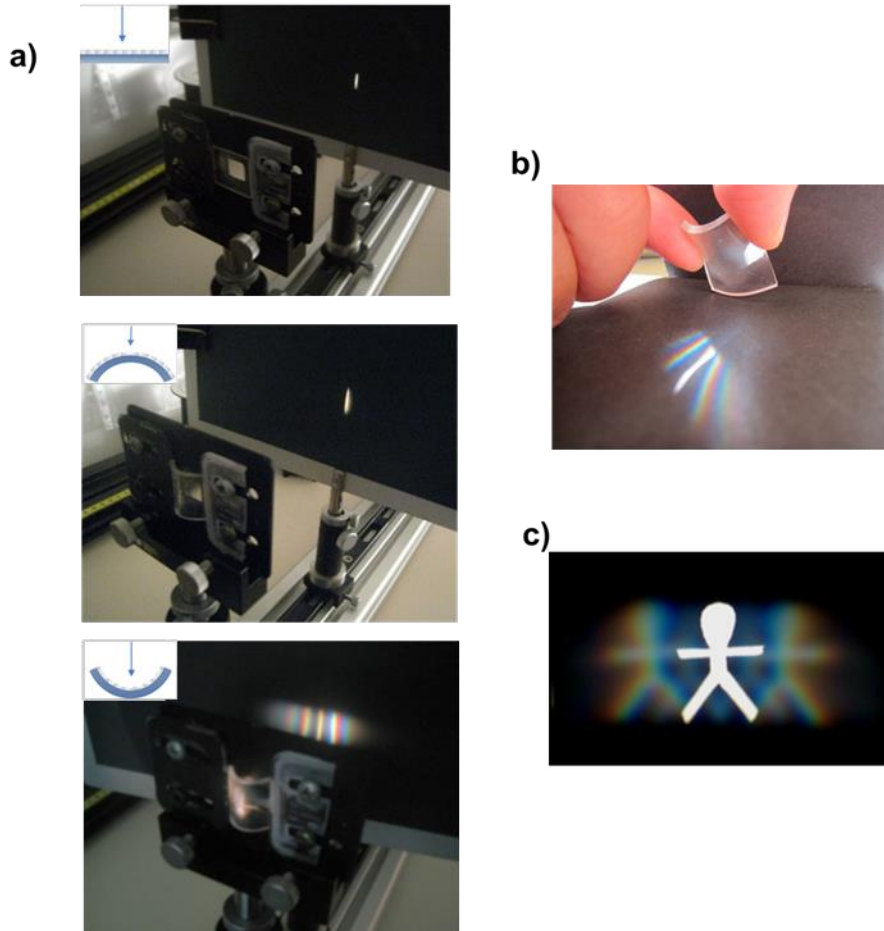
Figure 5.4. a) Pictures of a white light beam passing through a G-SiO2-PDMS foil with a regular groove pattern formed by bending. The light passing through this foil in a flat (left) and convex (center) configuration reaches the screen undisturbed. The light passing through the concave covered surface (right) is diffracted and forms a characteristic rainbow pattern onto the screen. b) Picture of a concave G-SiO2/PDMS foil diffracting a sunlight beam c) White light back-illuminated cut-out figure observed through a concave G-SiO2/PDMS foil showing a symmetric first order diffraction pattern at the two sides of the direct transmitted light.

Thus, Figure 5.4b shows the diffraction pattern of a beam of sunlight traversing the foil when falling on the concave surface. The diffraction performance of this system is further proved in Figure 5.4c showing the formation of a well-defined symmetric first order spectral image at both sides of an illuminated cut-out figure observed through the concave G-SiO$_2$/PDMS foil.

This transition from a transparent configuration (i.e., flat or convex surface) to a grating configuration was fully reversible and reproducible. The reversibility was tested by repeating the process more than one thousand times with the same foil (see next section).

To understand the origin of these diffraction effects we illuminated two concave surfaces with a 532 nm laser focused in a line oriented either along the *x* or *y* bending axes and measured the distance between the diffraction maxima and the relative intensity of the individual lines. The obtained results are gathered in Figure 5.5a.
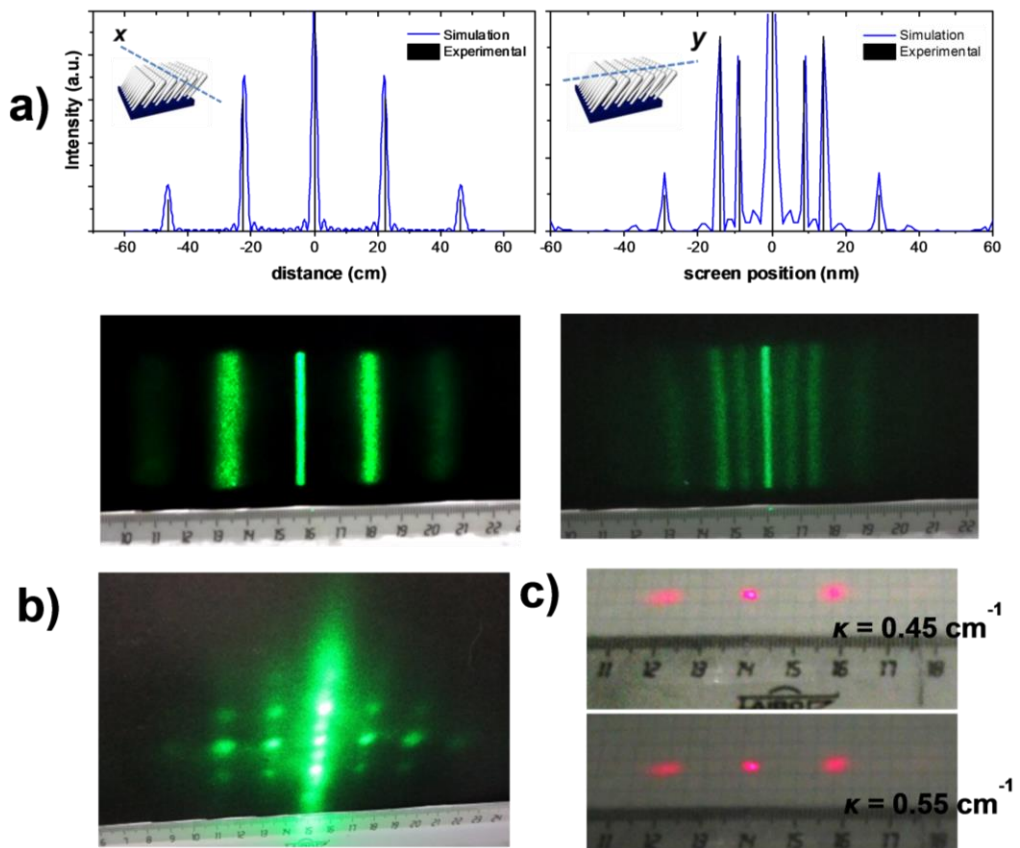
Figure 5.5. *a) Diffraction patterns corresponding two concave surfaces of the same G-SiO2/PDMS foil illuminated with a 532 nm laser focused along a line parallel to the x and y bending axis. The experimental and calculated Fraunhofer diffraction patterns for the two axes are also included in the figure. c) Diffraction of a 532 nm laser dot by a G-SiO2/PDMS foil with the oxide film covering the concave hemispherical surface which is bent by pressing the four corners simultaneously. c) First order diffraction pattern of a 635 nm laser measured by changing the curvature of the G-SiO2/PDMS foil bent along the x axis forming a concave surface. All the examples of this figure correspond to a ~300 nm thick G-85ºSiO2/PDMS foil. The distance between the samples and the screen was ~13 cm and the laser lateral spot size was ~2 mm.*

The experimental patterns can be directly simulated by assuming a Fraunhofer diffraction by the periodic undulation observed in the concave bent surfaces as shown in Figure 5.2b (see S5.3 for details about the calculations). The optical grating possibilities of the G-SiO$_2$/PDMS foils are further evidenced in Figure 5.5b showing the diffraction pattern obtained when the concave surface adopts a hemispherical shape by pressing simultaneously the four corners of the foil. In this case, the laser diffraction pattern is a combination of the single patterns obtained by edge bending along the **x** and **y** axis. A similar pattern was obtained when the foils were bent along an axis different to **x** or **y**. These evidences support that the **x** and **y** axes are determined by specific directions of the G-SiO$_2$ film nanostructure and not by the foil manipulation.

Equivalent experiments carried out with G-TiO$_2$/PDMS foils showed a similar decreasing trend of the crack spacing with the tilting angle (data not shown) than that reported in Figure 5.3 for the G-SiO$_2$/PDMS foils. However, in this system with nanocolumnar TiO$_2$ thin films no significant differences were found by bending along the **x** or **y** axis (see Figure S5.4). This different behavior can be related with that intrinsically the TiO$_2$ nanocolumnar GLAD thin films are in-plane isotropic due to the low tendency of these oxide films to develop bundles of nanocolumns specially at high glancing angles[17,23] This outcome clearly stresses the importance of the film nanostructure for the control of the micropatterning processes of PDMS when deposited on its surface.

Another outstanding characteristic of the light diffraction by the concave surfaces was that the diffraction patterns did not depend on the surface curvature but on the deposition angle of the films and, therefore, they were entirely controllable by the manufacturing process. We experimentally determined a minimal curvature κ = 0.55 cm^{-1} to observe the light diffraction. At higher curvatures (κ = 0.45 cm^{-1}) the diffraction pattern remained constant as shown in Figure 5.5c.

Another remarkable feature of the G-SiO$_2$/PDMS system is that the average crack spacing is independent of the thin film thickness. This was proved by verifying that identical micropatterns are obtained for thin films of ~50, 100, 300 and 600 nm when deposited at the same glancing angle. As reported above, in the

curse of these investigations it was also found that groove spacing was independent on the bending magnitude initially applied to the foil to produce the surface cracking. This behavior contrasts with the reported behavior of wrinkled PDMS surfaces where wrinkling-related diffraction effects are tightly dependent on the thickness of the stiff films coating the PDMS and on the magnitude of the experienced strain.[10-12, 30,31]

Other studies about cracking of thin films on compliant substrates also reveal that the average inter-crack distance is always inversely proportional to the strain.[10,24-26] It can be attributed the singular behavior of our system to the coupling between the PDMS surface wrinkling processes generally developed by this material to accommodate the bending induced stress and a tectonic-like behavior of the inter-crack $G-SiO_2$ (or $G-TiO_2$) regions. The collision behavior of these regions when bending would be determined by the deposited film and yield a specific distribution of valleys and ridges at a given periodicity which remains invariable at any curvature (Figure 2b). In this model the accommodation of the additional stress induced by increasing the curvature would produce an increase in the height of the ridges but not a modification of the inter-crack spacing.

5.3.3. Fabrication of optical patterns

Another remarkable optical effect of the $G-SiO_2$/PDMS foils usable for invisible labeling applications is the global loss of the foil transparency when they are properly bent. This blurring effect is a direct consequence of the diffraction of light along the whole visible spectrum studied in the previous section.

Figure 5.6a shows how a printed image appears blurred when observed thorough a bent foil with the $G-SiO_2$ film placed at the concave side. Since the regular groove pattern spreads over the entire bent surface, this effect can be observed through relatively large area foils as in the example of the figure. In addition, if only a region of the foil is bent, the flat region remains transparent as shown in Figure5.6b. The observed visual loss of transparency was less dependent

than the diffraction phenomena on the column microstructure and the specific orientation of the bending axis. This characteristic would facilitate the up-scaling of the process to coat large areas. Thus, large areas would perform similarly with respect to the light blurring even if the local microstructure (tilting angle and density) of the nanocolumnar film could slightly vary from a zone to the other due to slight differences in the glancing angle or the presence of any other inhomogeneity.

It is interesting to stress that the bending induced light diffraction and the related local blurring process are fully reversible effects. Figure 5.6c shows that the optical transmission of a G-SiO$_2$/PDMS in the range 250-800 nm remained invariable after 1000 bending events and how in all the cases the coated foils became transparent when they were brought back to their flat state.
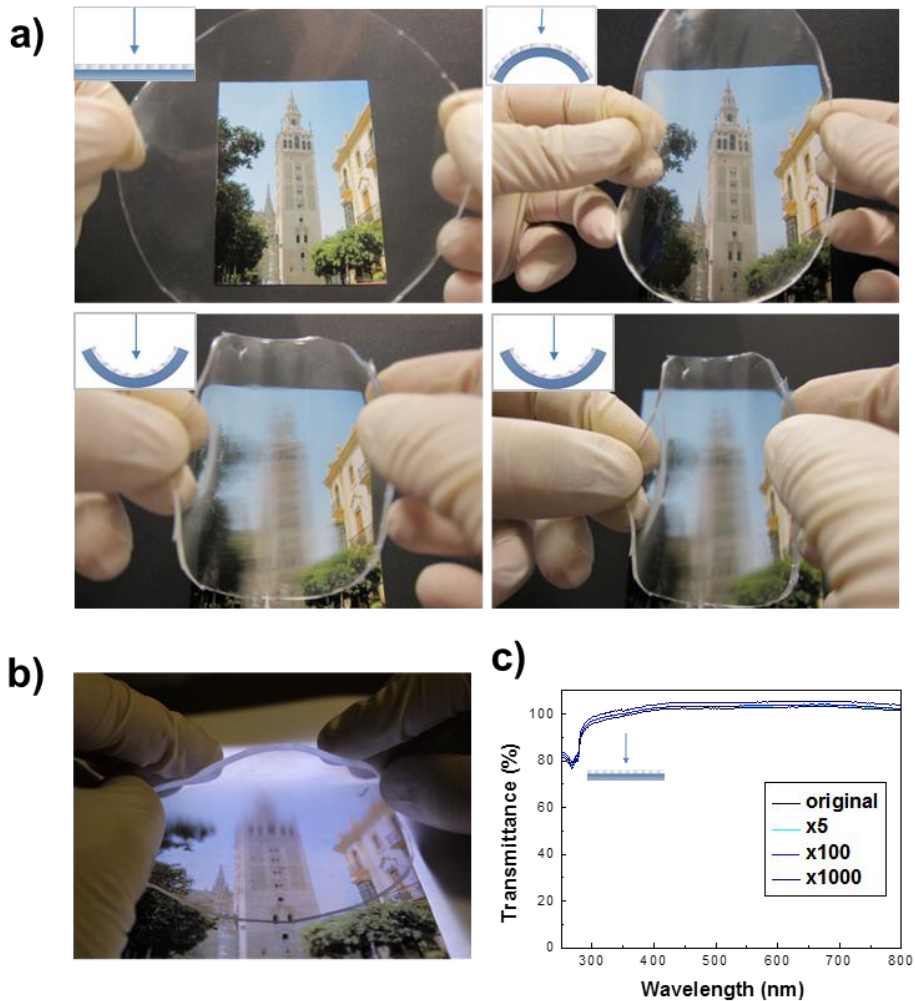
Figure 5.6. a) *Set of pictures demonstrating the loss of transparency of a G-SiO2/PDMS concave surface of a 15 cm diameter disk in comparison with the normal transparent behavior of the foil in flat and convex configurations. b) Picture showing that the loss of transparency is locally restricted to the bent zone whereas the flat region remains transparent. c) UV-Vis transmission spectra of a SiO2 thin film bent 5, 100 and 1000 times. All the examples of this figure correspond to a ~300 nm thick SiO2 film deposited at 85º of glancing angle on a PDMS foil.*

A straightforward application of the local optical diffusing effect is the development of invisible labels, i.e. motives that are invisible when the film is relaxed and visible by bending. Printed figures or patterns can be easily designed on

159

the surface of PDMS by depositing the nanocolumnar films using shadow masks. An example of this approach is presented in Figure 5.7 where each side of a PDMS foil has been coated with a G-SiO$_2$ film using different shadow masks.

The printed structures can be neatly seen by the naked eye on the surface of the bent foil and also by projecting on a screen with direct white light illumination as shown in the figure. Although the fabrication of patterns formed by local surface wrinkling after deposition or plasma oxidation of PDMS foils through shadow masks has been reported previously,[2,30-32] a clear advantage of our procedure is that it permits to pattern each side of the foil independently. In this way, two different labels can be extracted from a double side coated foil depending on the side forming a concave surface (Figure 7) when the surface is observed or illuminated. Furthermore, if the deposition of a G-SiO$_2$ film is carried out onto a curved substrate the structure appears either blurred or transparent when the foil is flat or curved, respectively (data not shown). All these procedures could be used to encrypt information on transparent foils that would be easily retrieved by mechanical actuation with no need of optical set-ups.
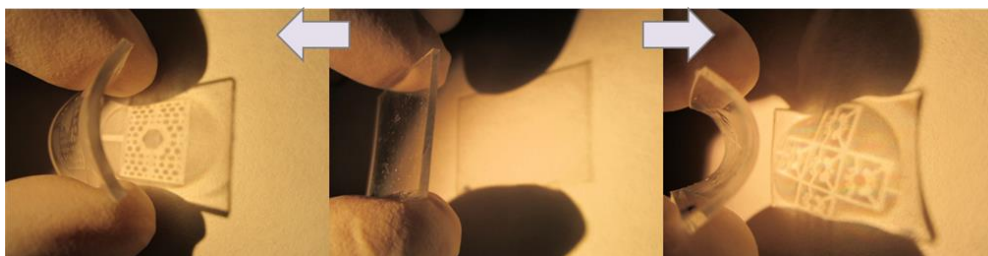
Figure 5.7.- *Pictures of a PDMS foil double-side deposited by using two different shadow masks. The projected light reveals the patterns printed onto the concave surface whereas the pattern in the opposite convex surface is invisible. All the examples of this figure correspond to a ~300 nm thick SiO2 film deposited at 85º of glancing angle on a PDMS foil.*

5.4 Conclusions

This work has demonstrated that reversible/switchable gratings can be obtained by bending flexible PDMS foils coated with nanocolumnar SiO_2 thin films prepared by GLAD. The simplicity of the method is proved by the fact that the PDMS foil, coated at room temperature in a single step, can be bent without any special precaution or consideration about the curvature degree (e.g., any unspecific hand bending produces quite reproducible results).

The mechanical stress induced by the first bending event is released by the formation of a regular micrometric parallel crack structure. Once this pattern is formed, the structure can accommodate the stress of subsequent bending events by either increasing the inter-crack spacing (i.e, convex surfaces) or by forming a parallel periodic distribution of valleys and crests (i.e., concave surfaces) with a periodicity defined by the inter-crack spacing.

These regular structures are the diffractive elements responsible of the optical properties of the concave surfaces. It should be noted that the characteristics of the pattern (i.e., inter-crack distances and periodicity) are reproducibly determined by the thin film nanostructure and not by the bending process.

In summary, when the film is bent forming a concave surface the PDMS wrinkles and the oxide film form a periodic distribution of valleys and ridges following the substrate undulations and preserving the pattern structure.

Two important features of the reported process differ from the common knowledge about patterning based on wrinkling or cracking of films on compliant substrates. The first one is its formation by manually bending instead of by well-controlled uniaxial straining. The second and most important difference is that the magnitude of the externally applied stress (i.e., degree of bending) does not affect the resulting pattern structure which is entirely dependent of the thin film nanostructure. Besides, the obtained results show that although the pattern generation upon bending is quite dependent on film structural parameters linked to the film nanocolumnar structure (i.e., tilting angle and thin film density) and its in-

plane anisotropy/isotropy, it is independent on its thickness. However, to fully understand this mechanism of bending induced fracture and why it is determined by the film nanostructure, mechanical simulations are deemed necessary.

Due to the large variety of single and multilayered nanostructured organic, inorganic and hybrid thin films that can be fabricated by GLAD (i.e., locally anisotropic films, nanostructured multilayers, photonic crystals, etc.) and the extreme simplicity of the procedure, it can be a starting point for new micro/nanopatterning design strategies of photonic elements, opto-mechanical actuators, reversible microfluidics valves, controlled wetting or security labeling, among others.

5.5 Supporting Information
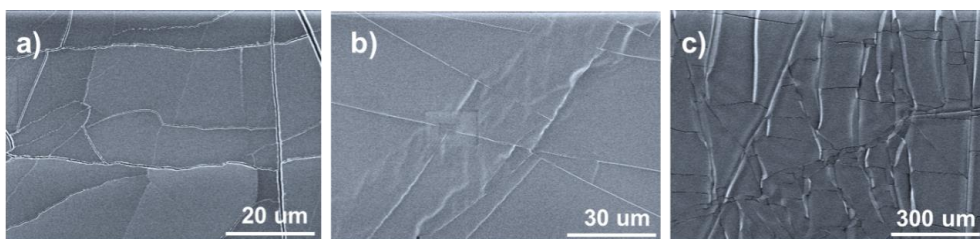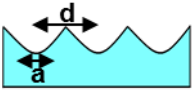
Figure S5.1. *Cracks formed in the surface of the non-columnar SiO_2 reference samples deposited on PDMS after a single bending event. **a**, FESEM micrograph of a sample obtained by oxygen plasma surface oxidation of a PDMS foil (Microwave remote plasma operating at 150 W during 180 min at 10^{-3} mbar at room temperature). **b**, FESEM micrograph of a SiO_2 thin film of a ~150 nm thick film deposited on PDMS by Plasma CVD at room temperature[1] **c**, FESEM micrograph of a ~150 nm thick SiO_2 thin film deposited by electron evaporation of silica pellets at normal incidence and room temperature.*
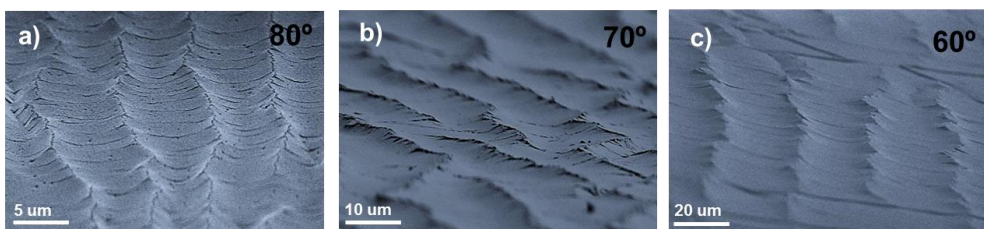
Figure S5.2 *Examples of GLAD SiO_2 thin films deposited on PDMS observed after bending along the **x** axis and with the deposited film forming a concave surface. **a**, FESEM micrograph of a thin film deposited at 80º glancing incidence. **b**, FESEM micrograph of a thin film deposited at 70º glancing incidence. **c**, FESEM micrograph of a thin film deposited at 60º glancing incidence.*

$$I = I_0 \left[\frac{\sin\left(N\pi \frac{d}{\lambda}\sin\theta\right)}{\sin\left(\pi\frac{d}{\lambda}\sin\theta\right)} \right]^2 \left[\frac{\sin\left(\pi\frac{a}{\lambda}\sin\theta\right)}{\pi\frac{a}{\lambda}\sin\theta} \right]^2 \quad (1)$$

*S5.3. Calculation of the diffraction spectra of Fig. 5a. The experimental diffraction pattern for are easily reproduced for λ= 532 nm by using the Fraunhofer diffraction equation (1) where N=100 the number of slits. For the x axis the slit width **a** was ~1 μm and the spacing value **d** the value determined from the FESEM micrographs in Figure 2. For the y axis the simulation was done combining two diffraction gratings with **a** = 4.7 and 6.6 μm and **d** = 7 and 10.5 μm, respectively, also within the values determined experimentally (Figure 2 and Figure 3).*
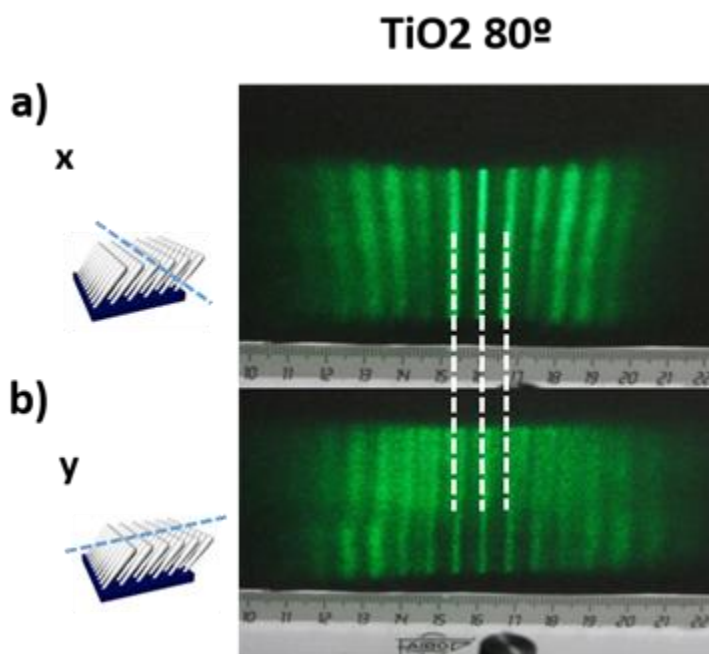
Figure S5.4. *Diffraction patterns of a 532 nm focused laser line passing through a bent TiO₂ thin film deposited on PDMS by GLAD at 80° glancing angle. The diffraction patterns corresponding to the **x** (a) and **y** (b) bending axes are very similar*

REFERENCES

(1) Bowden, N.; Brittain, S; Evans, A.G.; Hutchinson, J.W.; Whitesides, G.M. Nature 1998, 393, 146-149.

(2) Bowden, N.; Huck, W.T.S.; Paul, K.E.; Whitesides, G.M. Appl. Phys. Lett. 1998, 75, 2557-2559.

(3) Huck, W.T.S.; Bowden, N.; Onck, P.; Pardoen, T.; Hutchinson, J.W.; Whitesides, G.M. Langmuir 2000, 16, 3497-3501.

(4) Ohzono, T.; Monobe, H.; Shiokawa, K.; Fujiwara, M.; Shimizua, Y. Soft Matter 2009,5, 4658-4664.

(5) Khare, K.; Zhou, J.; Yang, S. Langmuir 2009, 25, 12794-12799.

(6) Efimenko, K.; Rackaitis, M.; Manias, E.; Vaziri, A.; Mahadevan, L.; Genzer, J. Nat. Mater. 2005, 4, 293-297.

(7) Jiang, X.; Takayama, S; Qian, X.; Ostuni, E.; Wu, H.; Bowden, N.; LeDuc, P.; Ingber, D.E.; Whitesides, G.M. Langmuir, 2002, 18, 3273–3280.

(8) Tawfick, S.; De Volder, M.; Davor, C.; Park, S.J.; Oliver, C.R.; Polsen, E.S.; Roberts, M.J.; Hart, A.J. Adv. Mater. 2012, 24, 1628-1674.

(9) Maruyama, T.; Hirakata, H.; Yonezu, A.; Minoshima, K. Appl. Phys. Lett., 2011, 98, 041908

(10) Stafford, C.M.; Harrison, C.; Beers, K.L.; Karim, A.; Amis, E.J.; Vanlandingham, M.R.; Kim, H.C.; Volksen, W.; Miller, R.D.; Simonyl, E.E. Nat. Mater. 2004, 3, 545-550.

(11) Genzer, J.; Groenewold, J. Soft. Mater. 2006, 2, 310-323.

(12) Chung, J.Y.; Nolte, A.J.; Stafford, C. Adv. Mater. 2011, 23, 349-368.

(13) Chung, J.Y.; Chastek, T.Q.; Fasolka, M.J.; Ro, H.W.; Stafford, C.M. ACS Nano, 2009, 3, 844-852.

(14) Robbie, K.; Brett, M.J.; J. Vac. Sci. Technol. 1997, 15, 1460-1465.

(15) Hawkeye, M.M.; Brett, M.J. J. Vac. Sci. Technol. A, 2007, 25, 1317-1335.

(16) Kennedy, S.R.; Brett, M.J.; Appl. Opt. 2003, 42, 4573-4579.

(17) Gonzalez-García, L.; Barranco, A.; Paez, A.M.; Gonzalez-Elipe, A.R.; García-Gutierrez, M.C.; Hernández, J.J.; Rueda, D.R.; Ezquerra, T.A.; Babonneau, D.; ChemPhysChem. 2010, 11, 2205-2208.

(18) Sanchez-Valencia, J.R.; Toudert, J.; Borras, A.; Lopez-Santos, C.; Barranco, A.; Feliu, I.O.; Gonzalez-Elipe, A.R. Plasmonics, 2010, 5, 241-250.

(19) Van Kranenburg, H.; Lodder, C. Mat. Sci. Eng. R. 1994, 11, 295-354.

(20) Sanchez-Valencia, J.R.; Toudert, J.; Borras, A.; Barranco, A.; Lahoz, R.; de la Fuente, G.F.; Frutos, F.; Gonzalez-Elipe, A.R. Adv. Mater. 2011, 23, 848-853.

(21) Gonzalez-Garcia, L.; Parra-Barranco, J.; Sanchez-Valencia, J.R.; Ferrer, J.; Garcia-Gutierrez, M.C.; Barranco, A.; Gonzalez-Elipe, A.R. Adv. Funct. Mater. 2013, 23, 1655-1663.

(22) Sanchez-Valencia, J.R., Blaszczyk-Lezak, I.; Espinos, J.P.; S. Hamad, Gonzalez-Elipe, A.R.; Barranco, A. Langmuir 2009, 25, 9140-9148.

(23) Gaillard, Y.; Rico, V.J.; Jimenez-Pique, E.; González-Elipe, A.R. J. Phys. D: Appl. Phys. 2009, 42, 145305, 1-9.

(24) Thouless, M.D. J. Am. Ceram. Soc. 1990, 73, 2144-2146.

(25) Thouless, M.D.; Li, Z.; Douville, N.J.; Takayama, S. J. Mech. Phys. Solids 2011, 59, 1927-1937.

(26) Zhu, X.; Mills, K.L.; Peters, P.R.; Bahng, J.H.; Liu, E.H.; Shim, J.; Naruse, K.; Csete, M.E.; Thouless, M.D.; Takayama, S. Nat. Mat. 2005,4, 403-406.

(27) Huh, D.; Mills, K.L; Zhu, X.; Burns, M.A.; Thouless, M.D.; Sakayama, S. Nat. Mater. 2007, 6, 424-428.

(28) Alcaire, M.; Sanchez-Valencia, J.R.; Aparicio F.J., Sagui, Z.; Gonzalez-Gonzalez, J.C.; Barranco, A.; Oulad-Zian, Y.; Gonzalez-Elipe, A.R.;, Midgley, P.; Espinos, J.P., Groening, P.; Borras, A. Nanoscale 2011, 3, 4554-4559.

(29) Barranco, A.; Cotrino, J.; Yubero, F.; Espinos, J.P.; Gonzalez-Elipe, A.R. Thin Solid Films 2001, 401, 150-158.

(30) Chua, D.B.H.; Ng, H.T.; Li, S.F.Y. Appl. Phys. Lett. 2000, 76, 721-723.

(31) Kim, P.; Hu, Y.; Alvarenga, J.; Kolle, M.; Suo, Z.; Aizenberg, J. Adv. Opt. Mat. 2013, 1, 381-388.

(32) Ohzono, T.; Suzuki, K.; Yamaguchi, T.; Fukuda, N. Adv. Opt. Mat. 2013, 1, 374-380.

Chapter 6

Tunable Anisotropic Wetting in Glancing Angle Deposited TiO$_2$ Coatings on Elastomeric PDMS Substrates

6.1. Introduction

Anisotropic devices for the control of directional flow of liquids is an emerging field of investigation and industrial development in energy efficiency systems to get self-cleaning surfaces[1] or microfluidic devices with a controlled droplet transport mechanism[2]. To promote the liquids movement along a preferential direction, wettability must be adapted through the surface chemistry and the morphological structure.

Particularly, geometrical modifications altering the surface roughness have been inspired in the hierarchical structures in the nature[3–6]. Thus, the fabrication of patterned surfaces by lithographic methods[7,8] may produce high water repellency and low flow resistance[9,10]. In a patterned surface, the liquid movement is favorable on the parallel direction due to the lower energy barrier for wetting[11–13]. In the same way, nanostructured thin films grown by GLAD presented a pin-release droplet mechanism[2]. However, these anisotropic structures have usually a high contact angle hysteresis complicating the water drops roll off. In addition, the wetting behavior of a surface cannot be extrapolated to different liquids restricting the feasibility for actual applications.

It is well-known that the surface wettability depends on both, the surface tension and the topography. Surface tension is controlled by chemical composition whereas the roughness, from the micro- to the nano- scale, can tune the wetting behavior from superhydrophobic (WCA water contact angle > 150º) to superhydrophilic states (WCA < 10º). For the case of a patterned surface, the inter-grooves distance has an influence on the range of liquid-air-solid surface interactions during the wetting. Micro-scale features are related to the droplet pinning on a surface according to the Wenzel's model[14], whereas the presence of a dual-scale roughness seems to be crucial for the superhydrophobicity and droplet mobility as the Cassie-Baxter model suggests[15].

Dual-scale roughness is also a critical requirement for anisotropic oil wetting. In fact, even in the case of omniphobic surfaces providing high contact angles and low contact angle hysteresis (CAH) ($< \sim 10°$) the anisotropic dual-scale roughness is sine qua non to induce a directional oil sliding[6]. The presence of nano-roughness generally contributes to a larger contact angle as well as a smaller sliding angle as seen from the lotus effect, but oil is able to wet the nano-roughness due to its low surface tension, complicating the control of directional oil drops transport. Consequently, a dual-scale roughness, achieved by the incorporation of nanoparticles[1,5,6,16], laser modification[17] or plasma treatments[18] among others, may assure the droplet sliding. Nevertheless, the effect of these processes on flexible substrates is unexpected or difficultly manageable.

In elastomeric surfaces it is possible to get a roughness change in the micro-scale by means of the ripples generation from applying a mechanical strain. Therefore, the self-patterned surface of elastomeric materials by means of wrinkling may promote a reversibly tune of the anisotropic wetting by altering the surface topography[16,19]. Thus, the use of elastomers for managing the wetting properties has recently open the way for the fabrication of microfluidics and biomedical devices such as microfluidic valves and mixers[6], anti-fouling materials or for cell transport manipulation[13]. As promising configurations, TiO_2 thin films on PDMS have been demonstrated special transparent self-cleaning protective properties[20–22], good photocatalytic behavior, optical diffusive reflector response[22,23], low-power strain sensor[24] and filtering ability for oil-water separation[25] using the self-organized wrinkling of the elastomeric substrate.

However, the generated undulations are randomly distributed on the surface, without any exhaustive control of the ripple appearance or orientation required to direct the selective liquid movement on a patterned surface. Besides, most mechanically switchable wetting devices presented in the literature needed

complex fabrication processes[13,16,26] involving nanoparticles deposition[22,27] and superhydrophobic functionalization in order to get a broad change of the contact angle[1,5,6,16,27–29] .

In the previous chapter was demonstrated that reversible/switchable optical gratings can be obtained by bending flexible PDMS foils coated with nanocolumnar SiO_2 thin films prepared by GLAD. The mechanical stress induced by the first bending event was released by the formation of a regular micrometric parallel crack structure. A complete study of this self-organized anisotropic micro pattering process in presented in Chapter 5. Once this pattern was formed, the structure accommodates the stress of subsequent bending events by either increasing the inter-crack spacing (i.e, convex surfaces) or by forming a parallel periodic distribution of valleys and crests (i.e., concave surfaces) with a periodicity defined by the inter-crack spacing. The formation of these oriented anisotropic regular distributions of parallel microgrooves was reproducible determined by the film bundled nanostructure and shown to be independent of the film thickness. Besides, the pattern microstructure was independent of the bending process characteristics like number of bending events or bending curvature.

In this work, oriented tilted columnar structured TiO_2 coatings grown by Glancing Angle Deposition (GLAD) on elastomeric polidimethylsiloxane (PDMS) substrates have been deposited. By mechanical deformation (bending or stretching) the nanocolumnar film structures generate a dual-scale roughness self-patterned system. These patterned surfaces show anisotropic wettability that can be directly controlled by manual manipulation with promising potential application in microfluidic devices.

.

6.2 Experimental set up

Polidimethylsiloxane (PDMS) foils of 2x2 cm^2 and 1,5 mm of thickness were fabricated by mixing the Sylgard 184 (DOW) two part silicon elastomer and degassing and curing the mixture at 80ºC during 1 hour. PDMS foils were growing on silicon wafers to replicate the smooth roughness and microstructure. Such as has been explained in chapter 5

TiO$_2$ thin films with 300 nm of thickness have been prepared on PDMS foils in an e-beam evaporator set-up under glancing angle (GLAD) conditions previously described[19]. GLAD methodology uses the arriving of a vapor flux at glancing angle $\theta \geq 60º$ with respect to the substrate surface for the fabrication of tilted oriented nanocolumnar thin films. TiO pellets (Kurt J. Lesker Company) were placed in a carbon crucible that was subjected to e-beam bombardment at an oxygen pressure of $5x10^{-4}$ Torr for the synthesis of the TiO$_2$ films. A water cooled sample holder was used to prevent heating during deposition of the films on PDMS with evaporation rates of 0.8-1 Å/s [30,31]. For simplicity, samples from two extreme glancing angle configurations are studied: tilted columnar TiO$_2$ thin films under 60º and 85º deposition angles hereafter named G-60º- and G-85º-TiO$_2$/PDMS films.

Surface characterization.

Regular ripples / grooves were generated on the surface of TiO$_2$ thin films on PDMS when the systems were deformed along the orthogonal directions given by the nanocolumnar growth (growing) and the columns stacking (bundling) directions. Samples were subjected to non-deformed, concave and convex bending with a curvature of 0.55 cm and stretching configurations for both sample's orientations. Similar reproducible wrinkled pattern than those presented on GLAD SiO$_2$/PDMS systems was remained unaltered after flexible manipulation on the film for several times (See Chapter 5).

Microstructure characterization was carried out with a Hitachi S-4800 scanning electronic microscope (FESEM) at 2KV. Surface topography was analyzed by atomic force microscopy (AFM) in a Dulcinea microscope from Nanotec working in tapping mode and using high-frequency cantilevers. AFM images, taken on different surface ranges as 40x40 μm^2 and 5x5 μm^2, were processed with the WSxM software freely available from Nanotec[30].

Wetting characterization was accomplished through the deposition of small distilled water droplets (2, 5, 20 and 30 μl of volume) and diodomethane droplets (2 and 5 μl of volume) on the surface of the TiO_2/PDMS samples in a Contact Angle System OCA from Dataphysics. Static and dynamic contact angles have been studied as well as the hysteresis contact angle and sliding properties under the deformation configurations previously indicated.

.

6.3. Results and discussion

6.3.1. Microstructural characterization of the self-patterned TiO_2/PDMS surface

GLAD oxide thin films present a well-defined tilted nanocolumnar structure as a function of the deposition glancing angle that is the results of shadowing effects during the film growth[32,33] . Transparent nanostructured TiO_2 thin films have been deposited on a flat flexible PDMS foils at different glancing angles. The observed tilted nanostructures are very similar to those obtained in rigid substrates[19,31,34] as shown in the previous chapter, similarly to what was reported for the SiO_2/PDMS system)[19]

In some materials, the nanocolumnar films tends to aggregate in the form of linear columns associations along the direction perpendicular to the incoming material flux by a process known as bundling[19,34,35]. It is interesting to note that a system formed by tilted columns is essentially anisotropic but the bundling

association introduced additional in-plane anisotropy in the GLAD films such as have been explained in the previous chapters.

The nanocolumnar bundling is a function of the deposition glancing angle and material composition. Previous works took advantage of this anysotropic column association process to prepare percolated silver nano-stripes on the surface of SiO_2 GLAD thin films by a combined silver evaporation and laser treatment procedure[34,36] and for the growth of oriented anisotropic dichroic gold nanoparticles in the bulk of nanocolumnar SiO_2 GLAD films [31]TiO_2 GLAD films show less pronounced bundling[30] effects than the SiO_2 GLAD films. The bundling association is less effective as the deposition angle increases being nearly absent in TiO_2 films deposited at the higher studied glancing angle (i.e., ~85º) (See Chapter 5).

Additionally, it has been demonstrated that further microstructuration of the films is possible by simply bending or stretching along the bundling and growing directions of oxidized nanocolumnar coatings on flexible PDMS foils. In this way, micrometric parallel wrinkles are formed with feature parameters such as shape and distance between grooves controlled through the nanostructure of the GLAD films: tilting angle and bundling. The formation of parallel grooves on the GLAD thin films/PDMS surfaces is then related to the combination of tilted oriented columnar nanostructures and the nanocolumnar bundling.

Figure 6.1a) shows the parallel distribution of grooves on the G-TiO_2/PDMS surface is observed flat after being bent along the x_b axis (bundling axis). Similarly to the results of G-SiO_2/PDMS films the obtained inter-groove distances are independent of the bending curvature and film thickness but are a function of the deposition glancing angle value (See chapter 5). The distances between parallel grooves were higher for the G-60º-TiO_2/PDMS sample than the 85TiO_2/PDMS one (Figs. 6.1a)-c)). More compact G-60º-TiO_2/PDMS surface provided larger inter-groove distances after bending and a higher dispersion of the groove spacing values Although TiO_2 porous thin films experienced less bundling effects compared with other oxides like SiO_2 as previously indicated in chapter 5 bending in x_b and y_g (growing axis) directions generated different patterns of

parallel grooves, being slightly more separated those obtained by bending along the growing direction. Moreover, the stretching experiments produced higher groove distances than bending (see Figs6. 1b) and c)).
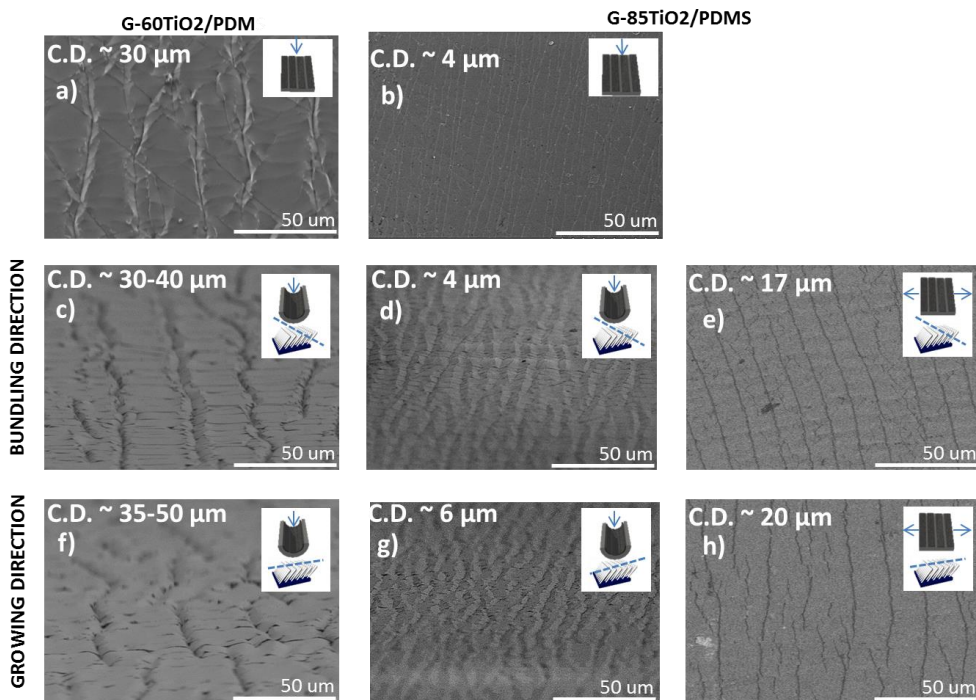
Figure 6.1. *FESEM micrographs of G-60º-TiO$_2$/PDMS(left) and G-85º-TiO$_2$/PDMS surfaces. a) Flat surfaces after bending the coated foils along the x$_b$ (bundling axis) and y$_g$ (growing axis) directions b) micrographs of the G-TiO$_2$/PDMS film bent along the x$_b$ direction forming a concave and convex surface and stretched perpendicular to the x$_b$ direction with the film on top in all the cases c) micrographs of the G-TiO$_2$/PDMS film bent along the y$_g$ direction forming a concave and convex surface with the film on top and stretched perpendicular to the y$_g$ direction with the film on top in all the cases. The thicknesses of the films in this figure are ~300 nm thick. The corresponding glancing angles are indicated in each micrograph.*

The results of the AFM analysis of the G-TiO$_2$/PDMS films show an increase in the surface roughness compared with the very low roughness of the uncoated polymer substrate surface (Figure 6.2). TiO$_2$ roughness increases as the tilting angle deposition increases similarly to what has been observed in different flat substrates due to the development of a more tilted columnar microstructure and the associated decrease in film density [30]. When the films are bent or stretched a notable increase in the roughness rise is observed.

These results from the AFM analysis at two monitoring scales are gathered in Table 6.1. In these AFM measurements, the nanocolumnar TiO$_2$ film surface determined the topography of the small scale analysis whereas the higher image scale analysis are determined by the observation of the grooves. Thus, when the G-TiO$_2$/PDMS system is bent or stretched, roughness values are almost one order of magnitude higher at the larger observation scale. During the AFM mapping of the G-60º-TiO$_2$/PDMS was not possible to include more than one of the grooves observed by FESEM (Fig. 6.1) whereas almost eight wrinkles could be included in the case of the G-85º-TiO$_2$/PDMS surface (Fig. 6.2) Concave bending configuration is the roughest, even for the PDMS foil. It is interesting to note that this occurs even for the nanocolumnar structured TiO$_2$ surface of lower tilting angle, although the image size is in the order of the inter-grooves distance.
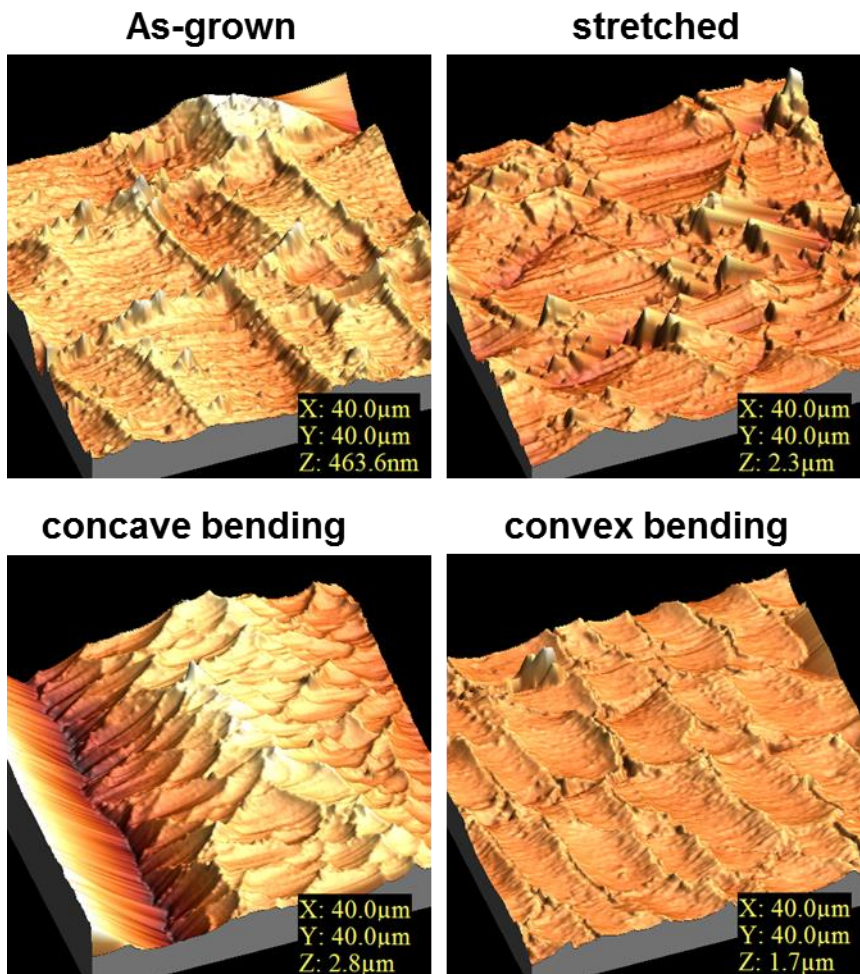
Figure 6.2.- *AFM images of the G-85º-TiO$_2$/PDMS surface. As-grown, stretched and bent forming a concave and a convex surface. The thickness of the TiO$_2$ film is ~300 nm.*

In resume, roughness increase at the larger observation scale is dominated by the coating nanostructure or by the parallel grooves pattern for the G-60º-TiO$_2$/PDMS or G-85º-TiO$_2$/PDMS surfaces, respectively. Apart from the nanocolumnar structure and the groove formation the wrinkling of the PDMS at the interface when the film is bent forming a concave surface may contribute

significantly to the increase in roughness observed by AFM[19] . Thus, these three components determined the different scales of roughness of the G-TiO$_2$/PDMS system in the flat (after a single bending event), bent (forming a concave o convex surface) or stretched states.

Table 6.1 Roughness surface values determined from AFM of the PDMS foil, G-60º-TiO2/PDMS and G-85º-TiO2/PDMS at two different scales**.**

| Roughness		R_{ms} (nm) (40umx40um)	R_{ms} (nm) (5umx5um)
PDMS	As-grown	17	1
	Concave	39	3
	Convex	15	2
	Stretched	12	1
G-60ºTiO$_2$ /PDMS	As-grown	36	12
	Concave	212	24
	Convex	110	6
	Stretched	142	8
G-85ºTiO$_2$ /PDMS	As-grown	44	15
	Concave	174	26
	Convex	66	8
	Stretched	170	11

6.3.2 Wetting behavior of the TiO$_2$/PDMS surface

In this section will be analyze the wettability of the patterned surfaces characterized using two different liquids of different polarity, water and diiodomethane and under stressed configurations in the two surface orientations (growing and bundling) of the G-TiO$_2$/PDMS samples compared to the flat state. The sliding (also called roll-off) response, referred to α^{II} and α^{N} when sliding angle is measured in a parallel way to the applied stress direction or in the normal one. The wetting contact angle (φ) of a drop on a flat surface is determined by the classical Young's law being the result of the balance among the cohesive forces acting in the contact line between a liquid drop deposited on a surface at equilibrium conditions with the environment:

$$\cos \varphi = \frac{\gamma_{SV} - \gamma_{SL}}{\gamma_{LV}} \ (1)$$

where γ_{SV}, γ_{SL} and γ_{LV} refer to the interfacial tension in the solid-vapor, solid-liquid and liquid-vapor interfaces, respectively. The oriented structured G-TiO$_2$/PDMS surface presents a similar hydrophobic state as a function of the drop volume and the surface orientation as shown in Figure 6.3a) for a G-60TiO$_2$/PDMS sample and an uncoated PDMS foil. However, the particular thin film surface formed by the nanocolumnar oxide and the parallel groove pattern present a particular critical drop size for the water drop to roll off..

Particularly, water sliding angles decrease as the drop volume increase presenting slight differences between growing and bundling direction at high liquid volumes with a better droplet rolling along the bundling direction on the surface as shown in Figure 6.3a). The pictures in Figure 6.4a) show an example of water sliding along the growing direction of the G-60°-TiO$_2$/PDMS film.
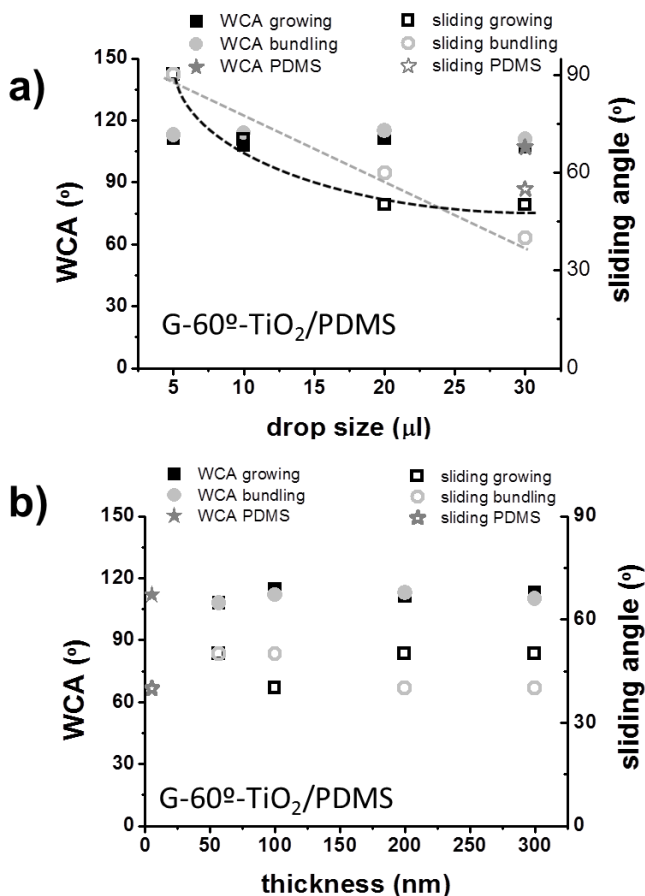
Figure 6.3. *Wetting contact angle and sliding angle values for the growing and bundling directions as a function of a) water droplet volume and b) the thin films thickness for the G-60º-TiO2/PDMS system for a drop of 30 μl . The figures also include the values of a uncoated PDMS foil.A ll measurementa have been done accepting 3-5% of error.*

Roughness as well as structural or chemical heterogeneities cause some digressions from the ideal Young's situation, originating a wetting hysteresis (HCA) estimated with the dynamic contact angle analysis i.e., the difference in the contact angle when a drop is increasing in volume on the surface and when is withdrawn from it. These magnitudes are called advancing (φ_a) and receding (φ_r) contact angles. Hysteresis contact angle is related to the liquid adhesion or the roll-off property of a liquid drop on the surface representing as the tilt angle (α) when a liquid drop starts to move on a surface[37]:

$$\sin \alpha = \frac{w}{mg} \gamma_{LV} (\cos \varphi_r - \cos \varphi_a) \quad (2)$$

with w the maximum width of the contact area of the liquid drop and the surface, m the mass of the liquid drop, g the gravity force constant and γ_{LV} the liquid surface tension.
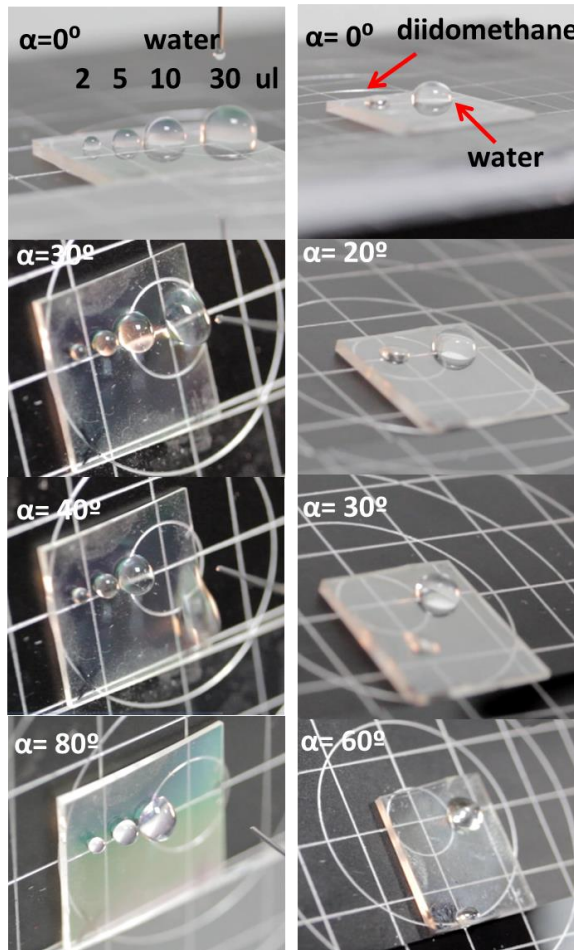
Figure 6.4*. a) Images of 2,5,10 and 30 μl water drops rolling off in function of the sliding angle (α) through the growing direction of G.60º-TiO$_2$/PDMS foil b) Images of 10 μl water drops and 5 μl diiodomethane drops rolling off in function of the sliding angle (α) in the growing direction of a G-85º-TiO$_2$/PDMS surface. All measurements have been done accepting 3-5% of error.*

Taking into account this expression of the flow resistance, it is expected that the gravity effects prevail over the surface tension effects as the droplet volume increases or the hysteresis decreases as seen in Figure 6.4a). Previously, S-G Lee et al[5] presented a similar tendency on a wrinkled PDMS surface, where a critical volume of 35ul was needed to roll off a water droplet on a surface with roughness around 40 nm. Also, they observed how the critical water volume at which the parallel and perpendicular roll-off angles converged decreased with the surface roughness. Meanwhile N.A. Malvadkar et al.[2] found similar anisotropic sliding behavior with comparable water drop volumes in columnar parylene GLAD thin films, what displayed great retention forces, 80μN higher in the pinning direction than in the release one.

Attending to their indicated estimation of the static load-bearing capability for knowing the maximum water drop volume that the GLAD structure could support, the maximum surface tension force imparted by these GLAD nanocolumnar G-TiO$_2$/PDMS surfaces is three orders of magnitude lower than the parylene GLAD structure, being even smaller in the more porous G-TiO$_2$/PDMS film, ie. the G-85°-TiO$_2$/PDMS surface.

Nevertheless, these values are high enough to promote the pinning of large water droplets, through the present smaller column diameter that should hold larger droplets. In addition, Figure 6.3b), shows there is not a clear influence between the coating thickness the water contact angle and the sliding angles. Consequently, the parallel micrometric groove structure seems to have the higher influence in the hydrophobicity.
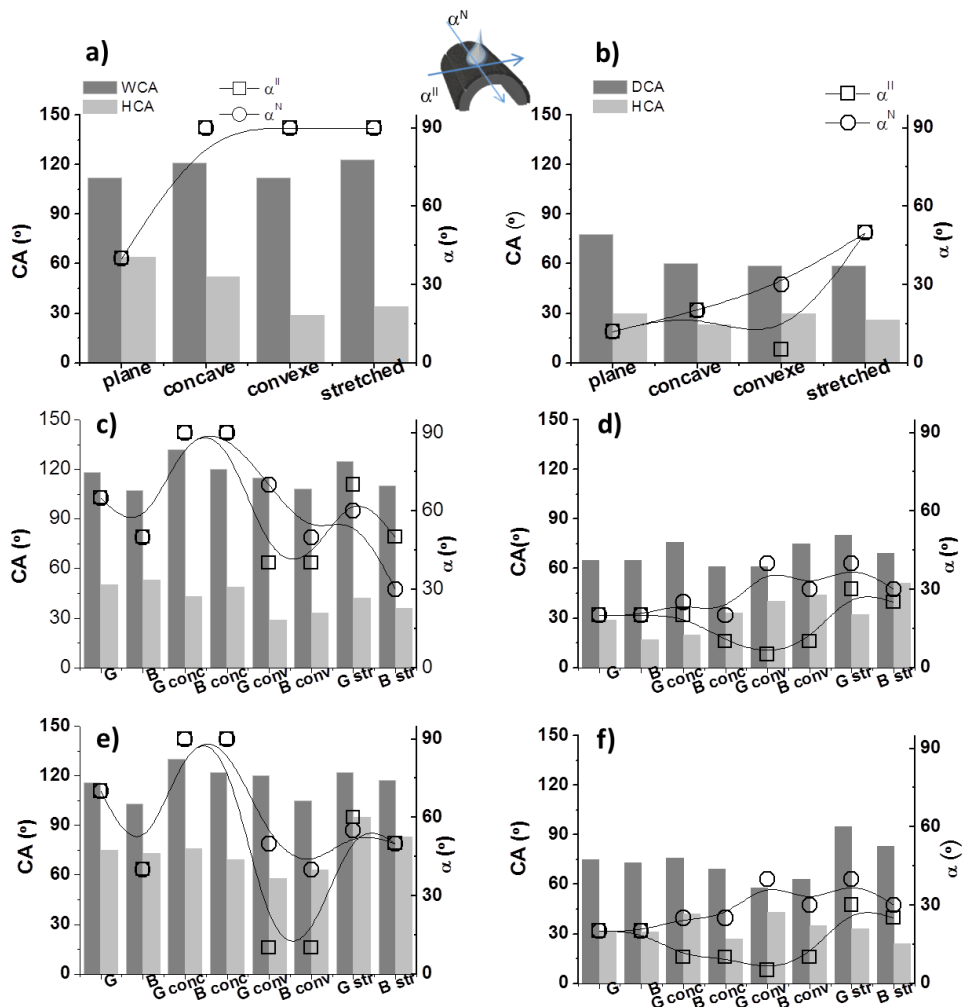
Figure 6.5. Wetting and hysteresis contact angle vs mechanicals deformations (bar chart) spectra and sliding angle vs mechanical deformations (squares and circles) values corresponding to a) a PDMS foil b) a G-60º-TiO$_2$/PDMS surface and c) a G-85º-TiO$_2$/PDMS surface along the growing (G) and bundling (B) directions. The volume of the water and diiodomethane droplets are 30 ul and 5 ul, respectively. The foils have been studied flat, forming a concave and convex surface and stretched. αII and αN are the sliding angles parallel and perpendicular to the particular mechanical deformation studied as indicated in the schematics where αII is always parallel to the groove structure.

By contrast with the previous results, diiodomethane droplets do not find energy barriers for sliding on the patterned G-60-TiO$_2$/PDMS system as shown in Figure 6.4b) where 20µl water and 5µl diiodomethane drops rolling off in function of the sliding angle through the growing direction. In view of this behavior, where water droplet is retained on the surface whereas diiodomethane droplet goes effortlessly across the surface, the G-TiO$_2$/PDMS system can be presented as a firm candidate to be used for oil-water separation systems at the micro-scale and other lab-on-a-chip devices of use in microfluidic or biomedical applications.

Figure 6.5 show selected results of an anisotropic wetting study in the G-TiO$_2$/PDMS surfaces.) The experimental results indicate the water contact angle is higher in the growing direction, whereas the bundling direction presented a lower value even when the system is under the mechanical manipulation.

These findings suggest that the effect of the oriented fracture of the G-TiO$_2$/PDMS surface caused by bending and stretching of the substrate determined the anisotropic wetting of the system. Usually water molecules are dissociatively adsorbed on defect sites, producing absorbed OH groups that reduce the water contact angle. On a rigid substrate, lower glancing deposition angles induced a more hydrophobic surface than the higher ones as an effect of a more compact developed structure with a lower roughness[30]. Here, the same tendency is achieved with the TiO$_2$ coatings on the non-deformed flexible substrate.

Morphological anisotropy has also an effect on the water sliding: water drop rolls off from the bundling oriented G-TiO$_2$/PDMS surface at similar sliding angles than from the PDMS foil whereas the sliding angles are higher in the growing direction of the TiO$_2$ structure. It should be noted that this oriented sliding was not observed with a non-polar liquid and, apparently, its sliding on the G-TiO$_2$/PDMS surface is also deteriorated compared to the PDMS one. Dual-scale roughness affecting the anisotropic wettability of a wrinkled surface can be interpreted using both Wenzel's[14] and Cassie-Baxter's models[15] that depend on the ripple wavelength and amplitude characteristics as well as the Young's contact angle[16]:

$$\cos \varphi^{W} = r \, \cos \varphi \ (3)$$

$$\cos \varphi^{CB} = f_{CB} \cos \varphi + f_{CB} - 1 \ (4)$$

The apparent contact angle on a rough surface, θ^{W}, is a function of the Young's contact angle on a flat surface, θ, through a roughness factor, r, defined as the ratio between the real surface area and the projected surface area. Therefore, Wenzel's assumption includes the completely wetting of the grooves of the PDMS surface by water. However, in porous structured surfaces, it is possible that the liquid does not fill the grooves and the air can be trapped below it. For that the Cassie-Baxter' model predicts the formation of a multi-phase system being θ^{CB} the contact angle on the solid surface and f_{CB} the solid surface forming the liquid-solid interface. Other factors in equation (4) come from the consideration of the air phase influence with a contact angle of 180º from the liquid-air interface.

A transition from the Cassie-Baxter's state to the Wenzel's state in a rippled surface[16] is expected if the geometrical wave characteristics, A/λ, , obeys $0.28 < \frac{A}{\lambda} < \frac{\tan \theta \varphi}{-2\pi}$, that corresponds to a mechanical strain value greater than the limit value for which the PDMS foil breaks. Therefore, for all the present stressed configurations, Wenzel's regime is more suitable to the G-TiO$_2$/PDMS wetting interpretation. Table 6.2 includes the wettability values of the equivalent flat surface confirms this assumption. Besides, S-G Lee et al.[5] confirmed the wrinkled PDMS wettability in the fully wetted Wenzel' state is barrierless because the transition between the Wenzel state (lower energy state) and the air-trapped Cassie state (higher energy state). In the end, roughness seems to have a poor influence in the PDMS hydrophobicity changes, where only a roughness increase is possible with the concave bending.

Table 6.2.- Wettability values corresponding to the equivalent flat surface for the G-60º-TiO$_2$/PDMS and G-85º-TiO$_2$/PDMS films and a reference PDMS foil.

Wetting of equivalent flat surface		θ (º)	θ^w (º) 40um	θ^w (º) 5um	θ^{CB} (º) 40um	θ^{CB} (º) 5um
PDMS	**As-grown**	112	112	112	87	83
	Concave	121	121	121	109	91
	Convex	112	112	112	79	79
	Stretched	123	123	123	90	95
G-60ºTiO₂ /PDMS	**As-grown**	118	118	118	95	97
	Concave	132	127	132	119	116
	Convex	115	114	115	96	91
	Stretched	125	123	125	98	101
G-85ºTiO₂ /PDMS	**As-grown**	116	115	114	87	92
	Concave	130	127	129	110	109
	Convex	120	119	119	96	102
	Stretched	122	118	122	101	99

6.3.3 Selective wetting TiO₂/PDMS devices by mechanical deformation

- *Wetting of PDMS under external strain*

Hydrophobicity is slightly emphasized when PDMS substrate is deformed, from a water contact angle value of 112º when PDMS is in a flat or convex (conv.) configuration to a value around 123º when PDMS is stretched (str.) or concave (conc.) bent (Figure 6.5 (a)). When PDMS is in contact with water, the dipole of the siloxane backbone is the dominant interaction and its surface becomes more

hydrophilic than in contact with air, where the pendant methyl groups in PDMS are closely packed at the interface[38]. Also, the flexible Si–O backbone is easily readapted to the lowest surface energy conformations responding to the mechanical changes. Surface tension, introduced in Table 6.3 and estimated by means of the contact angle measurement with diiodomethane, reveals differences in the wetting

behavior through the effect of the nature of the intermolecular forces by the Owens-Wendt-Kaelble approximation and the Young-Dupré equation[39]:

$$\gamma_L(1 + \cos \varphi) = 2\sqrt{\gamma_L^d \gamma_S^d} + 2\sqrt{\gamma_L^p \gamma_S^p} \quad (6)$$

Here, γ_L^d, γ_L^p, γ_s^d and γ_S^p are the dispersive and no dispersive/polar components of the surface tension for the liquid drop and the solid surface, respectively. Dispersive component is remarkably enlarged when PDMS foil is deformed, being the increasing tendency well correlated with the hydrophobicity level in the order: convex bending < concave bending < stretching. Therefore, dispersive component rise is pointing to a methyl groups exposition to the surface instead of the siloxane backbone when PDMS is subjected to the manual deformation. In the same way, water sliding on PDMS surface is suppressed under bending and stretching, whereas the easy diiodomethane sliding is complicated when the sample is stressed.

The deterioration of diiodomethane sliding on the concave bent PDMS foil may be related to the increase of the surface roughness. Moreover, the sliding obstacles during convex bending and stretching could be originated by several factors: polymeric chains alignment is possible along the stressed direction, where the Si-O backbone would be more exposed to the surface slowing down the liquid movement. Also, the formation of a surface layer rich in SiO_x would involve a spontaneous undulation of the PDMS surface[40] when is deformed and subsequently followed by obstruction of the liquid drop roll-off. It should be mentioned that the anisotropic sliding observed in Figure 5 (b) for the convex bent PDMS surface is product of the sample curvature in favor of the gravity effects: diiodomethane drop rolls off more easily in the parallel direction to the convex bending strain than in the normal direction to the applied tensile stress.

Table 6.3.- Surface tension values determined for the G-60º-TiO$_2$/PDMS and G-85º-TiO$_2$/PDMS films and a reference PDMS foil.

Surface Tension		WCA (º)	DCA (º)	Surf. tension (mN/m)	Polar c. (mN/m)	Dispersive c. (mN/m)
PDMS	**As-grown**	112	78	9,5	2,1	7,4
	Concave	121	60	46,9	1,1	45,7
	Convex	112	59	29,7	2,0	27,7
	Stretched	123	59	53,2	1,0	52,2
G-60ºTiO$_2$ /PDMS	**As-grown**	118	65	32,7	1,4	31,3
	Concave	132	76	41,6	0,5	41,1
	Convex	115	61	32,7	1,7	31,0
	Stretched	125	80	23,4	0,9	22,5
G-85ºTiO$_2$ /PDMS	**As-grown**	116	75	16,7	1,6	15,1
	Concave	130	76	37,9	0,6	37,3
	Convex	120	58	47,9	1,2	46,7
	Stretched	122	95	5,6	1,2	4,4

Wettability of TiO$_2$/PDMS under concave bending

Concave bending in the growing direction of the G-TiO$_2$/PDMS sample showed the highest hydrophobic state in Figure 6.5. Roughness of the G-TiO$_2$/PDMS surface increased by a factor 4-6 at high scale of observation, related to a more hydrophobic surface as Wenzel's model predicts. Also, structure arrangement to the external strain may induce the exposition of Ti-O-Ti groups at the surface or the migration of methyl groups from the substrate when wrinkles are required to be squeezed, in agreement with the increase in the dispersive component of the surface tension.

Nevertheless, no clear differences were revealed for the water wetting when the PDMS foil was concave bent in the bundling direction with or without the nanostructured TiO$_2$ coating. With these high contact angle values, water drops were pinned on the G-TiO$_2$/PDMS surface when bent in a concave way as took place for the bent PDMS foil.

However, roughness enlargement seems to be responsible for the water blocked movement on the surface at this case. Wenzel state explains the droplet pinning on a

wrinkled flexible surface with a high water adhesion due to a continuous and stable three phase (solid-liquid-air) contact line.

Contact angles of the deformed G-TiO$_2$/PDMS surfaces with non-polar liquids like diiodomethane are larger than the corresponding to the PDMS foil under the same external strain configurations. Nevertheless, diiodomethane is able to wet the parallel grooves and the hierarchical surface structure due to its low surface tension when is mechanically deformed.

In the case of diiodomethane sliding under concave bending, a preferential orientation for the liquid movement is facilitated by the mechanical deformation governed by the TiO$_2$ columns structure. When concave bending is applied on the bundling oriented G-TiO$_2$/PDMS surface, drop roll off enhances, showing different sliding behaviors in a parallel or perpendicular way to the external applied tension. Parallel sliding improved respect to the non-stressed situation or the similarly bent PDMS foil, whereas diiodomethane drops movement on the normal direction was more difficult.

This result presents the possibility to switch the movement of diiodomethane drops imposing the pin or liquid release in function of the surface pattern coming from the bending. According to S-M Kang et al[6], anisotropic oil sliding is possible on patterned flexible surfaces by the competition between internal gravity and Laplace pressures: if Laplace pressure is resisting against the gravity when oil penetrates into the structure and grooves, then drops slide smoothly without the wetting transition from Cassie to Wenzel state. Therefore, the energy barrier against the sliding of a diiodomethane droplet results higher in the normal orientation of the patterned structure.

Wettability of G-TiO$_2$/PDMS under convex bending

G-TiO$_2$/PDMS samples under convex bending presented similar water wettability than the non-deformed one in spite of the high roughness at large scales of observation, especially for the low deposition angle case. However, TiO$_2$ structure tends to soften the surface at low scale of observation when is bent. This

points to the influence of the scale of observation in the drop volume during the wetting experiments since different morphological changes will affect.

Therefore, for the same water drop size, the more porous $85TiO_2$/PDMS structure allows the surface migration of hydrophobic methyl groups[12] via the open cracks from the bent substrate. Surface tension values from Table 6.3 confirm this finding through the increase of the dispersive component with the convex bending compared to the unstressed situation. In spite of the non-appreciated hydrophobicity changes with the TiO_2 coating, water sliding was enhanced when the G-TiO_2/PDMS system is convex bent related to the dual-scale roughness developed on the surface through a combined groove and wrinkled pattern and the nanocolumnar TiO_2 structure.

Water drops circulates without any difficult on the more porous surface at difference of the non-deformed G-TiO_2/PDMS surface even after the bent of the PDMS foil as shown in Figure 6.5. Sliding is better in the parallel direction to the external deformation for both growing and bundling directions, where surface curvature produces an overlapped effect. However, surface curvature is not enough and the topography has a notable role in the anisotropic water sliding. Thus, the G-85°-TiO_2/PDMS sample favors the water drop rolling better than the G-60°-TiO_2/PDMS one in a parallel direction to the generated wrinkled structure under convex bending. S-G Lee et al[5] established isotropic/anisotropic sliding behaviors in function of the roughness on patterned surfaces. According to those results, one expects an isotropic rollable tendency of the water drops with roughness values higher than 100 nm and an anisotropic rollable tendency for a roughness range of 35-95nm inclined toward a better sliding in a parallel direction.

Thus, more anisotropic sliding found on the less rough G-85°-TiO_2/PDMS surface agrees with that dynamic water droplet transport. Particularly, the sliding angle normal to the grooves are higher than to the parallel ones because the three phase contact line for water droplet movement perpendicular to the grooves is more discontinuous due to the higher wetting/dewetting energy barrier[11]. If the strain is applied along the bundling direction, ordered grooves appear causing a "railway"

structural framework similar to the presented in the FESEM image, what directs the rolling of water drops, especially for the G-85º-TiO$_2$/PDMS case where closer wrinkles serve easily as guide for the water sliding.

An example of the control of the liquid movement on the G-TiO$_2$/PDMS surface applying a convex bending is presented in Figure 6.6. Pictures show selective water adhesion in function of the oriented microstructure. Although the water drop remains pinned on the tilted non-deformed surface, it is detached from the PDMS surface when bending in a vertical position since gravity effects exceed the surface tension interactions under the new geometrical configuration.
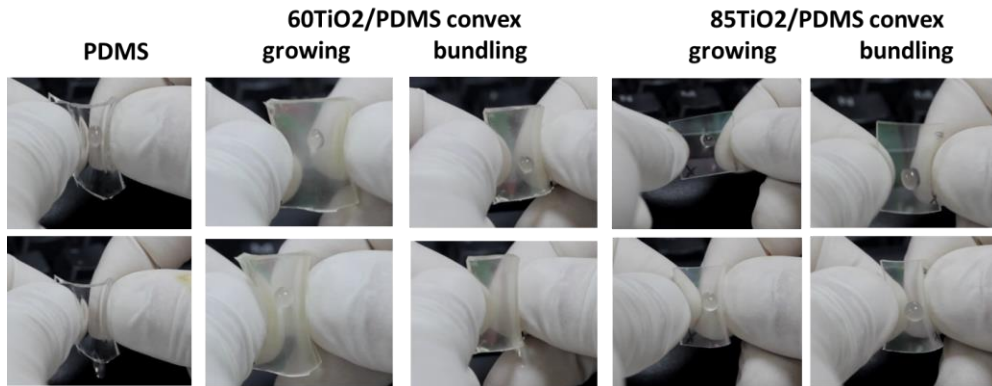
Figure 6.6. Selective water adhesion by bending the G-TiO$_2$/PDMS surface as a function of the microstructure.

However, it is possible to restrain the water droplet adhered to the G-60º-TiO$_2$/PDMS surface with the bending in the growing direction unlike the bundling one. When the surface is mechanically manipulated along the growing direction, cracks generation trying to relax the accumulated tensile stress increases the surface roughness leading to a disordered wrinkled pattern.

Water is able to fully wet the surface composed by grooves separated around 30-50um working as anchoring points. But, if convex bending is applied on

the bundling direction, water drop can leave the surface since sliding improves with better organized and closer cracks distribution on the surface, directing the liquid movement.

When the convex bending is applied on the G-85º-TiO$_2$/PDMS system, the previously deposited water droplet stays attached independently the structure orientation since the induced surface undulations are more similar. Porous surface accommodates the structure to the deformed configuration with less effort reducing the inter-grooves distance almost an order of magnitude and adopting a more regular rough aspect in both directions. Here the droplet stays adhered to the surface despite the action of the mechanical manipulation from a non-deformed situation where the closer undulations mean more fastening points at the liquid-surface interface.

As example, water droplet contact area on the bent surfaces can be roughly estimated from the water contact angle as $\sim\pi R^2$ with R=rsenθ, being r the droplet radius and θ the water contact angle supposing a spherical shape when is deposited on the surface. Taking into account crack distances of 40um and 6um for the G-60º-TiO$_2$/PDMS and G-85º-TiO$_2$/PDMS samples respectively, one expects to include 88 grooves per droplet diameter for the more compact case, facing more than 550 wrinkles per droplet diameter for the porous one.

Therefore, it may conclude that wrinkles distances of ~tens micrometers conditioned by the bundling structure generate an ordered surface pattern allowing droplet rolling when the sample is subjected to a convex bending from a tilted situation.

Diiodomethane anisotropic sliding was amplified with the convex bending, standing out the cases on the growing direction of the TiO$_2$ structure as shown in Figure 6.5 (d). Drops rolled off easier compared to the non-stressed samples in the parallel direction to the applied strain. Again, curvature effect can be prevailing as shown in the case of the PDMS foil under the same deformation. Consequently, it is possible the exposition of low molar mass PDMS fragments[12] across the TiO$_2$ structure when the system is bent. Diiodomethane sliding got slightly worse if

measuring in a normal direction to the convex bending because of the cracked surface, degenerating on the growing direction. At this situation, less aligned surface cracks are presented as a greater obstacle to the liquid flow.

Wettability of G-TiO$_2$/PDMS under stretching

When the G-TiO$_2$/PDMS sample is stretched in the growing direction, water contact angle did not present any significant change respect to the stretched PDMS sample, while a decrease of the water contact angle was presented in Figure 6.5 if the applied stress was along the bundling direction. G-TiO$_2$/PDMS roughness experienced a notable increase under stretching, especially for the TiO$_2$ structure grown at high deposition angle. However, it is only observable at large scale as a product of the grooves generation directing by the oriented TiO$_2$ structure.

This is a similar behavior to the obtained through the convex bending, but reaching higher inter-grooves distances. In general, water sliding is improved only if the mechanical stress is applied on the bundling direction. Other remarkable result is the increase of the diiodomethane contact angle when the TiO$_2$/PDMS surface is stretched, reaching an oleophobic surface state. It indicates that diiodomethane penetrates less in the stretched porous G-TiO$_2$/PDMS structure.

Indeed, stretching of the G-TiO$_2$/PDMS system is able to block the non-polar liquid sliding with an increase of the roll off angle, mainly in the growing direction of the patterned surface due to the dual-scale roughness of the wrinkled topography. Also, the Si-O backbone would be hanged on the surface involving opposite surface interactions to the diiodomethane drop movement, in agreement with the observed decrease of the dispersive component of the surface tension. Hence this manual change of the microstructure would be appropriate in selecting a non-polar liquid repelling/sliding surface.

Liquid movement control on the surface is clearly revealed under stretching of the G-TiO$_2$/PDMS system as Figure 6.7 (a) suggests. During the slow sliding of a water droplet on the G-85-TiO$_2$/PDMS surface, it is possible to completely stop its movement if the sample is stretched on the bundling orientation. Removal of the

manipulation provides the recovering of the initial surface wetting state. As the contact angle measurements indicated, this mechanical deformation involved a slight increase of the surface hydrophobicity accompanied by a high hysteresis contact angle. That means an intensification of the adhesion interactions at the liquid-solid interface making difficult the drop sliding on the surface. Moreover, with a non-polar liquid as diiodomethane,

Figure 6.7 (b) shows how droplets stay motionless on the growing-oriented stretched G-60º-TiO$_2$/PDMS surface immediately after the deposition. Then, when the external surface strain is relaxed, drops release until detach from the sample. A distinguished increase of the sliding angle was obtained when stretching was applied to the G-TiO$_2$/PDMS samples in the normal direction to the external tensile strain. In conclusion, reversible wetting of G-TiO$_2$/PDMS surface can be managed by manual manipulation.
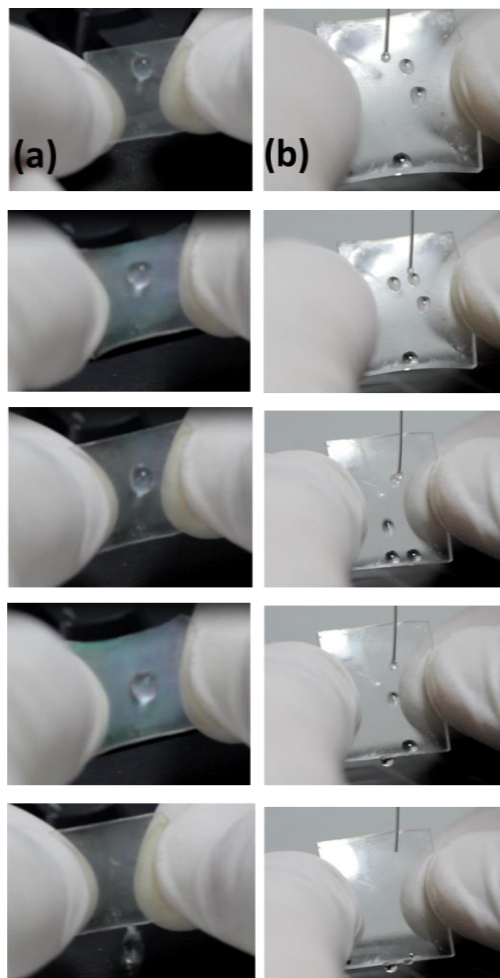
Figure 6.7. *a) Water control by stretching a G-85°-TiO$_2$/PDMS foil. The volume of water is 20ul. b) Diiodomethane control by streching on growing-G-60°-TiO$_2$ /PDMSsurface. The volume of the diiodomethane droplets are 5ul.*

6.4 Conclusions

Oriented nanostructured GLAD TiO$_2$ coatings on PDMS foil under manual manipulation demonstrated a selective liquid drops transport without possessing a superhydrophobic surface state due to the induced dual-scale roughness of the nanocolumns distribution together with the parallel groove formation and associated wrinkled self-pattern of the flexible substrate. Water drops pinning/release alternation is possible from concave to convex bending of the G-TiO$_2$/PDMS samples. Meanwhile, the stretched G-TiO$_2$/PDMS system exhibits an omniphobic behavior making possible the delay of the non-polar liquid motion on the surface by mechanical actuation. Besides, two anisotropic wetting levels are observed: 1) wettability in the bundling direction of the G-TiO$_2$ structure is lower than in the growing one and 2) sliding on the parallel direction of the external applied strain is better than on the normal one, especially for non-polar liquids. In conclusion, the oriented nanostructured micropatterned G-TiO$_2$/PDMS samples are presented as promising materials for selective microfluidic devices and water/oil separation filters when are subjected to an easy manual manipulation.

REFERENCES

(1)   Rahmawan, Y.; Xu, L.; Yang, S. *J. Mater. Chem. A* **2013**, *1* (9).

(2)   Malvadkar, N. A.; Hancock, M. J.; Sekeroglu, K.; Dressick, W. J.; Demirel, M. C. *Nat. Mater.* **2010**, *9* (12), 1023–1028.

(3)   Lai, Y.-K.; Tang, Y.-X.; Huang, J.-Y.; Pan, F.; Chen, Z.; Zhang, K.-Q.; Fuchs, H.; Chi, L.-F. *Sci. Rep.* **2013**, *3*.

(4)   Ionov, L. *J. Mater. Chem.* **2012**, *22* (37).

(5)   Lee, S. G.; Lim, H. S.; Lee, D. Y.; Kwak, D.; Cho, K. *Adv. Funct. Mater.* **2013**, *23* (5), 547–553.

(6)   Kang, S. M.; Lee, C.; Kim, H. N.; Lee, B. J.; Lee, J. E.; Kwak, M. K.; Suh, K.-Y. *Adv. Mater.* **2013**, *25* (40), 5756–5761.

(7)   Wu, D.; Wang, J.-N.; Wu, S.-Z.; Chen, Q.-D.; Zhao, S.; Zhang, H.; Sun, H.-B.; Jiang, L. *Adv. Funct. Mater.* **2011**, *21* (15), 2927–2932.

(8)   Zhang, F.; Low, H. Y. *Langmuir* **2007**, *23* (14), 7793–7798.

(9)   Öner, D.; McCarthy, T. J. *Langmuir* **2000**, *16* (20), 7777–7782.

(10)   Watson, G. S.; Cribb, B. W.; Watson, J. A. *ACS Nano* **2010**, *4* (1), 129–136.

(11)   Yoshimitsu, Z.; Nakajima, A.; Watanabe, T.; Hashimoto, K. *Langmuir* **2002**, *18* (15), 5818–5822.

(12)   Chung, J. Y.; Youngblood, J. P.; Stafford, C. M. *Soft Matter* **2007**, *3* (9).

(13)   Nagai, H.; Irie, T.; Takahashi, J.; Wakida, S. *Biosens. Bioelectron.* **2007**, *22* (9–10), 1968–1973.

(14)   Wenzel, R. N. *Ind. Eng. Chem.* **1936**, *28* (8), 988–994.

(15)   Cassie, A. B. D.; Baxter, S. *Trans. Faraday Soc.* **1944**, *40* (0), 546–551.

(16)   Lin, P.-C.; Yang, S. *Soft Matter* **2009**, *5* (5).

(17)   Hunt, J. A.; Williams, R. L.; Tavakoli, S. M.; Riches, S. T. *J. Mater. Sci. Mater. Med.* **1995**, *6* (12), 813–817.

(18)   Houston, K. S.; Weinkauf, D. H.; Stewart, F. F. *J. Membr. Sci.* **2002**, *205* (1–2), 103–112.

(19)   Parra-Barranco, J.; Oliva-Ramirez, M.; Gonzalez-Garcia, L.; Alcaire, M.; Macias-Montero, M.; Borras, A.; Frutos, F.; Gonzalez-Elipe, A. R.; Barranco, A. *ACS Appl. Mater. Interfaces* **2014**, *6* (15), 11924–11931.

(20)   Kapridaki, C.; Maravelaki-Kalaitzaki, P. *Prog. Org. Coat.* **2013**, *76* (2-3), 400–410.

(21)   Tavares, M. T. S.; Santos, A. S. F.; Santos, I. M. G.; Silva, M. R. S.; Bomio, M. R. D.; Longo, E.; Paskocimas, C. A.; Motta, F. V. *Surf. Coat. Technol.* **2014**, *239*, 16–19.

(22)   Guldin, S.; Kohn, P.; Stefik, M.; Song, J.; Divitini, G.; Ecarla, F.; Ducati, C.; Wiesner, U.; Steiner, U. *Nano Lett.* **2013**, *13* (11), 5329–5335.

(23)   Wang, J.-H.; Shih, T.-K.; Chen, C.-F.; Chen, K.-C.; Chen, C.-C.; Whang, W.-T.; Huang, G. S.; Su, H.-Y. *Opt. Commun.* **2008**, *281* (15-16), 3953–3956.

(24)   Noh, J.-S. *Nanoscale Res. Lett.* **2013**, *8* (1).

(25)   Deng, Z.-Y.; Wang, W.; Mao, L.-H.; Wang, C.-F.; Chen, S. *J. Mater. Chem. A* **2014**, *2* (12).

(26)   Nakata, K.; Udagawa, K.; Ochiai, T.; Sakai, H.; Murakami, T.; Abe, M.;
Fujishima, A. *Mater. Chem. Phys.* **2011**, *126* (3), 484–487.

(27)   Zhou, S.; Ding, X.; Wu, L. *Prog. Org. Coat.* **2013**, *76* (4), 563–570.

(28)   Lee, E.; Zhang, M.; Cho, Y.; Cui, Y.; Van der Spiegel, J.; Engheta, N.;
Yang, S. *Adv. Mater.* **2014**, *26* (24), 4127–4133.

(29)   Kim, K.-D.; Seo, H. O.; Sim, C. W.; Jeong, M.-G.; Kim, Y. D.; Lim, D. C.
Prog. Org. Coat. **2013**, *76* (4), 596–600.

(30)   González-García, L.; Parra-Barranco, J.; Sánchez-Valencia, J. R.; Barranco,
A.; Borrás, A.; González-Elipe, A. R.; García-Gutiérrez, M.-C.; Hernández,
J. J.; Rueda, D. R.; Ezquerra, T. A. *Nanotechnology* **2012**, *23* (20).

(31)   Gonzalez-García, L.; Parra-Barranco, J.; Sanchez-Valencia, J. R.; Ferrer, J.;
Garcia-Gutierrez, M.-C.; Barranco, A.; Gonzalez-Elipe, A. R. *Adv. Funct.
Mater.* **2013**, *23* (13), 1655–1663.

(32)   Hawkeye, M. M.; Taschuk, M. T.; Brett, M. J. *Glancing angle deposition of
thin films: engineering the nanoscale*; 2014.

(33)   Hawkeye, M. M.; Brett, M. J. *J. Vac. Sci. Technol. Vac. Surf. Films* **2007**, *25*
(5).

(34)   Sanchez-Valencia, J. R.; Toudert, J.; Borras, A.; Barranco, A.; Lahoz, R.; de
la Fuente, G. F.; Frutos, F.; Gonzalez-Elipe, A. R. *Adv. Mater.* **2011**, *23* (7),
848–853.

(35)   Sánchez-Valencia, J. R.; Toudert, J.; Borras, A.; López-Santos, C.; Barranco,
A.; Feliu, I. O.; González-Elipe, A. R. *Plasmonics* **2010**, *5* (3), 241–250.

(36)   Sánchez-Valencia, J. R.; Toudert, J.; Borras, A.; López-Santos, C.; Barranco,
A.; Feliu, I. O.; González-Elipe, A. R. *Plasmonics* **2010**, *5* (3), 241–250.

(37)   Rios, P. F.; Dodiuk, H.; Kenig, S.; McCarthy, S.; Dotan, A. *J. Adhes. Sci.
Technol.* **2007**, *21* (3-4), 227–241.

(38)   Efimenko, K.; Crowe, J. A.; Manias, E.; Schwark, D. W.; Fischer, D. A.;
Genzer, J. *Polymer* **2005**, *46* (22), 9329–9341.

(39)   Owens, D. K.; Wendt, R. C. *J. Appl. Polym. Sci.* **1969**, *13* (8), 1741–1747.

(40)   Roucoules, V.; Ponche, A.; Geissler, A.; Siffer, F.; Vidal, L.; Ollivier, S.;
Vallat, M. F.; Marie, P.; Voegel, J. C.; Schaaf, P.; Hemmerlé, J. *Langmuir*
2007, *23* (26), 13136–13145.

Chapter 7

General conclusions

The main achievements and conclusions of the work developed throughout the present thesis are summarized in this chapter.

- The present work showed that structural anisotropy of GLAD thin films is powerful tool to develop applications in different field of study.

- Plasma assisted system has been developed and implemented to growth oxides by glancing angle conditions.

- GLAD thin films on flexible polymers has been developed in this work satisfactory. Due to the extreme simplicity of the GLAD procedure on flexible polymers, it can be a starting point for new design strategies of photonic elements, opto-mechanical actuators, security labeling (G-SiO$_2$/PDMS) or reversible microfluidics valves, controlled wetting and microfluidics filters for (G-TiO$_2$/PDMS.)

- In this work has been developed two different ways to control, enhance and manipulate anisotropic properties in GLAD thin films. The first one consists of the control of the microstructure at the nano-scale and relays on assisting the growth of the film with a plasma during deposition. The second one appears at the micro-scale and is produced by a combination of factors involving the mechanical deformation on flexible polymers.

- Plasma assisted during GLAD growth has been utilized to fabricate porous ITO thin films with high optical transparency and electrical conductivity.

- The results prove that the thin film microstructure of the films can be effectively control by plasma-GLAD. This procedure also induces a considerable enhancement on the surface anisotropy of the ITO GLAD thin films, while the tilting angle orientation of their constituent nanocolumns becomes also modified.

- ITO GLAD and plasma-GLAD films present different in-depth and sheet conductivities as expected from their different porous and nanocolumnar microstructures.

- ITO plasma-GLAD thin films depict a high anisotropy in its in-plane conductivity behavior that has been linked with the association of nanocolumns (denoted as bundling) in a preferential direction perpendicular to the incoming flux of materials during deposition.

- Gold nanoparticles grown in these thin films by electrodeposition present a dichroic behavior when examined with polarized light. Plasma-GLAD thin films present a high birefringence ($\Delta n=0,2$) with different refractive indexes values along the bundling direction (1.48) and the perpendicular to it (1.68)). This is the highest birefringence reported up to now for metal oxide thin films prepared by GLAD.

- Plasma-GLAD thin films present a complex dichroic response when turning the samples around both their polar and azimuthal axis, especially when the rotation modifies the inclination of the columns (y-AXIS).

- A method has been developed that combines the use of cross polarizers, masks or photolithography and the highly birefringent films for the construction of highly dichroic patterns for advanced labelling and/or marking applications.

- Anisotropic flexible devices have been fabricated by growing GLAD thin films on flexible substrates. PDMS foils covered with nanocolumnar SiO_2 and TiO_2 thin films prepared by GLAD develop a reversible/switchable grating structure when bended. The grating behavior was independent on the curvature degree but was directly linked with the type of thin film deposited on its surface.

- In the SiO_2 and TiO_2/PDMS devices the reversible grating formation could be associated with a regular micrometric parallel crack structure that appears upon bending . For SiO_2 /PDMS a distinct diffractive behavior was found depending on whether the system is bended along the bundling and perpendicular directions of the film.

- Invisible labels have been developed using these SiO_2 /PDMS foils where the information can only be retrieve by reversible bending.

- TiO$_2$/PDMS foil under manual manipulation demonstrated a selective liquid drops transport without possessing a superhydrophobic surface in the original non-bended state. This is due to the induced dual-scale roughness induced at the surface upon bending and due to the nanocolumns distribution and the wrinkled self-pattern of the flexible substrate.

- Water drops retention/release alternation is possible by concave to convex bending the TiO$_2$/PDMS samples in two perpendicular directions (bundling and perpendicular).

- Upon stretching of the TiO$_2$/PDMS system it exhibits an omniphobic behavior producing a delay in the movement of non-polar liquid on the surface.

.